Clathrate hydrate formation in different chemical environments relevant to subsurface CO_2 storage

Master thesis in Petroleum Chemistry
by
Malene Lid Johannesen

Department of Chemistry

University of Bergen

August 2018

Abstract

Storing of carbon dioxide (CO_2) as hydrates in the formation of the subsurface permafrost and oceanic areas around the world is a new method of carbon capture and storage (CCS). Clathrate hydrates are solids consisting of water molecules bonded together in a crystalline structure encapsulating a guest gas molecule (e.g. CO_2). Storage of CO_2 as hydrate in the subsurface could contribute to limiting the current release of greenhouse gases released into the atmosphere. Furthermore, conventional CCS methods with deposition of CO_2 in depleted hydrocarbon reserves and water reservoirs have proposed to use CO_2 hydrate as a sealing barrier to limit the migration of liquid CO_2 upwards into the formation.

This thesis presents a study of the various parameters affecting CO_2 hydrate formation in a Bentheimer sandstone core, under realistic in-depth conditions. A range of experiments performed in different chemical environments with THF as an analogue to CO_2 was set up to design the parameters for the CO_2 hydrate formation experiments in the sandstone cores. Furthermore, the use of Magnetic Resonance Imaging (MRI) have been used for analysis of the macroscopic crystal structure and morphology of THF hydrates with particles of various wetting properties.

The formation of CO_2 hydrates in Bentheimer sandstone cores was seen to form a solid barrier that prevented further injection when the system was inside the Hydrate Stability Zone (HSZ). These results display the possibility of using CO_2 hydrate as a sealing barrier for further migration of liquid stored in conventional water reservoirs. Furthermore, increase in temperature, pressure (only for CO_2) and electrolyte concentration was seen to prolong or even prevent the formation of CO_2- and THF hydrates.

Natural occurring substances, such as Utsira formation water, and particles from Bentheimer sandstone were seen to promote hydrate growth. Use of MRI to study the macroscopic crystal structure and morphology of THF hydrate displayed liquid phase inside what appeared to the visible eye as solid hydrate. The morphology of ice versus THF hydrate in bulk displayed a significantly different structure formed. The natural substances Illite and Bentheimer solid particles were seen to promote formation of liquid channels inside the formed hydrate structure that upon melting obtained more liquid.

Acknowledgements

First of all I would like to thank my main supervisor Professor Tanja Barth of the Department of Chemistry at the University of Bergen for giving me the opportunity to write such an interesting thesis on gas hydrates. This thesis would not be the same without your guidance and knowledge within the field. You always took the time to answer questions and your encouragements, have been greatly appreciated. Thank you.

I would also like to thank my other supervisor post doc Jarand Gauteplass of the Department of Chemistry at the University of Bergen for introducing me to reservoir physics and for providing valuable input to this thesis. Your constructive comments and discussions have been very appreciated. Furthermore, I would like to express my gratitude to both Jarand and PhD candidate Stian Almenningen of the Department of Physics and Technology at the University of Bergen for welcoming me into your research project and spending many hours teaching me about fluid flow in porous media at the laboratory.

Furthermore, I would also like to express my gratitude toward my other supervisor Professor Per Fotland et Equinor for helping me with the experimental set-up with the MRI instrument at Equinor's facilities. Your help with feedback on my thesis and helping me enhance my understanding of gas hydrates and the MRI instrument is very appreciated. Moreover, I want to thank Gry Lien Aastveit from Equinor for additional with the MRI instrument.

Last but not least, nothing really matters without friends and family. So, thanks to everyone who makes my life so enjoyable :-)

Thank you.

Bergen, August 2018

Malene Lid Johannesen

Contents

Abbreviations and symbols

Abbreviations

Atm	Atmosphere (s)
CCS	Carbon capture and storage
CH_4	Methane
CNG	Compressed natural gas
CO_2	Carbon dioxide
CP	Cyclopentane
G	Guest molecule
GtC	Gigaton Carbon (1 GtC= 1* 10^{12} g Carbon)
H_2O	Water
HBGS	Hydrate based gas separation
HEN	Heterogenous nucleation
HON	Homogenous nucleation
HSZ	Hydrate stability zone
IR	Infrared
LDHI	Low dosage hydrate inhibitor
LNG	Liquified natural gas
MeOH	Methanol
MRI	Magnetic resonance imaging
NHI	Natural hydrate inhibitors
NMR	Nuclear magnetic resonance
PT	Pressure and Temperature
RF	Radio frequency
ROV	Remote Operated Vehicle
SNG	Solidified natural gas
STP	Standard temperature and pressure
THF	Tetrahydrofuran

Symbols

ΔG	Gibbs free energy
ΔG_s	Energy of the solute molecule required to become part of the surface of the crystal nuclei
ΔG_v	Energy of solute molecule required to become part of the bulk/ interior of the crystal nuclei
ΔP	Differential pressure across the core (atm)
°C	Celsius
μ	Viscosity (cP= 1 kg/ms)
A	Cross section of ore (cm^3)
B_0	Static magnetic field
D	Darcy
G	Guest molecule
k	Permeability (D)
L	Length of core (cm)
mass %	Mass percentage
n	Hydration number
P	Pressure (bar)
ϕ	Porosity (%)
q	Flow rate (cm^3/s)
r	Radius
r	Radius
r_c	Critical radius size of nucleus
r_c	Critical radius size of nucleus
S_{bt}	Saturation at gas breakthrough (frac)
sH	Structure H hydrate
sI	Structure I hydrate
sII	Structure II hydrate
S_{iw}	Irreducible water saturation (frac)
S_w	Saturation (frac)
T	Temperature
T	Tesla, strength of magnetic field
T1	Spin-spin relaxation
T2	Spin-lattice relaxation
V_b	Bulk volume
V_p	Pore volume
θ	Contact angle (^{0})
π	Pi (3,14159)
ρ	Density (g/cm3)
σ	Surface tension

1 Introduction

1.1 Motivation

The Paris agreement by 125 parties in 2017 aim to “decelerate and fight the current climate changes by intensifying the actions and investments needed for a sustainable carbon-constrained future. By strengthening the global response to climate change the goal of United Nations is to keep the global temperature rise lower than 2ºC above the pre-industrial levels by the end of this century” (United Nations, 2015).

Finding methods of reducing release of anthropogenic CO_2 into the atmosphere is crucial to meet the future climate demands. One approach could be to store CO_2 in the geological formation as gas hydrates. Clathrate hydrates are inclusion compounds consisting of a lattice of water molecules encapsulating a guest gas molecule. The first discovery of clathrate hydrates was by Sir Humphrey Davy in 1810, where he discovered chlorine hydrate (Davy, 1811). The identification of natural gas stored as hydrates as an energy resource by Makogon in 1965 led to a new research field focusing on how to economically and technically retrieve natural gas from hydrate deposits in the permafrost and oceanic regions around the world (Makogon et al., 2007, Makogon, 2010).

Natural gas hydrates are found in abundance in the subsurface of the permafrost regions and in the deep oceanic seabed areas around the world and comprise a vast energy resource if it can be recovered safely and economically. The accumulation of natural gas hydrates is primarily governed by the physical conditions, i.e. pressure and temperatures, and thus hydrate reserves are found in areas that have relatively high pressures and low temperatures in combination with the presence of water and guest gas molecules to form hydrates. These regions are commonly referred to as hydrate stability zones (HSZ).

Expected development in the primary energy demand today is shown in Figure 1 and displays the vast energy need in India and China especially. The potential reserves of hydrates are more evenly distributed around the earth than current fossil fuels and therefore makes a promising energy resource for the entire world (Makogon et al., 2007). Asia in particular has large numbers of hydrate deposits and utilizing natural gas stored as hydrates as an unconventional energy resource could be one of the solutions of solving the energy need in these countries and simultaneously reducing CO_2 emissions (Boswell and Collett, 2011).

Figure 1. Projected change in primary energy demand (Mtoe), 2016-2040 from Birol (2017). Yellow indicates increase in primary energy demand and red indicates reduction in primary energy demand.

Early estimates of the potential reserves of gas hydrates have been estimated to exceed all coal, natural gas and hydrocarbon reserves combined, with an upper estimate of 10 000 GtC (Sloan and Koh, 2008, Kvenvolden, 1995). Recent studies however have shown a large deviation in the estimates of global carbon trapped as hydrates, seen from figure 2 where a) shows the early estimates of 11 000 GtC made by Kvenvolden (1988) and b) the more recent estimates of 1800 GtC made by Milkov (2004), Boswell and Collett (2011) and Piñero et al. (2013). Even the lowest estimates display a vast amount of natural gas stored as hydrates.

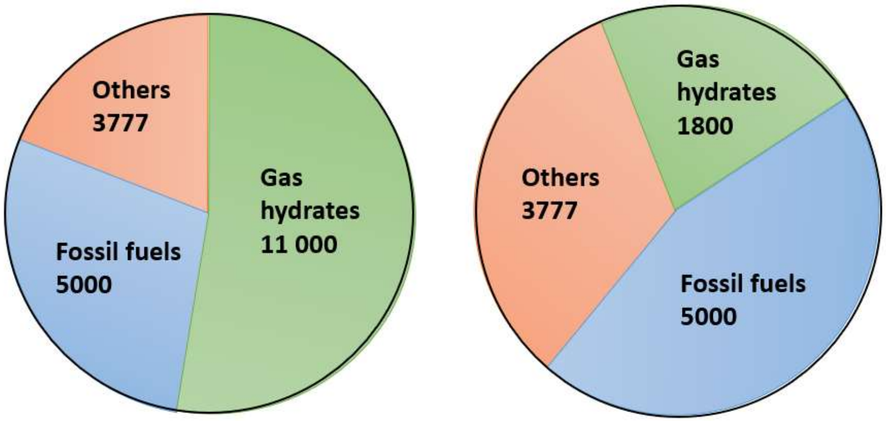

Figure 2. The estimated global carbon trapped as gas hydrates. Figure a) shows the estimated amounts of avaiable carbon trapped as gas hydrates from Kvenvolden (1988) and b) the newer estimates made by Milkov (2004), Boswell and Collett (2011) and Piñero et al. (2013) showing a substantial lower estimate. The numers are given as gigatonne Carbon, GtC (1 GtC= 10^{12} g Carbon). Figure reproduced from Ruppel and Kessler (2017).

Gas hydrate formation is usually considered a challenge in the petroleum industry, particularly in multiphase flow systems, where hydrates can plug pipelines during both transport and production from reservoir. However, the formation of hydrates can be used as a benefit within the Carbon Capture and Storage (CCS) field. Current methods of CO_2 storage involve storage of CO_2 in supercritical phase in depleted hydrocarbon reserves or water reservoirs, with temperatures outside the hydrate stability zone (HSZ). A promising alternative to current CCS methods is storage of CO_2 as hydrates in geological formations within the HSZ. One proposed method is the possibility of injecting CO_2 to thermodynamically replace methane gas stored as hydrate with CO_2 hydrates. This method would provide an energy resource from methane gas in addition to limit the release of greenhouse gases released into the atmosphere (Ersland et al., 2009).

In addition to the possibility of replacing methane hydrate by CO_2 hydrate in formation, there are methods under developments which focuses on the capture of CO_2 for further storage, often referred to as Hydrate based gas separation (HBGS). This method involves separation of different gases by their ability to form hydrates at different conditions (i.e. pressures and temperatures). The addition of promoters (liquids/solids) that accelerate hydrate growth is an important factor for making this technology possible, in addition to the dependency of continuous and rapid hydrate growth (Englezos et al., 2015, Linga et al., 2013).

Conventional CCS methods have by Koide et al. (1995) proposed to use CO_2 hydrates as a sealing barrier for limit migration of liquid CO_2 (i.e. CO_2 becomes supercritical at approximately 800m depth due to hydrostatic temperatures and pressures) upwards in the formation (Koide et al., 1995). As described by Rochelle et al. (2009) and Gauteplass et al. (2018), the Gas Hydrate Stability Zone (GHSZ) is estimated to a thickness of 0,5 km on the western European shelves, providing a large potential of CO_2 hydrate as a sealing mechanism for liquid CO_2 storage (Gauteplass et al., 2018, Rochelle et al., 2009). Further research on CO_2 hydrate formation under realistic conditions are necessary for evaluation of CO_2 hydrates as a sealing barrier.

Furthermore, Solidified Natural Gas (SNG), i.e. converting natural gas to hydrates, is proposes as a new method of transportation and storage of natural gas above surface. This method has a greater storage capacity than conventional methods such as Compressed Natural Gas (CNG) and Liquified Natural Gas (LNG, i.e. cooling gas to condensate) in addition to being a safer option (Veluswamy et al., 2018, Pandey et al., 2017).

1.2 Objectives

Three different experimental methods are used for investigation of how chemical and physical factors influence hydrate nucleation and growth of CO_2-and THF hydrate. The main objective is investigation of CO_2 as a sealing barrier for conventional CO_2 storage in addition to storage of CO_2 as hydrates in formation. Since THF forms hydrates at ambient pressure this hydrate former is used as analogue to CO_2. Results from the THF experiments are used for optimization of the high-pressure experiments with CO_2 in porous media. The specific objectives for this thesis were:

1. Perform experiments at atmospheric conditions with THF as hydrate former to investigate various parameters affecting hydrate growth. The various parameters were:
    a. Change in temperature
    b. Change in electrolyte concentration
    c. Change in mole ratio of solution
    d. Addition of solids with varying wetting properties
2. Exploration of the macroscopic crystal structure and morphology of THF hydrate by use of Magnetic Resonance Imaging (MRI) instrument. Experiments with THF hydrate in bulk solution and with the addition of particle of varying wetting properties is performed in addition to the study of the macroscopic crystal structure of ice versus THF hydrate.
3. Perform experiments with CO_2 as hydrate former in Bentheimer sandstone cores under realistic conditions. The CO_2 injection rate, temperature and synthetic brine solutions is changed to analyze the effect on hydrate growth in porous media.

2 Theory

2.1 Clathrate hydrates

Clathrate hydrates are crystalline solids composed of water molecules capable of encapsulating different light hydrocarbon guest gas- and liquid molecules within the cavities that are formed. The most common gas hydrates formers are methane, ethane, propane and carbon dioxide. Natural gas hydrates form at relatively low temperatures and high pressures. One of the distinctive features of hydrates is the capability of storing a large amount of gas in a small volume (164 volumes of gas in one volume of methane hydrate at STP) (Makogon et al., 2007). The following sub-sections go into more detail on the crystalline structure, guest molecule, occurrence and the various parameters effecting the growth and dissociation of hydrates.

2.1.1 The crystalline structure of hydrates

The hydrate crystal structure is held together by hydrogen bonding between the water molecules which is stabilized by encapsulation of guest molecules. The attraction forces between the guest molecule and the water molecule is Van der Waals forces (Makogon, 2010). The stability of the lattice is dependent on which guest is encapsulates and the size and geometry of the guest. The main difference between ice and hydrates is that ice is able to form a stable lattice without a guest molecule whereas a hydrate lattice will not form without this guest molecule present.

Different crystalline structures can arise dependent on which guest molecule it encapsulates, and there are three main types (figure 3 and table 1): Structure I is composed of two small 5^{12} (pentagonal dodecahedron) cavities and six large $5^{12}6^{2}$ (tetrakaidecahedron) cavities. Structure II composed of sixteen small 5^{12} cavities and eight large $5^{12}6^{4}$ (hexakaidecahedron) cavities. Structure H consist of three small 5^{12} cavities, two medium $4^{3}5^{6}6^{3}$ (irregular dodecahedron) and one large $5^{12}6^{8}$ (icosahedron) cavities. Normally only one guest is present inside one cavity and the size of the guest is close to the size of the cage itself. The relationship between the guest size and cavity size is important for stabilization of the hydrate strucutre, guest molecules too small will not be able to stabilize a large cavity.

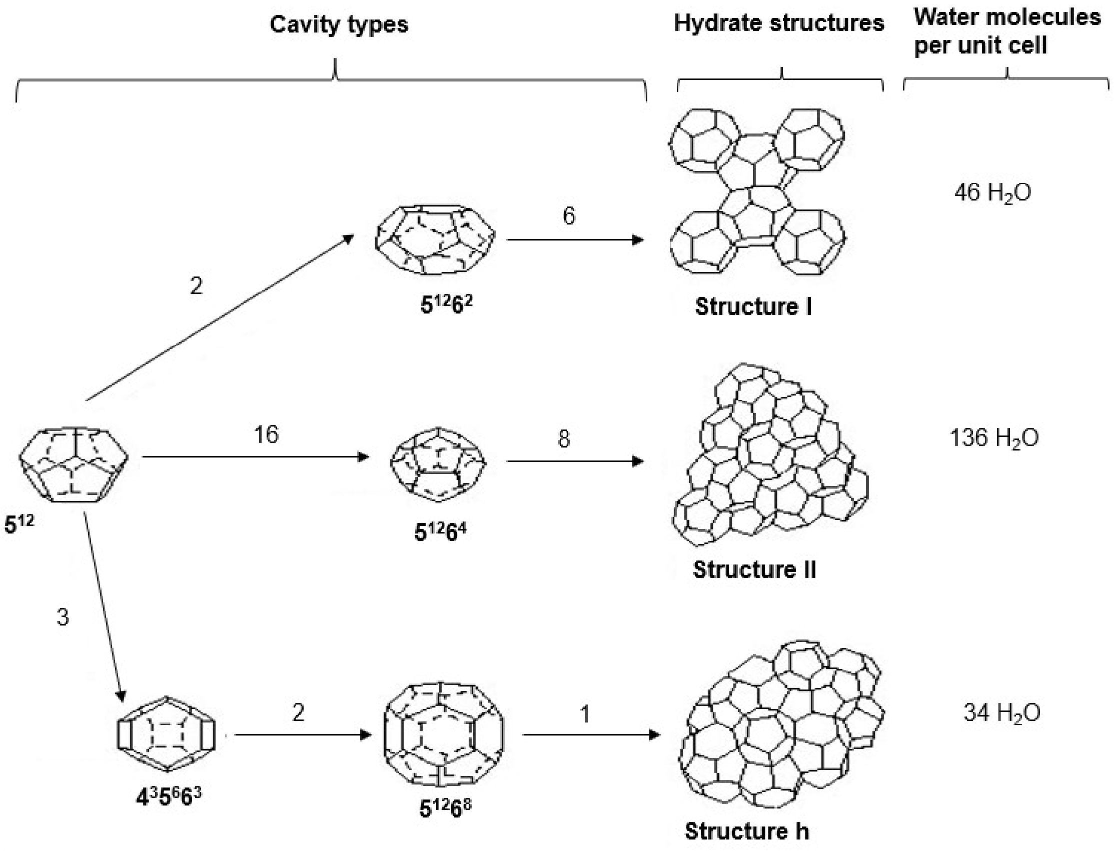

Figure 3. The tree main hydrate structures: sI, sII and sH. The numbers above the arrows indicates how many cavities per unit cell. The 5^{12} consist of 12 pentagons connected to one cavity, the $5^{12}6^2$ cavity consist of 12 pentagons and two hexagons, the $4^35^66^3$ cavity consist of three squares, six pentagons and three hexagons and so forth. Figure reproduced modified from Sloan (2003) and Anderson (2017).

Table 1. Properties of the three hydrate crystal structures. Reproduced from Sloan and Koh (2008).

Hydrate crystal structure	I		II		H		
Cavity	Small	Large	Small	Large	Small	Medium	Large
Description	5^{12}	$5^{12}6^2$	5^{12}	$5^{12}6^4$	5^{12}	$4^35^66^3$	$5^{12}6^8$
Number of cavities per unit cell	2	6	16	8	3	2	1
Average cavity radius (Å)	3,95	4,33	3,91	4,73	3,91	4,06	5,71
Number of waters molecules per unit cell	46		136			34	

2.1.2 The guest molecule

The most common guest molecules that form hydrates in nature are small gas molecules like methane, ethane, propane or carbon dioxide (Sloan and Koh, 2008). Methane hydrate is the most abundant hydrate former on earth and forms structure II hydrates, whereas carbon dioxide forms structure I.

Liquid hydrate formers are molecules such as tetrahydrofuran (THF) and cyclopentane (CP), figure 4, which form structure II and I, respectively. Both THF and CP are commonly used in the laboratory due to their ability to form hydrates at ambient pressures and is sometimes used as analogues to CH_4 and CO_2, which only forms hydrates at elevated pressures. THF is used as an analogue to CO_2 since both are water soluble and CP as analogue to CH_4 since they are not water soluble. THF is used as analogue for CO_2 in this thesis to perform numerous experiments without the need for pressurized equipment.

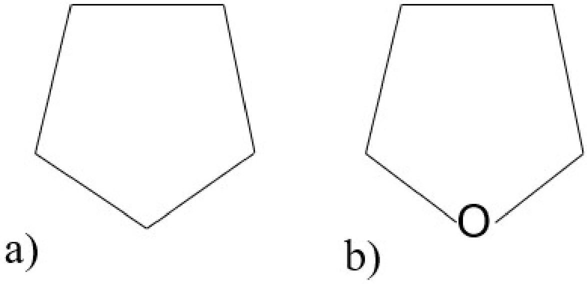

Figure 4. Molecular structure of a) Cyclopentane (CP) and b) Tetrahydrofuran (THF). Figure made by the author.

The number of water molecules required for forming hydrates with a specific guest molecule is referred to the ideal hydration number. The ideal hydration number, G x nH_2O, where n= hydration number, depends on which hydrate structure the guest molecules (G) forms and if it occupies the large, small or intermediate cavity. For THF the ideal hydration number is 17 H_2O: 1 THF where the THF molecules occupy the large cavities of structure II. The ideal hydration number will in principle yield complete conversion of water and THF to solid hydrate. The ideal hydration number for CO_2 is 5 ¾H_2O: 1 CO_2 where CO_2 occupies both the large and the small cavities of structure I (Sloan and Koh, 2008).

The theoretical ideal hydration number of 17 H_2O: 1 THF corresponds to approximately 20 wt.% THF solution. Figure 5 shows the melting point temperature for THF hydrate in water solution at different weight percentages of THF with the maximum melting point temperature of 4,5°C at approximately 20 wt.% THF. By use of PVTsim the pressure-temperature phase diagram for a 20 wt.% THF solution with 3,5 wt.% NaCl has been produced, figure 6. Here it can be seen that a 20 wt.% THF solution with 3,5 wt.% NaCl is within the hydrate forming region below 4°C. Experiments performed in this thesis with

THF as hydrate former used 2ºC or lower temperatures at atmospheric conditions, well within the stability zone.

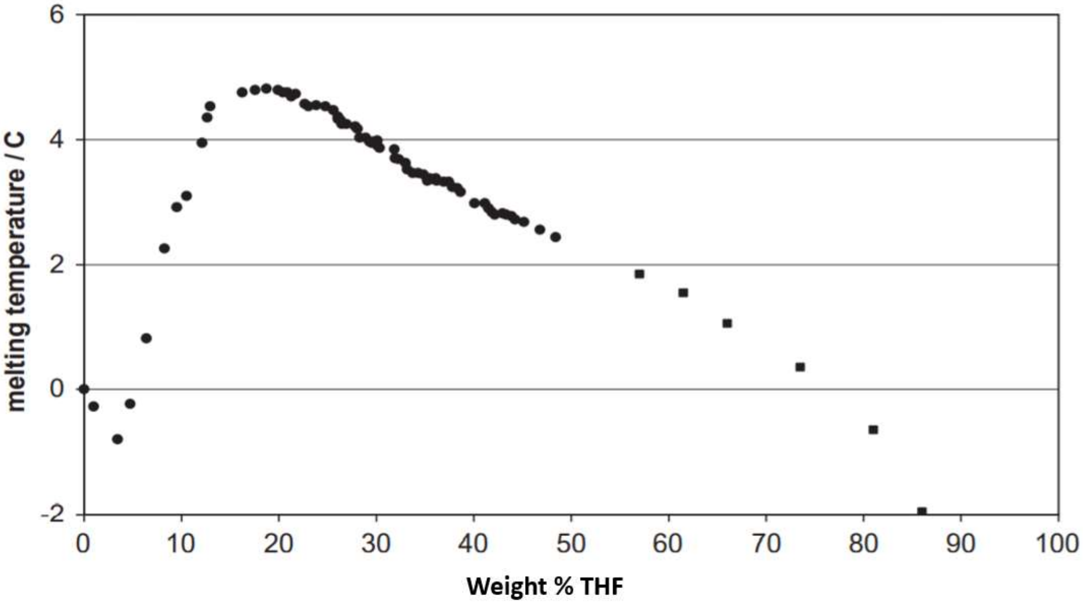

Figure 5. Shows the melting point curve of THF hydrate with ultrapure water at different wt.%, figure reproduced from Wilson et al. (2005).

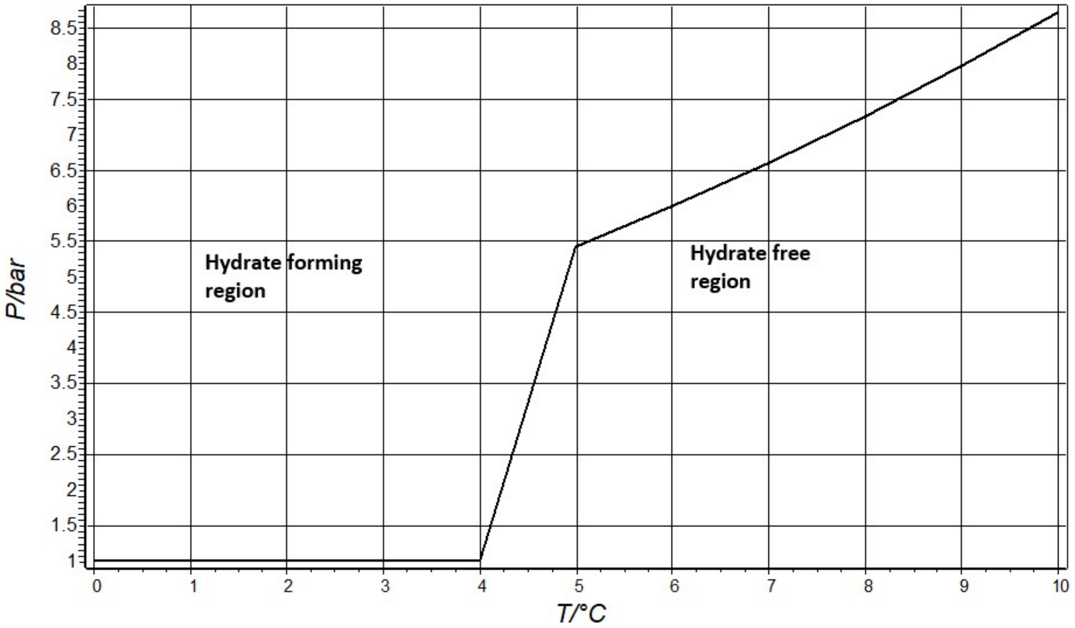

Figure 6. Pressure-Temperature phase diagram of a 20 wt.% THF solution with 3,5 wt.% NaCl. The equilibrium line can be seen to increase rapidly from 4ºC. The hydrate forming region is on the left of the line and hydrate free region on the right. Figure produced in PVTsim by Jarand Gauteplass and modified by author.

2.1.3 Phase equilibrium of gas hydrates

The different pressures and temperatures where the guest molecules can form hydrates at are usually presented in a phase diagram (PT- diagram). The calculated phase diagram for CO_2 hydrate at different electrolyte concentrations chosen for this thesis have been simulated by use of the simulation software PVTsim, Nova Calsep, shown in figure 7. Each of the equilibrium lines shown in figure 7 represent CO_2 in solution with various electrolyte concentrations, where the hydrate stability zone (HSZ) is on the left side of the equilibrium line and no hydrate formation will occur on the right side. The inhibition effect of electrolyte concentration can be seen here, where increase in electrolyte concentration moves the equilibrium further on the left side, reducing the HSZ considerably. These phase diagrams are frequently used in the oil industry where complex constituents in a reservoir including gases, liquid hydrocarbons and water is present at various temperatures and pressures. For oil production purposes it is ideal to stay outside the hydrate stability zone and avoid any hydrates from forming and possibly blocking pipelines. In modern oil production processes the oil and gas from reservoirs are produced from within the HSZ by a method referred to as hydrate management (Kinnari et al., 2015), where the operators can produce from within the HSZ by continuous monitoring and evaluations of hydrate plugging tendencies.

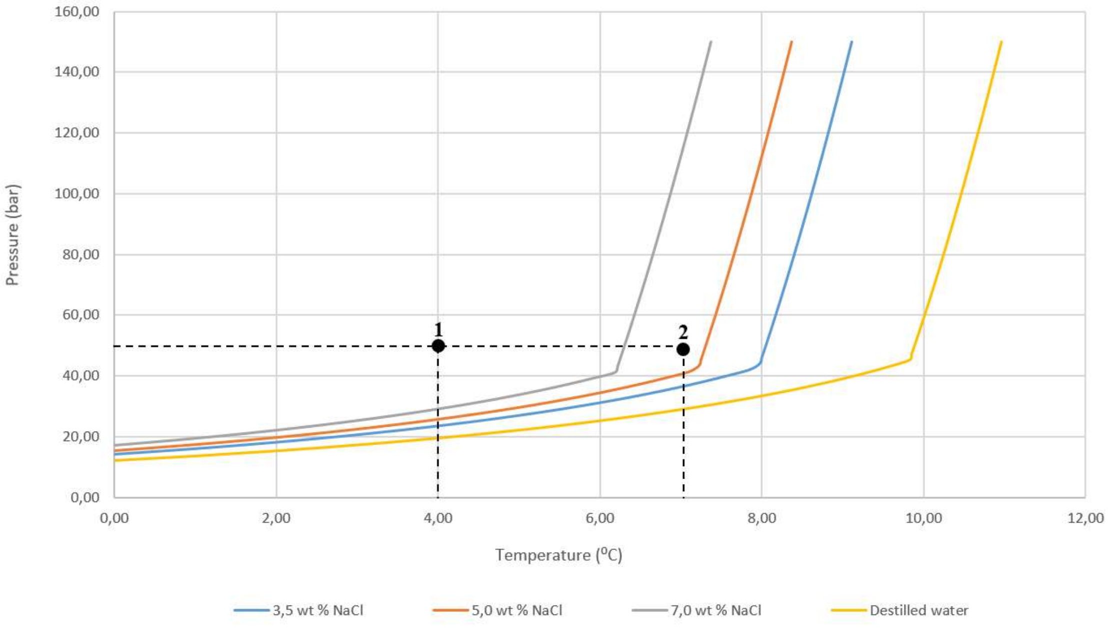

Figure 7. Pressure-and temperature (PT) diagram for carbon dioxide hydrate at different sodium chloride (NaCl) concentrations. The left side of each curve shows the area within the hydrate stability zone. Point 1 and 2 represent the system parameters used for this thesis for the CO_2 hydrate formation experiments. Figure made in PVTsim.

This thesis has used CO_2 as hydrate former under experimental conditions of 70 bar with temperatures of 4ºC or 7ºC, indicated as point 1 and 2 in figure 7, respectively. Figure 7 shows that hydrates can form at point 1 for all electrolyte concentrations but at point 2 only 5,0 and 3,5 wt.% NaCl is within HSZ (left of curve). The further the system is inside the HSZ, the higher driving forces are present, and consequently higher probability of hydrate formation.

2.1.4 Hydrate nucleation

Hydrate nucleation can be divided into homogenous (HON) or heterogenous (HEN) nucleation where the difference is that HON involves the absence of particles or solid phases and HEN involves nucleation on a substrate (particles and solid surfaces). In the majority of systems, the nucleation will be heterogenous due to the presence of particles or solid surfaces.

Nucleation is the process where small clusters of water and gas/liquid molecules grow to achieve critical size (r_c) for spontaneous growth. For homogenous nucleation the energy required for spontaneous growth can be described by the Gibbs free energy (ΔG), figure 8. From this figure and equation 1 below it can be seen that the sum of ΔG_s and ΔG_v equals the total ΔG, where ΔG_s represents the energy required of the solute molecule (e.g. THF) to become part of the surface of the crystal nuclei and ΔG_v represents the energy required of the solute molecule to become part of the bulk/interior of the crystal nuclei (Sloan and Koh, 2008, Larson and Garside, 1986). Equation 1 below shows the Gibbs free energy required for homogenous nucleation and assumes spherical clusters with radius r:

$$\Delta G = \Delta G_s + G_v = 4\pi r^2 \sigma + \frac{4}{3}\pi r^2 \Delta g_v \qquad \text{Equation 1}$$

, where σ is the surface tension and $\Delta g_v \left(= -\frac{2\sigma}{r_c}\right)$ is the free energy change associated with the phase transition of the solute from liquid to hydrate phase.

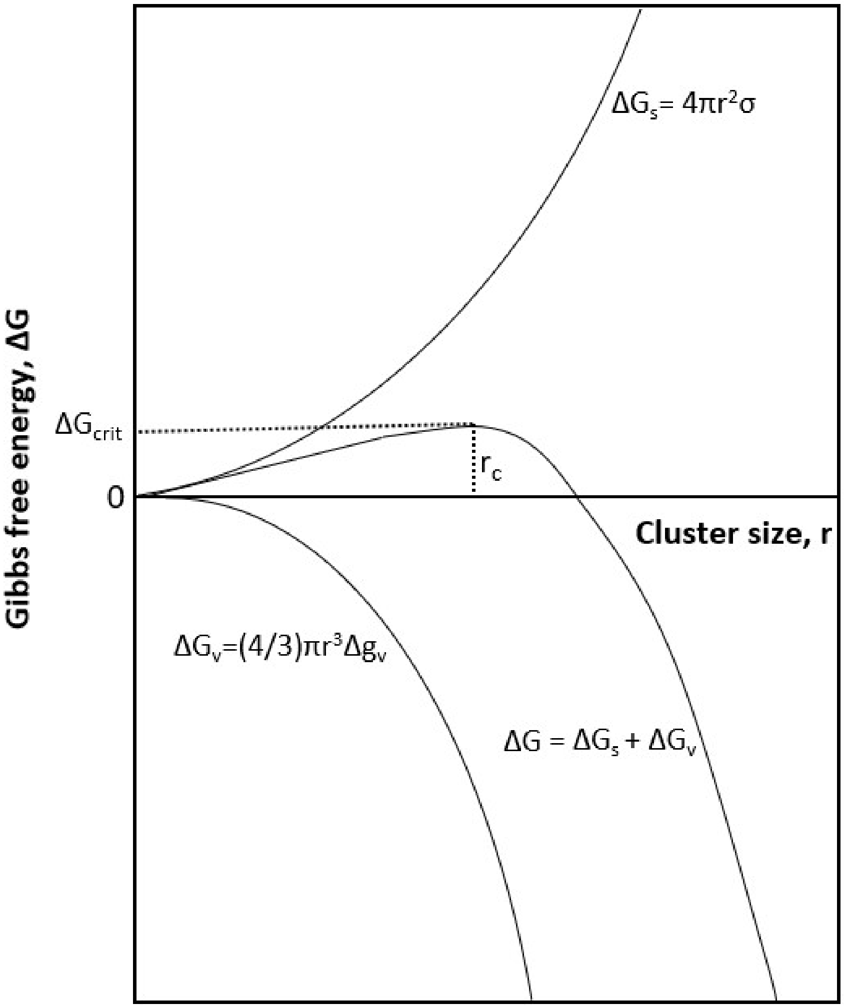

Figure 8. The Gibbs free energy versus cluster size for homogenous nucleation. The figure shows the critical cluster radius (r_c) necessary for spontaneous growth. The sum of the surface free energy and the volume excess energy yields the free energy. Figure reproduced from Larson and Garside (1986) and Sloan and Koh (2008).

Spontaneous growth for homogenous hydrate nucleation occurs when the cluster size radius, r_c, and the free energy barrier, ΔG_{crit}, reaches its maximum, as seen in figure 8. Equation 2 below described the relationship between homogenous nucleation (ΔG_{crit}) and heterogenous nucleation ($\Delta G'_{crit}$) where the difference lies in the factor, ϕ, that is dependent on the contact angle between the hydrate crystal and substrate:

$$\Delta G'_{crit} = \phi \Delta G_{crit} \qquad \text{Equation 2}$$

.The latter equation shows the increased probability of heterogenous nucleation due to the presence of substrates (e.g. particles and solid surfaces).

The time it takes for hydrates to grow to a size possible to detect with current technology is often referred to as the induction time or lag time. The induction time implies a metastable process, meaning that the solution can be at temperatures and pressures within the hydrate stability zone without nucleating (subcooling). Figure 9 shows the effect of subcooling in hydrates and ice. The effect of subcooling on hydrate formation with cyclopentane as hydrate former have shown that increased subcooling (i.e. lower temperature) increases the driving forces substantially (Corak et al., 2011).

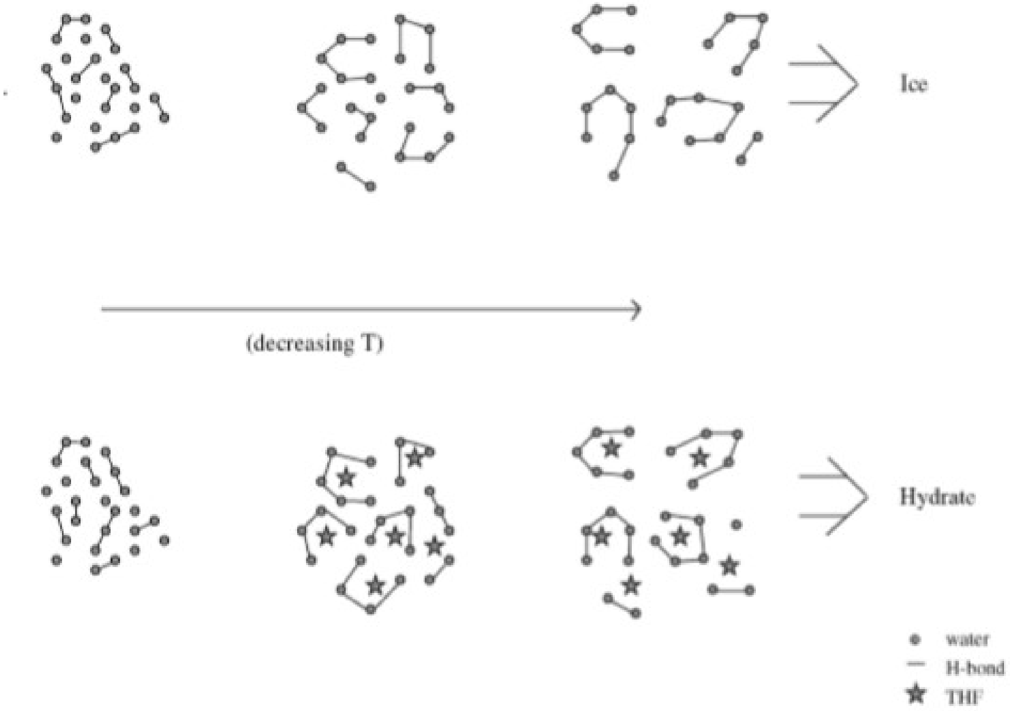

Figure 9. Hypothesis of hydrate nucleation versus ice. Illustration shows how the decreasing temperature changes the orientation and slows down the water molecules to orient themselves into crystal nucleus being able to form solid ice and capture guest molecule to form hydrate (Devarakonda et al., 1999).

2.1.5 Hydrate dissociation and inhibition

Prevention of hydrate formation plays a critical role in the oil industry where hydrates plug pipelines during transport and production of oil and gas from reservoirs. Several remediation methods are used for either complete prevention or inhibition. Thermal stimulation and depressurization are *physical dissociation* methods that changes the system conditions (pressure and temperature) whereas thermodynamic, low dosage hydrate inhibitors (LDHI) or Natural inhibitors are *chemical inhibitors* that affects the hydrate equilibrium line (Koh et al., 2010). These methods are described in detail in the following section below.

Physical dissociation:

Physical dissociation changes the system parameters (pressure and/or temperature) from inside the hydrate stability zone to outside, this can be seen from figure 10 where pressure reduction and temperature increase (shown in red and blue lines) will move the system from inside the hydrate formation region to outside, the hydrate free region. This thesis has used both depressurization and thermal stimulation to dissociate CO_2 hydrate in porous media in addition to methanol as thermodynamic inhibitor.

In the oil industry changing the pressure and temperature can be a challenge and therefore these methods are most commonly used in the laboratory while performing experiments. Insulation and dielectric heating on pipelines are thermal stimulation methods used in the oil industry to prevent hydrate formation (Kinnari et al., 2015).

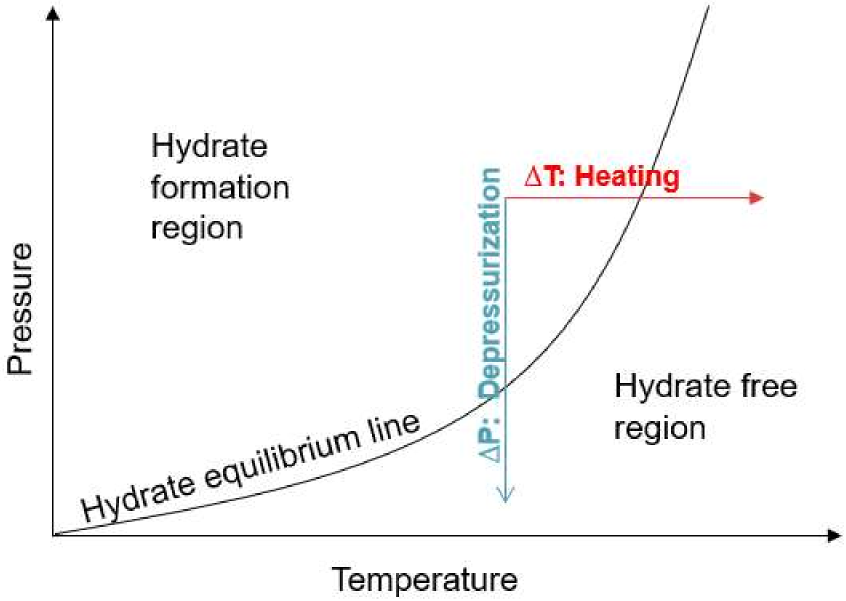

Figure 10. Phase diagram illustrates the hydrate equilibrium line with hydrate formation region on the left of the line and hydrate free region on the right. Figure illustrates that by changing the pressure and temperature the system can be moved from hydrate formation region to hydrate free region.

Chemical inhibitors:

Chemical inhibitors are widely used in the oil industry to prevent and control hydrate growth in pipelines during production or process operations. There are several different methods of chemical inhibition, one of these are **thermodynamic inhibitors** that changes the hydrate stability zone by moving the hydrate equilibrium line (i.e. by use of salts, alcohols or glycols). The mechanism behind the use of alcohols is the hydroxyl group of the alcohol bonding to the water molecules, leading to the hydrocarbon part of the alcohol arranging in such a way that free water is less available to form hydrates. In the oil industry alcohols are preferred relative to salts due to salt being a corrosive material and not suitable for use as inhibition of hydrate growth in pipelines and equipment. Figure 11 shows that by adding an alcohol (i.e. methanol (MeOH)) the equilibrium line for forming hydrates shifts further to the left, reducing the pressure and temperature area of the HSZ. This change in the equilibrium can then lead to hydrates not stable at in situ conditions (Kvenvolden, 1993). Figure 11 also shows that by addition of 30 % MeOH the hydrate formation region is outside the flowline conditions set as an example here.

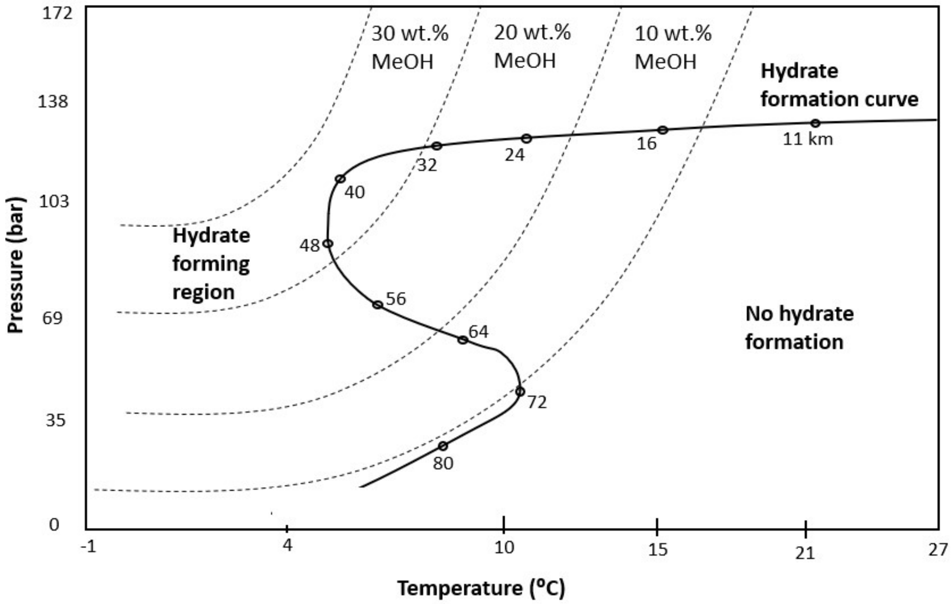

Figure 11. Hydrate formation PT-diagram with varying methanol concentration in free water for a given gas mixture. A gas flowline is shown as distance along the bold black line. Hydrate equilibrium line (stabled lines) are seen to vary dependent on MeOH concentration. Figure reproduced from Koh et al. (2010).

Another chemical inhibition method is the **Low Dosage Hydrate Inhibitors (LDHI),** that can be divided into kinetic inhibitors and anti-agglomerates. Kinetic inhibitors involve polymers suspended in water that can interrupt significant crystal growth whereas anti-agglomerates are long molecules having the capability of suspending small hydrate particles and preventing growth by making it difficult for hydrates that form to agglomerate and block pipelines. **Natural hydrate inhibitors (NHI)** involves polar compounds from crude oil (i.e. resins and asphaltenes) that stabilize water in oil emulsions making it difficult for hydrates to form since hydrates normally form at the interface of the water in oil emulsion (Koh et al., 2010, Fadnes, 1996). Several researchers at the Department of Chemistry at the University of Bergen have investigated the effect of NHI from crude oil on hydrate formation in pipeline and oil production processes in addition to the effect of petroleum acids on hydrate formation (Borgund et al., 2009, Erstad et al., 2009).

2.2 Occurrence and storage of gas hydrates

The most common hydrate former on earth is methane gas from biogenic (i.e. plant and animals from bacterial degradation at shallow depths) or thermogenic sources (i.e. kerogen from organic matter at high pressures and temperature deep in sediment). Natural gas hydrates can form where there are relatively high pressure, low temperature, water and guest gas molecule available. Methane is the most abundant hydrate former on earth and is mainly found in the arctic permafrost or ocean sediments (Figure 12).

Hydrate deposits in the permafrost regions are normally found at 300-800m water depth where organic carbon can accumulate rapidly (continental shelves/enclosed sea). In the ocean, hydrates are normally found between 1200- 1500m below the seafloor, and in both areas the hydrate stability zone follows the geothermal gradient, figure 12.

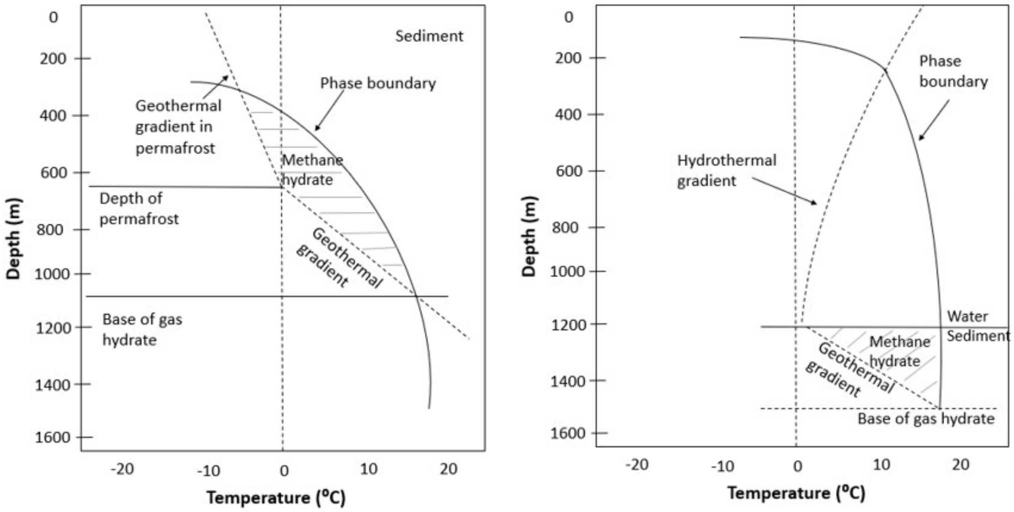

Figure 12. Hydrate stability region for the methane hydrate in a) permafrost and b) ocean sediments. Figure reproduced from (Sloan and Koh, 2008). Hydrothermal gradient is the change in temperature from ocean surface to seabed, whereas geothermal gradient is the change in temperature in formation. The methane hydrate stability zone is shown by the grey stapled lines.

Extracting gas hydrate from ocean or permafrost regions depend on the location and type of formation present. Hydrate deposits with high hydrate concentration are the most favorable locations (i.e. high hydrate saturation in sediments). Figure 13 below show different hydrate deposits around the world where the red dots indicates deposits deduced from seismic reflectors, yellow dots are direct samples taken by use of Remote Operated Vehicle (ROV) and red squares are production sites where methane gas has been successfully extracted (dissociated) from hydrate deposits. The Mallik, Messoyha and

Nankai fields are fields where methane gas has been successfully extracted from hydrate deposits in the sediment.

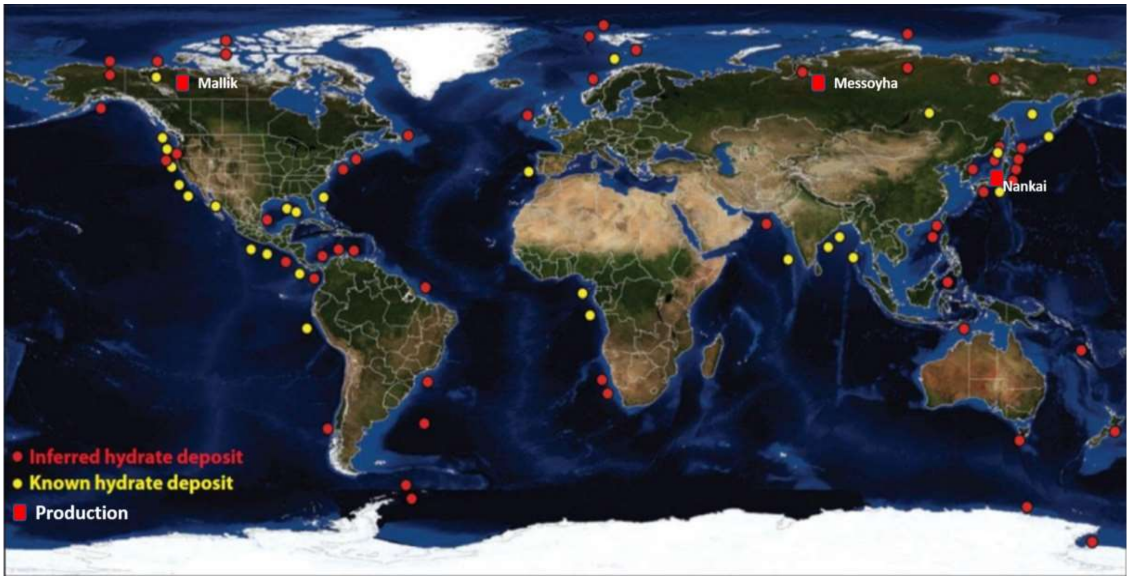

Figure 13. Worldwide distribution of documented hydrate deposits in the arctic and permafrost regions, figure modified from Hester and Brewer (2009). Inferred hydrate deposit: extracted from indirect data, mainly seismic reflectors and pore-water freshening in core sample. Known hydrate deposit: direct data (hydrate sample) obtained during drilling and Remote Operated Vehicle (ROV) expeditions.

The estimates of the amounts of natural gas hydrates in the earth subsurface vary significantly, but even the lowest estimates (figure 2) show that extracting methane gas from hydrate deposits can serve as an unconventional energy resource. The exchange reaction between CO_2/CH_4 is of particular interest, where CH_4 is being released by thermodynamically exchanged with the CO_2 hydrates. The department of Physics and Technology at the University of Bergen have done research on the CH_4/CO_2 exchange reaction in porous media by use of Magnetic Resonance Imaging techniques (Kvamme et al., 2007, Ersland et al., 2010, Baldwin et al., 2009). Exploiting these hydrate deposits for energy purposes and simultaneously injecting CO_2 for safe storage could be a unconventional energy resource in addition to limit the release of greenhouse gases into the atmosphere (Lee et al., 2003).

Storage of CO_2 as hydrates into geological formation or oceanic areas is a promising method of reducing the climate gases released into the atmosphere (Lal, 2008). Formation of CO_2 hydrates in geological areas within the HSZ depend on the formation composition, water, gas composition, electrolytes and organic matter present in the formation (Gauteplass et al., 2018). Research performed by Lamorena and Lee (2008) have investigated the effect of various electrolytes and soil surfaces on CO_2 hydrate formation in a pressurized vessel. They report shorter hydrate formation times for solutions without electrolytes and solutions containing solid particles (Bentonite, Kaolinite, Nontronite, Pyrite, Soil). For successful and rapid formation of CO_2 hydrate, various parameters affecting hydrate growth and in particular natural hydrate promotors are of interest.

Conventional CCS methods involve storage of CO_2 into depleted hydrocarbon reserves or cold aquifers (water reservoirs). The cold aquifers are of particular interest due to their location near the hydrate stability zone. Koide et al. (1995) have proposed to use CO_2 hydrates as a sealing mechanism for limiting the migration of liquid CO_2 injected into cold aquifers (i.e. CO_2 becomes supercritical at approximately 800m depth due to hydrostatic temperatures and pressures) upwards in the formation (Koide et al., 1995).

As described by Gauteplass et al. (2018) and Rochelle et al. (2009), the Gas Hydrate Stability Zone (GHSZ) is estimated to a thickness of 0,5 km on the western European shelves, making a great potential of CO_2 hydrate as a sealing mechanism for liquid CO_2 storage (Rochelle et al., 2009, Gauteplass et al., 2018). Furthermore, hydrate formation in conventional water reservoirs can, as described by Graue et al. (2007), have a negative or positive effect, where the formation of hydrates can be an challenge if the permeability is reduced and block further injection, but on the other hand hydrate formation can be positive if it prevents migration of dissolved CO_2 gas from upwards migration (Graue et al., 2007).

2.2.1 Environmental- and geohazards

Methane gas is 21 times more hazardous than carbon dioxide in terms of enhanced greenhouse effect when released into the atmosphere (Orszulik, 2008). This is due to the methane molecule absorbing thermal infrared (IR) photons emitted from the earth to a greater extent than carbon dioxide molecule and thus leading to a higher global warming effect in the atmosphere (Baird and Cann, 2012). The greatest mass extinction on earth is thought to be caused by methane gas released from hydrate deposits from the permafrost and shelf sediments at the end of Permian (Brand et al., 2016).

The general perception for years has been that uncontrolled emissions of methane gas from hydrate deposits around the world have the potential to increase the global temperature on the earth. However, studies performed by Ruppel and Kessler (2017) have shown that methane gas from hydrate deposits leaking from subsea formation does not reach the atmosphere as previously thought and consequently does not contribute to the global warming effect compared to the more direct emissions from human activities (Ruppel and Kessler, 2017).

“Hydrate formation in the sediment by replacing free water with solid hydrates will increase the shear strength of the formation and reduce the porosity and permeability” (Chopra et al., 2010). The integrity of the sediment when hydrates dissociates can in addition lead to geological hazards in the form of sediment failures, particularly on the seafloor (Kvenvolden, 1993, Maslin et al., 2010). A better understanding of how CO_2 hydrate will interact and behave during nucleation with liquids and sediment present in formation is important when addressing the possibility of using CO_2 hydrates as a sealing barrier for upwards migration of liquid CO_2 from cold aquifers. Moreover, formation of CO_2 hydrates for permanent storage in formation also require a broader understanding of the growth mechanism of hydrates in porous media.

2.3 Solid particle properties

Solid particles have a large surface area and they are reported to promote hydrate nucleation compare to bulk solutions due to the increase of available nucleation sites (Zhao et al., 2011). Molecules are attracted to each other by electrostatic forces (cohesive forces) and they are attracted to other molecules of adjoining fluids (adhesive forces). This cohesion and adhesion forces that a molecule experience determines its wettability. The wettability of the particles is of interest when investigating hydrate formation in the presence of solid particles with surfaces of different properties. Solid surfaces which are hydrophilic have an affinity for polar compounds (e.g. water, THF, CO_2) whereas hydrophobic solid surfaces have an affinity for non-polar compounds (e.g. CH_4, cyclopentane) (Barnes and Gentle, 2005). This thesis uses both oil-wet, intermediate- and water-wet particles to investigate the effect of wettability on hydrate formation. Figure 15 displays the various wetting properties of a system consisting of solid surface, water and oil.

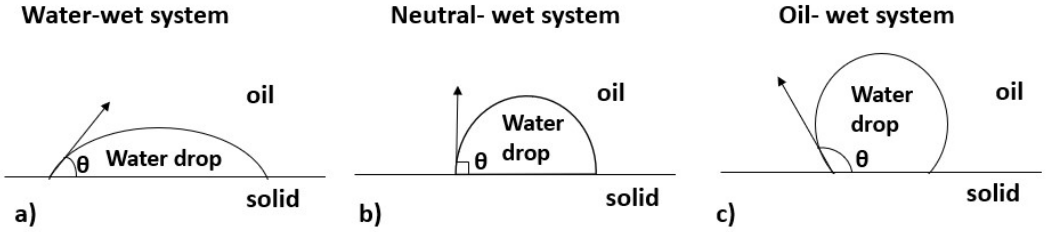

Figure 14. Various wetting properties of solid/water/oil system where a) water-wet system ($0<\theta<90^o$), b) neutral- wet system ($\theta=90^o$) and c) oil-wet system ($90<\theta<180^o$). Contact angle (θ) defines the wetting properties of the system.

A water-wet system is defined by the contact angle between the water droplet adhesion to the solid surface to be lower than 90^o, neutral-wet system where the contact angle is 90^o and oil wet-system where the contact angle is larger than 90^o and less than 180^o. Contact angle close to 0^o equals complete wetting and contact angle close to 180^o complete non-wetting (Kontogeorgis and Kiil, 2016).

The surface properties of solid particles can be studied by use of Magnetic Resonance Imaging (MRI) techniques. Studies performed by use of the MRI instrument for investigation of hydrate nucleation performed by Cheng et al. (2013) reports shorter induction times for CO_2 hydrate when silica glass bead particle size decreases (i.e. increased surface area), this reduction in induction time by the presence of particles is also observed for methane hydrate by Zhao et al. (2015). Observations of initial nucleation on the surface of the glass wall and on the particle surface moving inwards is reported by both Zhao et al. (2011) and Cheng et al. (2013) who analyzed THF and CO_2 hydrates formation in an MRI instrument, respectively. These articles also report that the subcooling effect is more significant than increased surface area of solid particles.

2.4 MRI imaging

Magnetic resonance imaging (MRI) offers a unique way of investigating clathrate hydrate formation and dissociation in porous media in addition to the macroscopic crystal structure (Yang et al., 2017). The MRI instrument consist of 5 main parts: static magnetic field (B_0), radio frequency system (RF) (transmitter and receiver), gradient coil, control electronics and a computer.

Since protons in molecules can be viewed as having a north and south pole, spinning in different direction with a net magnetism of 0, they will when being subjected to a static magnetic field (B_0) align with the magnetic field in either parallel-or anti parallel directions, as illustrated in figure 15, with a net magnetic moment in the direction of the magnetic field (B_0).

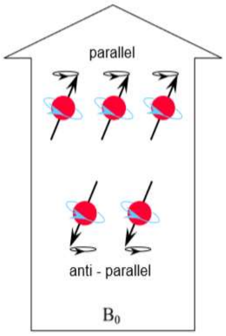

Figure 15. The net magnetization is in the direction of the static magnetic field (B0), figure from Blink (2004) .

The RF pulse in an MRI is used to excite the protons 90º or 180º away from the magnetic field (B_0), and when the RF pulse stops the relaxation of the protons back to their original distribution is measured through T1 and T2 relaxation times, often referred to spin-spin and spin-lattice relaxation, respectively.

The MRI instrument at Equinor's offices in Bergen has a magnetic field strength of 4,7 Tesla (T) and uses ^1H nuclei as image source. The magnet (B_0) is immersed in liquid helium to achieve superconducting properties and a homogenous field. Since the ^1H nuclei in the solid phase is undetectable due to short T_2 relaxation times, ice and hydrates will yield no signal intensity corresponding to black areas and liquid solutions will yield bright pixels.

The relationship between the magnetic field (B_0) effect on a nucleus and the angular frequency of rotation ω_0 of the nuclear spin can be described by the Larmor frequency:

$$\omega_0 = \gamma B_0 \qquad \text{Equation 3}$$

, where ω_0 is the angular frequency, γ is the gyromagnetic ratio (hydrogen has the highest gyromagnetic ratio of 42,6 MHz/T) and B_0 the magnitude of the magnetic field. The Larmor frequency is proportional to the static magnetic field (B_0) and the RF pulse necessary to excite the protons is determined from calculation of the angular frequency.

There are different measurement techniques by which an MR image is obtained, one of the methods are the RAREst (Rapid Acquisition with Relaxation Enhancement with Short echo Time) and this method contains the instructions of RF pulses, gradient pulses and timings necessary to obtain the desired image (Brown and Semelka, 2010). Details of the RAREst sequence is described in detail in earlier Master student theses (Eriksen, 2017, Tetlie, 2017). The exact parameters chosen for this thesis is described in section 3.2- MRI technique for visualization of the macroscopic crystal structure of THF hydrate.

3 Methods and experimental procedures

Three separate experimental methods are used to investigate the nucleation of clathrate hydrates of CO_2- and THF in different chemical environments. The first section, (3.1) describes the screening of THF hydrate formation in different chemical environments followed by section (3.2) that describes the MRI technique for visualization of the macroscopic crystal structures of THF hydrate and finally section (3.3) that described the experimental design used for CO_2 hydrate formation in Bentheimer sandstone cores.

3.1 The screening of THF hydrate formation in different chemical environments

Tetrahydrofuran (THF) was used as hydrate former in mixtures with either distilled water or Utsira formation water. Different solids were added to some of the solutions with varying wetting properties: oil-wet, water-wet, intermediate or untreated water-wet particles. The salinity of the solution was varied between 0, 3,2, 3,5 or 5,0 wt.% NaCl and Utsira formation water (approx. 3,2 wt.% salinity) was also used. The various samples were then placed in a refrigerator on a magnetic stirrer at desired temperature, figure 16. The magnetic stirrer was kept constant at 300 rpm for all experiments, this was used to promote hydrate growth and reduce induction time. All experiments were ended after 24 hours.

Observation of THF hydrate formation was done visually. The hydrate formation time must therefore not be confused with the induction time since this method of visual observation is not sufficiently, the precise formation time is used as an indication to which parameters affect hydrate growth the most. A web camera was used to register the hydrate formation times outside normal working hours. Parallel experiments were performed for each combination to increase reproducibility, where an average success rate was calculated for each combination based on how many parallel experiments yielded successful hydrate formation. In addition, the average hydrate formation time was calculated based on the successful experiments within each combination. All experiments were performed at the Department of Chemistry at the University of Bergen.

Figure 16. Experimental setup of THF hydrate formation in different chemical environments. Figure shows some of the samples placed on a magnetic stirrer in a pre-cooled refrigerator at desired temperature.

3.1.1 Preparation of samples

The liquid solutions of THF and H_2O/Utsira were prepared in batch mixtures at room temperature (22ºC) at different mole ratios and with various saline concentrations. For those experiments without solid particles added the various batch mixtures prepared were weighed into separate vials with approximately 40 g of liquid solution. For those experiments with solid particles the solids were first weighed into the vial (0,5 g or 1,0 g of solids) before the desired liquid solution was added (approximately 40 g of liquid solution). The various samples were then placed on a magnetic stirrer in a pre-cooled refrigerator at desired temperature.

The various combinations prepared of different mole ratios of H_2O/Utsira: THF, electrolytes and solids yielded in total 24 combinations that were investigated, listed in table 2. The magnetic stirrer used for the experiment was kept at 300 rpm for all experiments and the total amount of solid and liquid solution that were weighed in for each sample is listed in appendix C. Unless otherwise stated by an (*), the amount of solids that were added was 0,5 g.

Table 2. The different combinations of liquids and solid particles used for the THF hydrate formation experiments. All experiments performed at atmospheric pressures. The experiments conducted with solid particles contained 0,5 g of solids unless otherwise stated.

Combination nr.	Mole ratio (H_2O/Utsira: THF)	Electrolyte (wt.% NaCl)	Solids	Experimental temperature (^{0}C)
1	17 H_2O: 1 THF	0,00	-	0/2
2	17 H_2O: 1 THF	3,50	-	0/2
3	17 H_2O: 1 THF	0,00	SiO_2	2
4	17 H_2O: 1 THF	0,00	SiO_2*	2
5	17 H_2O: 1 THF	3,50	SiO_2	2
6	17 H_2O: 1 THF	3,50	SiO_2*	2
7	17 H_2O: 0,33 THF	0,00	-	2
8	17 H_2O: 0,33 THF	0,00	SiO_2	2
9	17 H_2O: 0,66 THF	0,00	-	2
10	17 H_2O: 0,66 THF	0,00	SiO_2	2
11	17 H_2O: 1 THF	0,00	CN-EC	2
			CN-nonEC	
12	17 H_2O: 1 THF	0,00	C18	2
13	17 H_2O: 0,66 THF	0,00	CN-nonEC	2
14	17 H_2O: 0,66 THF	0,00	C18	2
15	17 H_2O: 1 THF	5,00	-	2
16	17 H_2O: 1 THF	5,00	SiO_2	2
17	17 H_2O: 1 THF	5,00	SiO_2*	2
18	17 H_2O: 1 THF	3,50	CN- EC	0/2
			CN-nonEC	2
19	17 H_2O: 1 THF	3,50	C18	2
20	17 H_2O: 1 THF	0,00	Bentheimer	2
21	17 H_2O: 1 THF	3,50	Bentheimer	0
22	17 Utsira: 1 THF	3,20	-	0
23	17 Utsira: 1 THF	3,20	Bentheimer	0
24	17 H_2O: 1 THF	3,50	-	0

* 1,0 g of SiO_2 added.

3.1.2 Materials and equipment

Description of the various materials and equipment used for the THF screening experiments is listed in table 3 and 4 below. Both intermediate (CN) and C18 solid particles are chromatography solid phase particles with a defined surface corresponding to intermediate-and oil wet, respectively. The untreated water-wet Bentheimer sandstone core was ground at the University of Bergen and is the same sandstone material as from the CO_2 hydrate formation experiments and the MRI experiments with THF hydrate.

Table 3. Solids and liquids used in THF screening experiments. Table describes manufacturer, empirical formulae and different physical properties of the solids and liquids used.

Solids

Name	Specifications	Supplier	Particle size (µm)	Empirical formula	Wetting properties
Si60/SiO_2	LiChroprep Si60	Merck	40-63	SiO_2	Untreated, water-wet
CN-EC	Discovery DSV-CN SPE, CN (Cyano)-EC	Sigma Aldrich	50	$SiO(CH_2)_3CN$	Intermediate
CN-nonEC	Isolute SPE column CN (Cyano) -nonEC	Biotage	50	$SiO(CH_2)_3CN$	Intermediate
C18	Hypersep C18	Thermo Scientific	40-60	C18	Oil-wet
Bentheimer	Bentheimer sandstone core, quartz (SiO_2)	UIB	150-212	SiO_2	Untreated, Water-wet
NaCl	Sodium chloride > 99,5%	Emisure	-	NaCl	-

Liquids

Name	Specifications	Supplier	Density (g/ml) at 20°C	Empirical formula	Molar mass (g/mol)
THF	Tetrahydrofuran anhydrous >99,9%	Sigma Aldrich	0,889	C_4H_8O	72,11
THF	Tetrahydrofuran anhydrous >99,9% with inhibitor (250 ppm BHT)	Sigma Aldrich	0,889	C_4H_8O	72,11
Water	Deionized water	UIB	0,998	H_2O	18,01
Utsira	Utsira formation water, 3,2 wt.% electrolytes	Utsira reservoir	-	-	-

Table 4. Equipment used in the THF screening experiments. Further details of the uncertainties for the equipment is listed in Appendix A.

Name	Specification	Supplier
Vials	Vials 60ml with snap on cap	Sigma Aldrich
Stirring bars	Cylindrical stirring bars 25 x 6 mm	VWR
Refrigerator	Master cella ir33 LED display for temperature monitor and control	Carel
Magnetic stirrer	IKA werke RO 10 power magnetic stirrer with 10 plates, 0-1100 rpm	IKA
Thermometer	Digitron Thermometer, -50°C to +750°C	Digitron
Weighing scale	Kern precision balance weighing scale, uncertainties of ± 0,005 g	KERN

The molecular structure of silica C18 chromatography solid phase material used in this thesis is shown in figure 17 below.

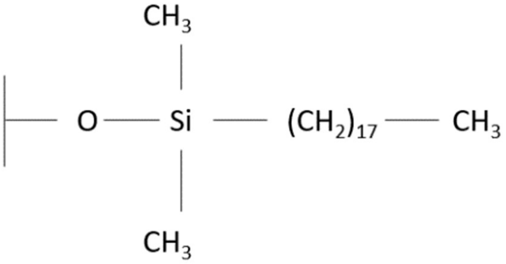

Figure 17. Molecular structure of silica C18 chromatography solid phase material.

The silica CN chromatography solid phase material used had either the presence of OH groups (non endcapped) or they were reacted to -OCH_3 (endcapped). Structures are shown in figure 18 below.

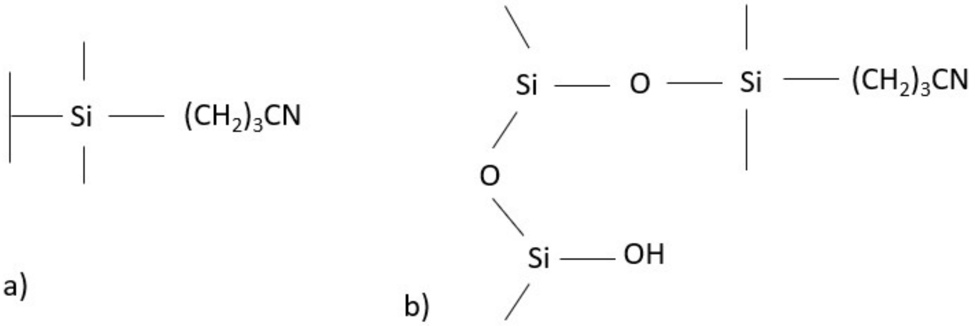

Figure 18. Molecular structure of silica with a) CN endcapped (Sigma) and b) CN non-endcapped (Biotage) chromatography solid phase material.

Utsira formation water was kindly supplied by Sandra Eidnes and Hilde Aleda Weber from Oseberg South. When the formation water arrived, it was stored at -30ºC to avoid any growth of organisms in the water. The total saline composition of the solution is described in table 5 below and a 3,2 wt.% saline solution was assumed when mixing the formation water with THF. In addition to saline constituents, the formation water contained substances that are naturally occurring in water reservoirs and visible particles were seen. Other articles suggest a slightly salinity of the Utsira formation water (3,0 wt.% salt) and demonstrates that the exact composition will vary dependent on when the sample is taken and from which well (Fleming et al., 2007).

Table 5. Saline composition of Utsira formation water from Oseberg South, data obtained from "Detection and quantification of Utsira formation water in production wells of the Oseberg South Field and impact on scale management" (McCartney et al., 2010).

Constituents	Concentration (mg/l)
Na	10728
K	331
Mg	800
Ca	482
Sr	13,2
Ba	0,2
Cl	19400
Total	31754,4

The average temperature in the samples under the experiment was measured by registering the temperature changes in a water solution from room temperature to desired experimental temperature. This cooling gradient is shown in figure 19 below and shows that temperature stabilizes at around 2ºC within 40 minutes.

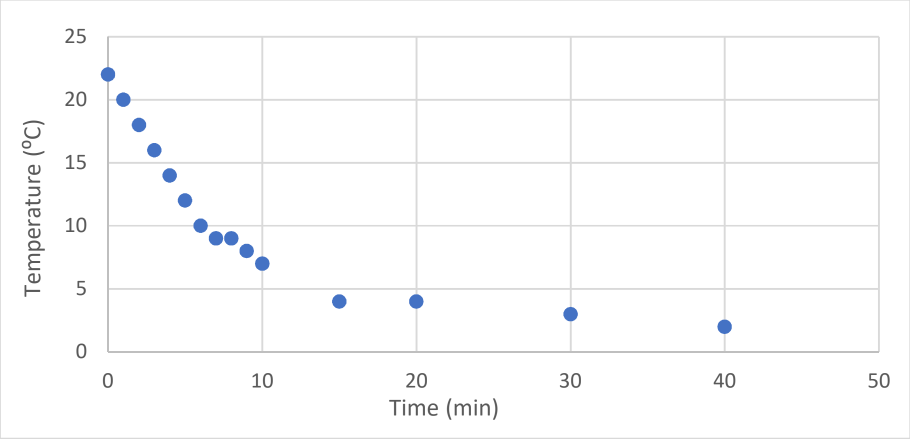

Figure 19. Cooling gradient for samples in refrigerator from room temperature to experiment temperature. Samples used an average of 40 minutes from room temperature to experimental conditions when placed in the refrigerator.

3.2 MRI technique for visualization of the macroscopic crystal structures of THF hydrate

The magnetic resonance imaging (MRI) instrument at Equinor's offices in Bergen was used for visualization of the macroscopic crystal structure and morphology of THF hydrate with small amounts of particles added.

The MRI instrument (figure 20) contains a superconductive magnet with a field strength of 4.7 Tesla (T). The instrument uses hydrogen as image source and since ^{1}H nuclei in the solid phase is undetectable due to short T_2 relaxation times, both ice and hydrate solid structures will not give any signal intensity (corresponding to black pixels on image). Liquids containing hydrogen will send a bright signal intensity back corresponding to white pixels. The signal intensity obtained from the MRI instrument is shown to decrease as the THF hydrate saturation increases (Liu et al., 2010).

Figure 20. The MRI instrument at Equinor in Bergen.

3.2.1 Preparation of samples

Tetrahydrofuran (THF) and deionized water from Equinor facilities in Bergen was used to prepare a 500ml solution containing 17 moles of H_2O and 1 mole of THF, the ideal hydration number. The solution was then weighed into small sample glasses (with lid), approximately 15-20 g of liquid solution in each sample before a small spatula spoon of solids was added to the desired solutions before placing the samples into the freezer at -10ºC. Caution was used to avoid any shaking or movement on the samples to make sure the hydrates formed were from static conditions without any external energy supplied. Samples with distilled water with and without particles were also prepared to compare crystal structure of ice with THF hydrate.

Table 6 below shows the different combinations prepared and at which temperature the hydrate/ice was formed at. The refrigerator was set to -10ºC for rapid hydrate growth and after successful hydrate formation the refrigerator was set to -2ºC to reduce the time necessary in the MRI instrument when sample melts. There were three parallels performed for each combination to insure statistics and increase reproducibility.

Table 6. The various combinations prepared of THF hydrate and ice for MRI imaging. After successful hydrate formation the temperature was raised to -2ºC for reducing time in MRI instrument during melting.

Combination nr	Composition	Solids	Ice/hydrate formation temperature (ºC)
1	Distilled water	-	-10
2	Distilled water	Bentheimer	-10
3	17 H_2O: 1 THF	-	-10
4	17 H_2O: 1 THF	Illite mineral	-10
5	17 H_2O: 1 THF	Oil-wet SiO_2	-10
6	17 H_2O: 1 THF	Water-wet SiO_2	-10
7	17 H_2O: 1 THF	Bentheimer	-10

3.2.2 MRI method

Operation of the MRI instrument and settings chosen was done with and under the supervision of Per Fotland at Equinor. The MRI instrument was first tuned and matched by using the Wobbling function before the Localizer function was used to set the location of the sample in the instrument. Based on earlier master student work done by Eriksen (2017) with THF hydrate melting in the MRI instrument, the following settings were chosen for the RAREst protocol:

- Echo time (TE): 5,02 ms (exception for combination nr. 3 that used an Echo time of 4,5 ms)
- Repetition time (TR): 3000 ms
- Rare factor (RF): 1
- Slices: 60
- Field of view: non-continuous
- Image size: 140 x 140
- Slice orientation: axial

The RAREst protocol was run three times for each series yielding a total of 1,5 hours in the MRI instrument. The three separate RAREst images obtained for each series represents a gradual melt. Figure 21 below shows the axial distribution of the three parallel samples divided into 60 slices.

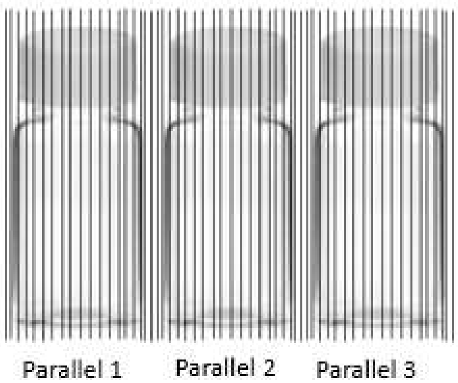

Figure 21. Axial slice distribution for the parallel solutions scanned with the RAREst protocol. 60 slices where distributed across the three parallel solutions to cover the samples with approximately 20 slices representing one parallel. This figure is not accurate and only a representation of slice distribution.

The RAREST images obtained from the experiments were extracted from ParaVison in DICOM-files and processed in MATLAB by Per Fotland. Since solid phases will not give any signal, the black areas are solid phases (ice or hydrate) and bright areas are liquids (THF or H_2O). The particles added to the solution was not suspended in the solution but positioned at the bottom of the vial due to gravitation, meaning that black pixels seen in the solution represents solid ice or hydrates and not solid particles.

The images obtained from ParaVision and processes in MATLAB should have been modified in such a way that the intensity scale for each image series are the same, meaning that the intensity in one figure might be slightly different in another since this factor has not been corrected for. Based on this only a general comparison between the experiments will be presented.

3.2.3 Materials and equipment:

Materials and equipment used for the MRI experiment is listed in table 7 and 8.

The oil-and water-wet quartz sand from Equinor have been prepared from untreated quartz sands by an earlier master student, details of this procedure and specification of quarts sand can be view in her thesis (Tetlie, 2017). The Bentheimer sandstone used for these experiments are the same sandstone as from section 3.3 (CO_2 hydrate formation in Bentheimer sandstone core) and 3,1 (the screening THF hydrate formation in different chemical environments). Bentheimer sandstone consist mainly of Quarts (SiO_2) but also of other components. Table 9 shows an XRD analysis performed by an earlier master student on a similar Bentheimer sandstone core, here it can be seen that Illite is one of the minerals present (Riisøen, 2012).

Table 7. Solids and liquids used for the MRI experiments. Table describes manufacturer, empirical formulae and different physical properties of the solids and liquids used.

Solids					
Name	**Specifications**	**Supplier**	**Particle size (µm)**	**Empirical formula**	**Wetting properties**
Water-wet SiO_2	NC4X modified quartz sand	Equinor	Unknown	SiO_2	Water-wet
Oil-wet SiO_2	NC4X modified quartz sand	Equinor	Unknown	SiO_2	Oil-wet
Bentheimer	Bentheimer sandstone core, quartz (SiO_2)	UIB	150-212	SiO_2	Untreated water-wet
Illite	Mineral	Equinor	Unknown	Unknown	Unknown
Bentheimer	Bentheimer sandstone, quartz (SiO_2)	UIB	150-212	SiO_2	Untreated water-wet
Liquids					
Name	**Specifications**	**Supplier**	**Density (g/ml) at 20°C**	**Empirical formula**	**Molar mass (g/mol)**
THF	Tetrahydrofuran anhydrous >99,9%	Merck, Equinor	0,889	C_4H_8O	72,11
Water	Deionized water	Equinor	0,998	H_2O	18,01

Table 8. Equipment used for the MRI experiments.

Name	**Specification**	**Supplier**
Vials	Vial with screw lid	Equinor
MRI	BRUKER BioSpec 47/40 USR (Ultra Shielded and Refrigerated magnet) with superconducting magnet	Equinor, Bruker
Refrigerator	Panasonic MIR-554-PE cooled incubator	Panasonic
Weighing scale	Mettler PK 2000 scale, uncertainties of ± 0,01 g	Mettler Toledo

Table 9. Mineral composition of Bentheimer sandstone core from XRD analysis performed by earlier master student (Riisøen, 2012).

Mineral	**Molecular formula**	**Contents (± 0,1%)** *
Illite/Smectite	-	TR
Illite + Mica	$(K, H_3O) (Al, Mg, Fe)_2(Si, Al)_4O_{10}[(OH)_2(H_2O)]$	3,2
Kaolinite	$Al_2Si_2O_5(OH)_4$	0
Chlorite	ClO_2^-	0
Quartz	SiO_2	90,6
K Feldspar	$NaAlSi_3O_8$-$CaAl_2Si_2O_8$	4,6
Calcite	$CaCO_3$	0,6
Dolomite	$CaMg(CO_3)_2$	0
Siderite	$FeCO_3$	1
Pyrite	FeS_2	TR

*TR: trace amounts.

3.3 CO_2 hydrate formation in Bentheimer sandstone cores

The following section provides a detailed description of the experimental procedure and equipment used for the CO_2 hydrate formation in the Bentheimer sandstone cores. In addition, the core preparations including permeability- and porosity measurements are described. The experimental setup for all experiments were identical and a total of nine experiments was performed.

3.3.1 Experimental setup:

A process flow diagram for the experimental setup used for the CO_2 hydrate formation in a sandstone core is shown in figure 22 below. All experiments were conducted at the department of Physics and Technology at the University of Bergen in cooperation with Jarand Gauteplass and Stian Allmenningen. Based upon the results from the simulation program PVT sim Nova 2 the pore pressure was set to 70 bar to keep within the hydrate stability zone for CO_2 when regulating the temperature between 4-7 ^{o}C (Figure 6 shows the phase diagram of CO_2 hydrate in section 2.1.3). The fluids injected into the core under each of the experiments were in liquid form.

High pressure pumps used for injecting or rejecting the different liquids (CO_2, brine, MeOH) were of type ST Sigma 1000. The high-pressure pumps were set to a maximum pressure of 90 bar due to safety risks associated with high pressure. Swagelok stainless steel valves were used throughout the system. The confinement pressure pump was of type Teledyne ISCO pump. High pressure valves and tubings (1/8in.) were used throughout the system. Two ESI-USB pressure transducers were mounted on the inlet and outlet side of the core holder to register the pressure change across the core. One Multilogger Thermometer HH506RA recorder was mounted on a three- way valve on the inlet side of the core holder to register the temperature. Two resistance recorders were manually connected on the inlet and outlet side of the core unit. Equilibar Back Pressure Regulator (BPR) was set to 70 bar to regulate the pressure inside the core and release liquid/gas when exceeding 70 bar. On the outlet side of the BPR a graduated cylinder collected the produced liquid. Uncertainties for the equipment and instrument used is listed in appendix A.

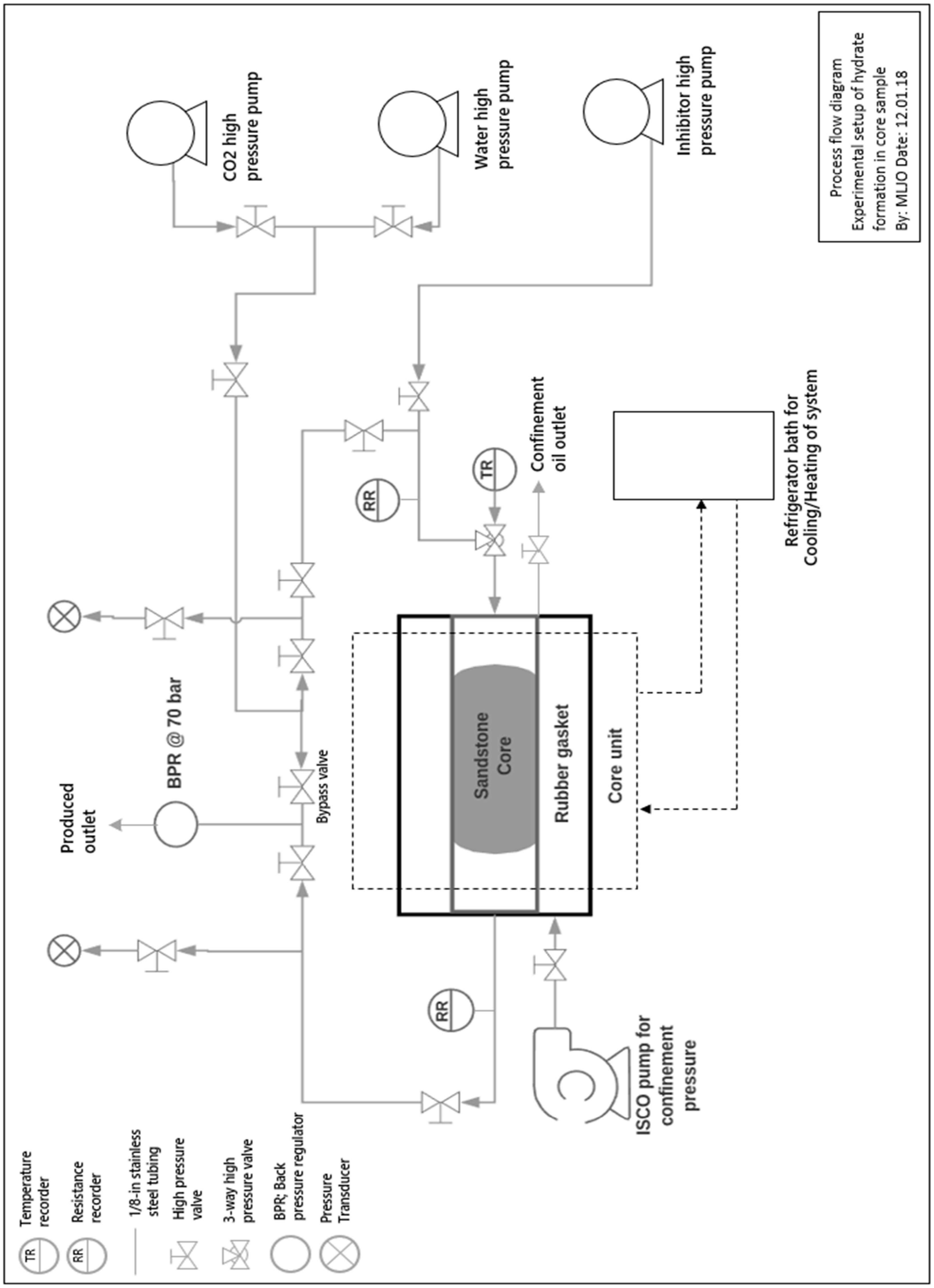

Figure 22. Process flow diagram showing experimental setup of hydrate formation in core sample. The core unit is surrounded with confinement oil and cooling system. Three different ST stigma high pressure pumps were available to inject/reject liquids through opening/closing of desired valves. One ISCO pump was used for creating the confinement pressure around the core unit. Two ESI-USB pressure transducers and two pressure recorders were mounted on the inlet and outlet side of core unit. The Mulitlogger thermometer recorder was mounted on the three-way valve on the inlet side of the core unit. The BPR (back pressure regulator) was set to constant 70 bar under all experiments. On the outlet of the BPR a graduate cylinder collected liquids when pressure exceeded 70 bar.

3.3.2 Core preparations:

The Bentheimer sandstone cores used for the experiments was collected from a quarry in Germany. Both permeability and porosity was measured for equivalent cores by Graue et al. (2008) to 22% and 1.1 Darcy, respectively.

The first preparations consisted of cutting the cores into 15 cm length and 5 cm diameter, see figure 23, before washing and drying the cores in a heating cabinet (@ 69ºC) for minimum 24 hours to ensure that no moisture was left before weighing. The length and diameter were measured three times each and the mean value used for porosity calculations. Saturation of the core was done by standard vacuuming procedure (Berge, 2017) with the desired brine solution (distilled water and either 3,5, 5,0 or 7,0 wt.% sodium chloride (NaCl>99,5%)). The dry weight of the core and saturated weight of the core was used to calculate the porosity. Average porosity for all cores were calculated to 22%, ref. appendix B for calculations.

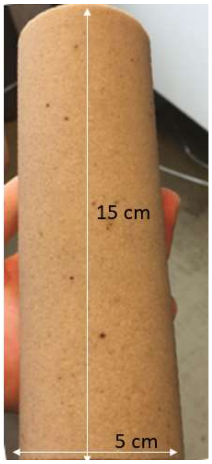

Figure 23. Saturated sandstone core with measurements.

After the core was saturated with desired brine solution it was mounted into the Hassle core holder by first threading a Viton sleeve onto the core and then placing it inside the cylindrical core unit (Figure 24 for details). When the core was mounted inside the Hassle holder and end pieces connected at the top and bottom were connected, confinement oil was injected on the outside of the Viton sleeve (Figure 24c). This was to create a confinement pressure around the rubber sleeve so that all liquids injected were forced through the saturated core. The confinement pressure was set to 30 bar above the desired pore pressure (70 bar). Once the core was successfully mounted the desired brine solution was injected from the high-pressure pump until pore pressure reached 70 bar and a steady flow was established for the brine solution.

The permeability measurements of the cores were performed at 70 bar and room temperature with the following injection rates of brine solution: 10, 20, 40 and 60 ml/min. Average permeability for all cores was calculated to 1,3, ref. appendix B for details of permeability calculations. After the permeability measurements were completed the system was cooled for 24 hours to reach the target temperature for the experiment.

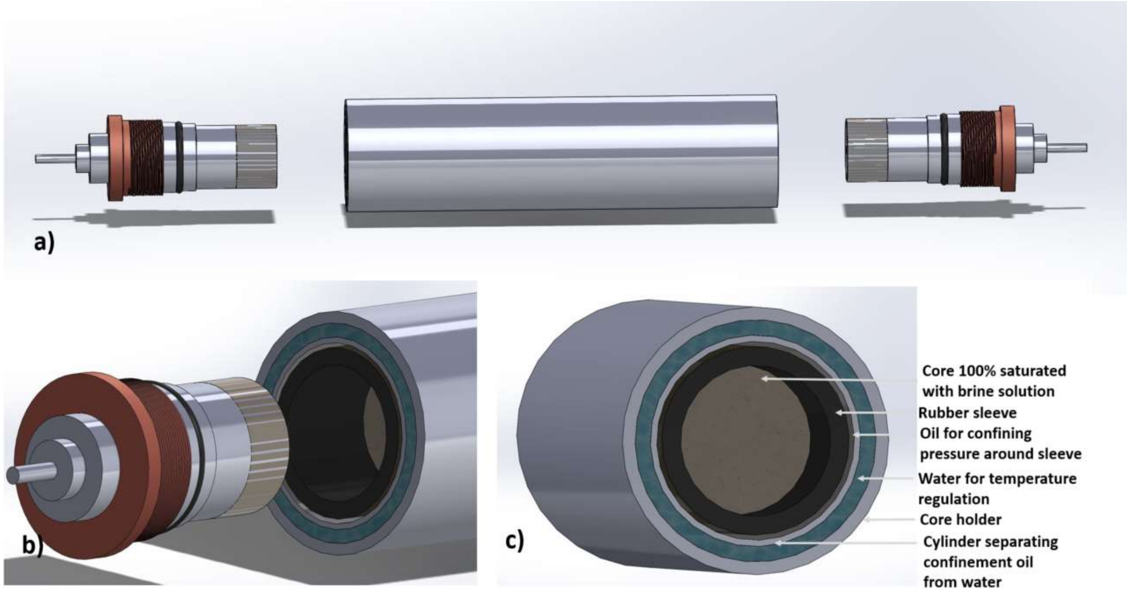

Figure 24. 3D illustration made in SolidWorks showing from top left a) Hassle core holder with end pieces, b) how end piece is placed inside core holder and c) how saturated core is surrounded by one Viton rubber sleeve, oil for confining pressure and water for temperature regulation.

3.3.3 CO_2 hydrate formation procedure:

The experiments were performed with a pore pressure of 70 bar and temperature regulated to either 4,0, 5,0 or 7,0ºC. Injection rate, temperature and pore pressure were logged continuously by the computer in the lab. Temperature logging was only performed for some of the experiments due to sensor breaking and difficulties repairing it, but was assumed to be constant and controlled by cooling bath. Resistivity measurements needed to be logged manually. The injection rate of CO_2 was either 0,5, 5 or 10 ml/min, depending on which experiment ongoing. Three baseline experiments were performed at the different injection rates to ensure reference values for resistivity and permeability without CO_2 hydrate present in the core. Due to long induction time for some of the experiments a web camera was set up to register the resistivity outside normal working hours.

In total nine experiments completed; including three baseline experiments.

During injection of CO_2 the hydrate formation in core was verified by observing a temperature increase (due to hydrate formation being an exothermic process) in combination with resistivity-and pressure increase. When the pressure reached 80-85 bar the injection of CO_2 was stopped due to safety concerns. The pressure decrease after this point was due to CO_2 being encapsulated inside the water molecules forming hydrates and consequently lowering the pressure. Both the pressure increase, and pressure decrease can be viewed as CO_2 hydrate formation inside the core.

3.3.4 Dissociation of formed CO_2 hydrate plug in the core

Dissociation of the formed hydrate plug was performed by either pressure reduction, chemical injection (30 wt.% MeOH), thermal stimulation or a combination of these methods. The dissociation of the formed hydrate plug started with disconnecting the CO_2 pump and connecting the water pump. The water pump was then set to receive fluid so that all liquid/gases formed from dissociation could be collected in the water pump and safely disposed. The water pump was set to 70 bar so that when CO_2 gas dissociated from the plug the water pump expanded as more and more gas were collected. When pressure was used as dissociation method the pressure was gradually reduced until no more pressure inside the core and complete dissociation of formed plug. When chemical-or thermal methods were used the pressure was kept constant until no more CO_2 gas dissociated from core. The confinement pressure was kept at 30 bar above the pore pressure until no pressure remained. The remaining residual pressure was air vented.

3.3.5 Materials

The solids and liquids used for the CO_2 hydrate formation experiments in the sandstone cores are listed in table 10, including chemical-and physical properties.

Table 10. The solids and liquids used for the CO_2 hydrate formation experiments.

Solids					
Name	**Specifications**	**Supplier**	**Empirical formula**	**Wetting properties**	
Bentheimer	Bentheimer sandstone core, quartz	UIB	SiO_2	Untreated water-wet	
NaCl	Sodium chloride > 99,5%	Emisure	NaCl	-	
Liquids					
Name	**Specifications**	**Pressure (bar)**	**Temperature (°C)**	**Density (g/ml)**	**Viscosity (cP) at 21°C**
CO_2	Carbon dioxide > 99,999 %	70	21	0,798 1)	0,0702 1)
			7	0,913 1)	0,0952 1)
			4	0,932 1)	0,1005 1)
Water	Deionized water	STP	STP	0,998	-
Brine A	3,5 wt.% NaCl	70	21	-	1,07 1)
			7		
			4		
Brine B	5,0 wt.% NaCl	70	4	-	-
Brine C	7,0 wt.% NaCl	70	4	-	-
Methanol	MeOH	-	-	-	-

1) Data collected from NIST chemistry webbook (Chemistry web book, 2017).

4 Results and discussion

4.1 Overview

This chapter presented the experimental results from the three different methods used in this thesis. The first experiments presented in this section, section 4.2, involves THF as hydrate former, where numerous experiments were performed at atmospheric pressures for a broad screening of the various parameters affecting hydrate formation. These results include the effect of change in both the temperature, electrolyte concentration, mole ratio and addition of solid particles with varying wetting properties. This method allowed for performing many parallel experiments for the different combinations investigated. The next section, section 4.4, presents the results from the MRI analysis of the macroscopic crystal structure of THF hydrate. Results include the effect of addition of solid particles with varying wetting properties on THF hydrate formation. In addition, experiments with pure ice was also performed for comparison of the macroscopic crystal structure of ice with THF hydrate structure. Finally, the results from the experiments with CO_2 as hydrate former in Bentheimer sandstone cores are presented, section 4.6. The effect of change in CO_2 injection rate, electrolyte concentrations and temperature change are presented. Furthermore, the resistivity and pressure change due to CO_2 hydrate growth are also presented.

4.2 Results- The screening of THF hydrate formation in different chemical environments

The screening of THF hydrate involved >100 different experiments performed in different chemical environments. The change in THF hydrate formation time and growth due to the addition of solids with varying wetting properties, temperature- and composition changes was investigated. All experiments were performed at atmospheric pressure.

The experiments with several parallels within one series are presented with average values, meaning that if 5 experiments yielded THF hydrates out of 10 experiments the average success rate was calculated to 50 %. The average hydrate formation time for these experiments were also calculated, but due to the stochastic nature of hydrate formation, the average hydrate formation time for each combination varied considerably if one of the experiments deviated considerably form the others. Table 11 below shows the standard deviation for the various combinations that were performed with three or more parallels. The table shows, in red, that some of the standard deviations exceeds the average hydrate formation time calculated. To give an appropriate average hydrate formation time for each combination these "outliers" were removed, and the corrected average hydrate formation time is used for the rest of this thesis.

Table 11. Standard deviations for the combinations performed with more than three parallel experiments and corrected average hydrate formation based on outliers.

Combination	Temperature (°C)	Average hydrate formation time (hr) ± 0,5 hr	STD. dev	Corrected average hydrate formation time (hr) ± 0,5 hr	STD. dev corrected
1	-5	0,23	0,137	-	-
	0	0,75	0,000	-	-
	2	7,67	9,385	2,25	0,353
2	0	7,70	12,220	7,92	8,817
	2	19,25	0,354	-	-
3	2	8,67	11,117	2,25	0,353
5	2	14,33	8,520	-	-
11[1]	2	3,56	1,944	-	-
18[2]	2	3,67	1,443	-	-
21	0	2,54	1,525	-	-
22	0	3,73	5,857	2,44	2,457
23	0	2,36	2,169	-	-
24	0	2,0	0	-	-

[1] Combination involving CN-EC.

[2] Combination involving CN-nonEC

A summary of the different combination performed with THF as hydrate former is shown in table 12. The table shows an overview of the number of experiments performed for each combination in addition to the overall successful hydrate formation and average hydrate formation time. Experimental uncertainties for the experiments performed are described in Appendix A.

The following sub-sections below are divided into five main categories:

- Change in temperature
- Change in electrolyte concentration
- Change in mole ratio of solution
- Addition of solids with varying wetting properties:
    - Oil-wet (C18)
    - Untreated water-wet (Bentheimer, SiO_2)
    - Intermediate wet (CN-EC/nonEC)
- THF hydrate growth

The hydrate formation time for each experiment was observed visually or by use of a web camera. When the web camera was in use it was more challenging to observe the first initial THF hydrate crystals and therefore a deviation of ± 0,5 hours was set to account for this. The results from these experiments should be used as an indication of the hydrate formation time and differences in success rate depending on the various variables chosen. Additional uncertainties investigated is discussed in detail in appendix A.

Table 12. Summary of the different combinations performed, and amount of experiments performed for each combination.

Nr	Composition (H_2O/Utsira: THF)	NaCl (wt.%)	Solids	Temperature (°C)	Nr. of experiments	Successful hydrate formation (%)	Corrected Average hydrate formation time (hr) ± 0,5
1	17 H_2O: 1 THF	0,0	-	-5	4	100,0	0,23
				0	5	100,0	0,75
				2	6	66,7	2,25
2	17 H_2O: 1 THF	3,5	-	0	5	100	7,92
				2	10	20,0	19,25
3	17 H_2O: 1 THF	0,0	SiO_2	2	3	100,0	2,25
4	17 H_2O: 1 THF	0,0	SiO_2*	2	1	100,0	19,0
5	17 H_2O: 1 THF	3,5	SiO_2	2	7	75,0	14,3
6	17 H_2O: 1 THF	3,5	SiO_2*	2	1	100,0	5<hr<24[1)]
7	17 H_2O: 0,33 THF	0,0	-	2	2	0,0	No hydrate formation
8	17 H_2O: 0,33 THF	0,0	SiO_2	2	2	0,0	No hydrate formation
9	17 H_2O: 0,66 THF	0,0	-	2	2	0,0	No hydrate formation
10	17 H_2O: 0,66 THF	0,0	SiO_2	2	2	50,0	4,5
11	17 H_2O: 1 THF	0,0	CN-nonEC	2	1	100,0	3,0
			CN-EC	2	9	100	3,56
12	17 H_2O: 1 THF	0,0	C18	2	1	100,0	23,0
13	17 H_2O: 0,66 THF	0,0	CN-nonEC	2	1	0,0	No hydrate formation
14	17 H_2O: 0,66 THF	0,0	C18	2	1	100,0	3,0
15	17 H_2O: 1 THF	5,0	-	2	2	0,0	No hydrate formation
16	17 H_2O: 1 THF	5,0	SiO_2	2	2	0,0	No hydrate formation
17	17 H_2O: 1 THF	5,0	SiO_2*	2	1	0,0	No hydrate formation
18	17 H_2O: 1 THF	3,5	CN-EC	0	1	0	No hydrate formation
			CN-EC	2	6	0	No hydrate formation
			CN-nonEC	2	3	100,0	3,67
19	17 H_2O: 1 THF	3,5	C18	2	1	100,0	4,5
20	17 H_2O: 1 THF	0,0	Bentheimer	2	2	100,0	1,5
21	17 H_2O: 1 THF	3,5	Bentheimer	0	4	100,0	2,54
22	17 Utsira: 1 THF	3,2	-	0	17	100,0	2,44
23	17 Utsira: 1 THF	3,2	Bentheimer	0	11	100,0	2,36
24	17 H_2O: 1 THF	3,2	-	0	5	20,0	2,0

[1)] Web camera was not in use at the time of this experiment, leading to a variation in hydrate formation time from 5-24 hours since the experiment lasted outside normal working hour. Not discussed further due to this large deviation in formation time.

*1,0g of SiO_2

4.2.1 Addition of solids with varying wetting properties

Solid particles are known to promote hydrate nucleation due to the increased nucleation sites available for crystal growth (Cheng et al., 2013, Zhao et al., 2011). To compare the effect of solids added the experiments with the same mole ratio, electrolyte and temperature were collected from table 12 and is presented in table 13 below. The first 6 combinations (Nr. 1, 3, 4, 11, 12 and 20) shown in table 13 are solutions with the same mole ratio of water to THF in addition to the same experimental temperature and electrolyte concentration, only difference is the type of particles added. The data from these results show that the addition of solids increased the percentage of successful hydrate formation from 66,7% in bulk solution to 100% with the addition of solids. The average hydrate formation time can be seen to increase with the addition of the particles except for the addition of Bentheimer particles, where the average hydrate formation time decreased compared to bulk solution.

The next 5 combinations (Nr. 2, 5, 6, 18 and 19) were all done with 17 H_2O: 1 THF mole ratio and 3,5 wt.% NaCl solution at either 0ºC or 2ºC. Experiments performed at 0ºC gave 100% hydrate success rate in bulk solution, whereas addition of CN-EC particles yielded no hydrate formation. At 2ºC the successful hydrate formation time increases from 20% in bulk solution to 100% by the addition of SiO_2^*, CN-nonEC and C18 particles and to 75% by the addition of SiO_2 particles. Addition of CN-EC yielded no hydrate formation, same as at 0ºC. The average hydrate formation time at 2ºC was observed to decrease with addition of particles, the opposite as what was observed for the experiments performed without electrolytes present (Nr. 1, 3, 4, 11, 12 and 20).

Experiments performed with Utsira formation water (Nr. 22 and 23) shown in table 13 no effect in success rate by the addition of particles. Both combinations gave 100% hydrate nucleation, only a small reduction in the average hydrate formation time can be seen for the experiments performed with the addition of the particles. This formation water was used “as is” to best represent natural conditions in the reservoir, meaning that natural occurring solid substances were visibly seen in solution.

Table 13. Extraction of data from table 16 showing the effect of adding different solids into solution with and without electrolytes.

Nr	Composition (H_2O/ Utsira: THF)	NaCl (wt.%)	Solids	Temperature (°C)	Nr. of experiments	Successful hydrate formation (%)	Corrected Average hydrate formation time (hr) ± 0,5
1	17 H_2O: 1 THF	0	-	2	6	66,7	2,25
3	17 H_2O: 1 THF	0	SiO_2	2	3	100	2,25
4	17 H_2O: 1 THF	0	SiO_2*	2	1	100	19
11	17 H_2O: 1 THF	0	CN-nonEC	2	1	100	3
			CN-EC	2	9	100	3,56
12	17 H_2O: 1 THF	0	C18	2	1	100	23
20	17 H_2O: 1 THF	0	Bentheimer	2	2	100	1,5
2	17 H_2O: 1 THF	3,5	-	0	5	100	7,92
				2	10	20	19,25
5	17 H_2O: 1 THF	3,5	SiO_2	2	7	75	14,3
6	17 H_2O: 1 THF	3,5	SiO_2*	2	1	100	5<hr<24 1)
18	17 H_2O: 1 THF	3,5	CN-EC	0	1	0	No hydrate formation
			CN-EC	2	6	0	No hydrate formation
			CN-nonEC	2	3	100	3,67
19	17 H_2O: 1 THF	3,5	C18	2	1	100	4,5
22	17 Utsira: 1 THF	3,2	-	0	17	100	2,44
23	17 Utsira: 1 THF	3,2	Bentheimer	0	11	100	2,36

1). Web camera was not in use at the time of this experiment, leading to a variation in hydrate formation time from 5-24 hours since the experiment lasted outside normal working hours.

4.2.2 Change in temperature

Temperature plays a significant role in hydrate formation, being one of the critical parameters together with pressure that affects hydrate nucleation. The driving forces of hydrate nucleation will increase as subcooling increases (i.e. temperature decrease), ref. figure 9 in section 2.1.4. The temperature for these experiments were either -5, 0 or 2°C. Figure 25 and 26 shows the success rate and average hydrate formation time by change in temperature for combination 1 and 2 (ref. table 12), respectively. Figure 25 shows THF solution without any electrolytes and figure 26 with THF and 3,5 wt.% NaCl solution, both with the ideal hydration number and no particles added. These figures show that when temperature is lowered, the success rate of hydrate formation and the hydrate formation time decreases substantially, corresponding well with literature where subcooling increases the driving forces. Figure 25, experiments without any electrolytes, shows that the success rate increases from 66,7% to 100% by lowering the temperature to 0 and -5°C. The average hydrate formation time decreases from 2,25 hours at 2°C to 0,75 hours at 0ºC and to 0,23hours at -5ºC. Figure 26, experiments with 3,5 wt.% NaCl solution, shows this same trend that when the temperature is lowered from 2ºC to 0ºC the success rate increases from 20% to 100% and the formation time decreases from 19 to 8 hours.

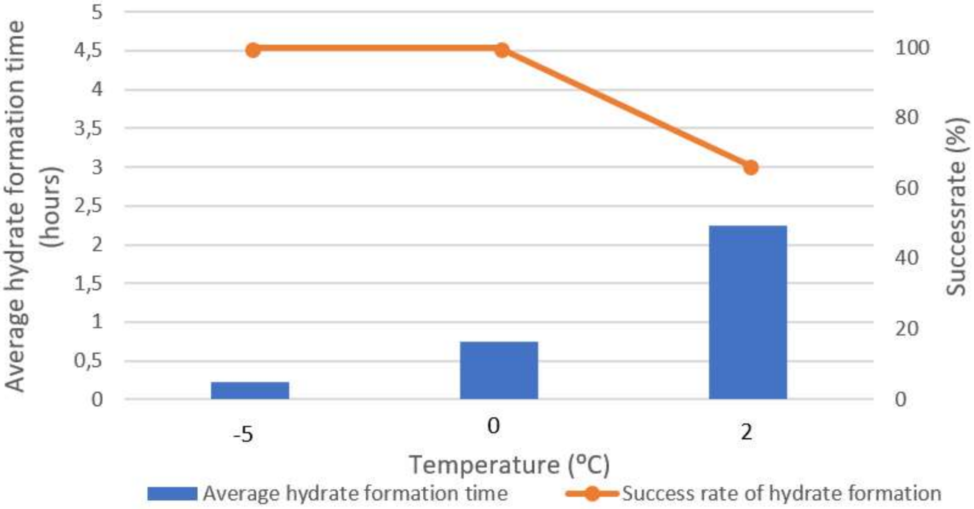

Figure 25. Successful hydrate formation time and success rate for experiments without electrolytes in bulk solutions at -5, 0 and 2ºC (Combination nr.1, table 12). Figure shows change in success rate and hydrate formation time by change in temperature. The significant decrease in success rate can be seen when temperature is increased to 2ºC in combination with increase in average hydrate formation time.

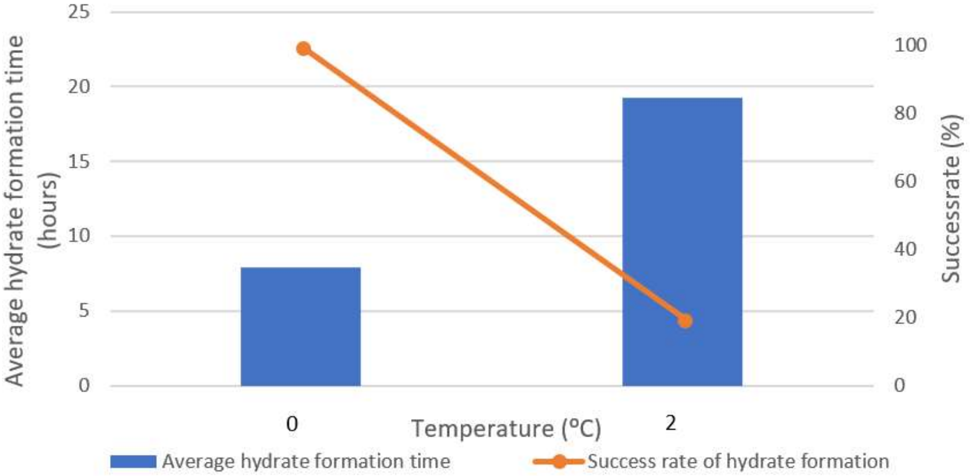

Figure 26. Successful hydrate formation time and success rate for THF experiments with 3,5 wt.% NaCl bulk solutions at 0 and 2ºC (Combination nr.2, table 12). Figure shows change in success rate and hydrate formation time by change in temperature. The significant decrease in success rate can be seen when the temperature increases from 0 to 2ºC in combination with increase in average hydrate formation time.

4.2.3 Change in electrolyte concentration

Electrolytes are a known chemical inhibitor that can either prevent or prolong the induction time of hydrate formation. This thesis has used Sodium Chloride (NaCl>99,%) at different concentrations in addition to Utsira formation water (3,2 wt.% electrolyte concentration, ref. table 5 for details of electrolyte constituents).

A summary of the THF experiments from table 12 performed in bulk solution with the same mole ratio and only change in Sodium Chloride concentration is shown in table 14 below. At 2ºC the increase in electrolyte concentration was observed to decrease the success rate of hydrate formation from 66,7% for experiments without electrolyte to 20% for solutions with 3,5wt.% NaCl and to no hydrate formation for experiments performed with 5,0wt% NaCl. The average hydrate formation time is seen to increase substantially when the electrolyte concentration increases, from 2,25 hours without electrolytes to 19,25 with 3,5wt% NaCl and to no hydrates at 5,0wt% NaCl.

Experiments performed at 0ºC from table 14 shows that the success rate of hydrate formation decrease from 100% without any electrolytes to 20% for 3,2wt% NaCl. Experiments performed with 3,5wt% NaCl were seen to have a success rate of 100%, which is an anomaly since eperiments with 3,2wt% NaCl did not yield any THF hydrates

Table 14. Extraction of data from table 12 which shows the experiments performed in bulk solutions. Table shows experiments with NaCl as electrolyte with the same mole ratio in bulk solution.

Nr	Composition (H_2O/Utsira: THF)	NaCl (wt.%)	Temperature (ºC)	Nr. of experiments	Successful hydrate formation (%)	Average hydrate formation time (hr) ± 0,5
1	17 H_2O: 1 THF	0	-5	4	100	0,23
			0	5	100	0,75
			2	6	66,7	2,25
24	17 H_2O: 1 THF	3,2	0	5	20	2
2	17 H_2O: 1 THF	3,5	0	5	100	7,92
			2	10	20	19,25
15	17 H_2O: 1 THF	5	2	2	0	No hydrate formation

Since electrolytes are a chemical inhibitor it is to be expected that an increase in electrolyte concentration will delay or even prevent THF hydrate formation. Most of the experiments have behaved according to this, but combination nr. 24 with 3,2 wt.% NaCl gave hydrate formation in only 20% of the experiments, whereas the 3,5wt% NaCl experiments gave 100% hydrate formation at 0ºC. The 3,2 wt.% NaCl experiments should have yielded a much higher hydrate formation success rate. Increase in electrolyte concentration was seen to decrease the success rate and increase the hydrate formation time in average.

4.2.4 Change in mole ratio of solution

The ideal hydration number for THF and water is approximately 17 moles H_2O to 1 mole THF, corresponding to approximately 20 wt.% THF. Figure 5 in section 2.1.2 shows that a 20 wt.% THF solution can form hydrates up until 4,5ºC. The temperature for these experiments were 2ºC, well below the melting point of THF hydrate at atmospheric conditions. To investigate the effect of changing the mole ratios there were experiments performed at 2ºC with 17 H_2O: 1 THF, 17 H_2O: 0,66 THF and17 H_2O: 0,33 THF ratios. Table 15 list the experiments performed at the same temperature with various mole ratios chosen.

It can be seen from table 15 that the 17 H_2O: 0,33 THF did not yield any THF hydrates with or without particles added. The experiments performed with 17 H2O: 0,66 THF did form hydrates but only with the addition of particles and not in bulk solution. The results from table 15 shows that THF hydrates formed most successfully with the ideal hydration number and decreases as the mole ratio decreases, corresponding well with literature.

Table 15. Effect of change in mole ratio of H_2O: THF with and without particles at 2ºC without any electrolytes. Table shows that hydrate success rate decreases with decreasing wt.% THF.

Nr of experiments	Mole ratio (H_2O: THF)	Wt. % THF	Solid surfaces	Successful hydrate formation (%)
2	17: 0,33	6,7	-	0
2	17: 0,33	6,7	SiO_2	0
2	17: 0,66	13,3	-	0
2	17: 0,66	13,3	SiO_2	50
1	17: 0,66	13,3	CN-nonEC	0
1	17: 0,66	13,3	C18	100
6	17: 1	20	-	66,7
4	17: 1	20	SiO_2	100
11	17: 1	20	CN-EC	100
1	17: 1	20	CN-nonEC	100
1	17: 1	20	C18	100

4.2.5 THF hydrate growth

The heterogenous nucleation of the THF hydrate for these experiments were suspected to occur in one of the three scenarios, or a combination:

1. The surface of the glass vial due to the centrifugal forces of the stirring rate
2. Liquid/air interface
3. The surface of the particles added

Homogenous nucleation is deemed unlikely due to one of the possible nucleation sites could be the glass of the vial which all experiments were performed in. The hydrate growth patterns observed for these experiments were observed visually and the THF hydrate formed needed to achieve a size visible for the eye to detect.

Each of the experiments performed were given an ID number to separate each parallel from each other and these ID numbers will only be displayed in this section. For those experiments which gave successful hydrate formation the morphology of the hydrate formed varied considerably. Some experiments only gave hydrate particles on the top of the solution along the wall of the sample glass (figure 27b and c) and some experiments gave more slush hydrates extending further down in the solution, as seen from figure 27a. The three samples shown in figure 27 consisted of the exact same constituents but a significant difference in hydrate growth pattern can be seen.

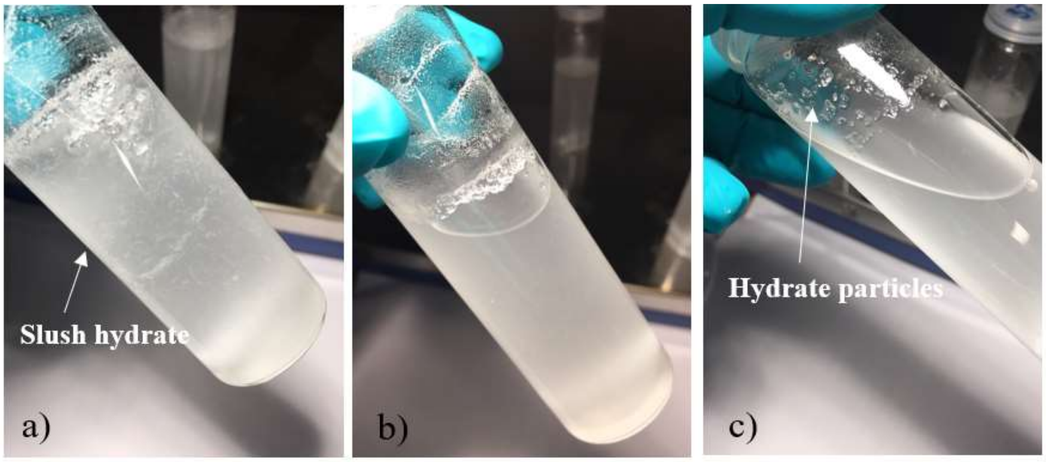

Figure 27. Figure shows three parallel experiments with 17 H_2O: 1 THF with intermediate water-wet CN-EC particles where a) is ID 36 after 2,5 hours, b) ID 37 after 1,5 hours and c) ID 40 after 1,5 hours. Experimental temperature of 2ºC. Slush THF hydrates can be seen in a) and solid particles in b) and c).

Figure 28 below shows experiments performed with 17 H_2O: 1 THF at 2ºC where a) shows hydrate growth 1 day after start for a bulk solution without any electrolytes present, b) and c) shows experiments performed in bulk with 3,5 wt.% NaCl solution after 1 day and 19 hours, respectively. Comparison of THF hydrate growth shows that what appeared as full conversion of liquid solution to hydrate occurred only for bulk solution without any electrolytes (figure 28a), whereas for the solutions with 3,5 wt. % NaCl the hydrate growth did not completely convert the entire liquid solution (figure 28ba and c). Full conversion of hydrates with electrolytes will not occur since electrolytes are not present in the hydrate structure, leading to accumulation of electrolytes outside the hydrate structure. This will in turn increase the local salt concentration and inhibit further hydrate formation. The results here are based on visual observations and liquid could be present without being able to visually see it.

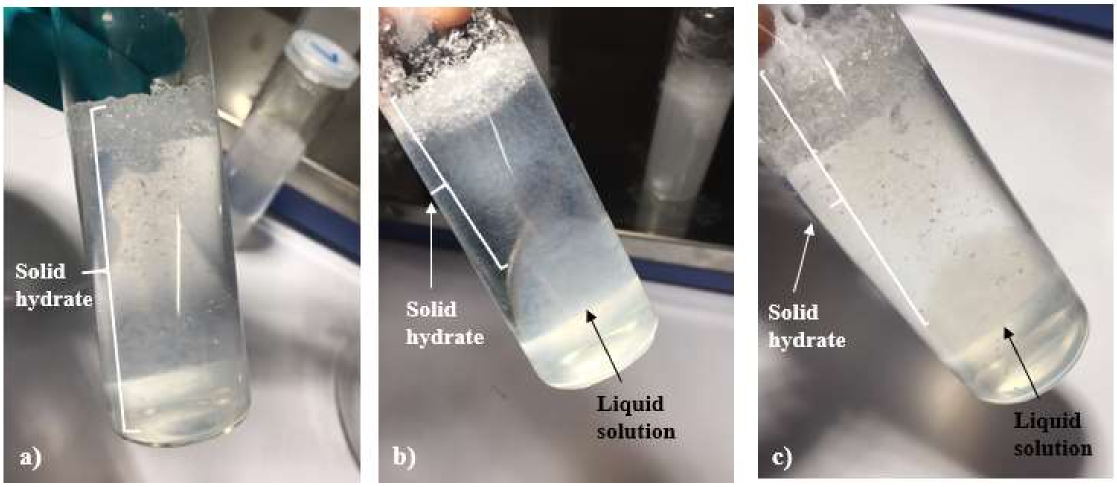

Figure 28. THF hydrate growth for three experiments with 17 H_2O: 1 THF solutions in bulk (i.e. without particles) performed at 2°C. Figure a) without any electrolytes after 1 day (ID 1), b) 3,5 wt.% NaCl solution (ID 1, hydrate growth after 1 day) and c) 3,5 wt.% NaCl solution (ID 31) after 19 hours.

Figure 29 below shows THF hydrate growth for solutions containing the ideal hydration number without electrolytes, experiment performed at 2°C. Figure 29a and b shows the solution with addition of intermediate water-wet CN-nonEC solid particles, after 1 and 4 days, respectively. Figure 29c and d shows solution with oil-wet C18 solid particles after 1 and 4 days, respectively. Comparison of these experiments shows a more solid hydrate growth with the addition of CN-nonEC particles, whereas the solution with C18 particles formed a solid hydrate layer at the top of the solution. Observations also display solutions consisting of both solid hydrate, slush hydrates and liquid solution. Solid hydrates were mainly found on the glass vial or surface of the solution whereas the slush hydrate was usually seen below the solid hydrate phase and above the liquid solution at the bottom.

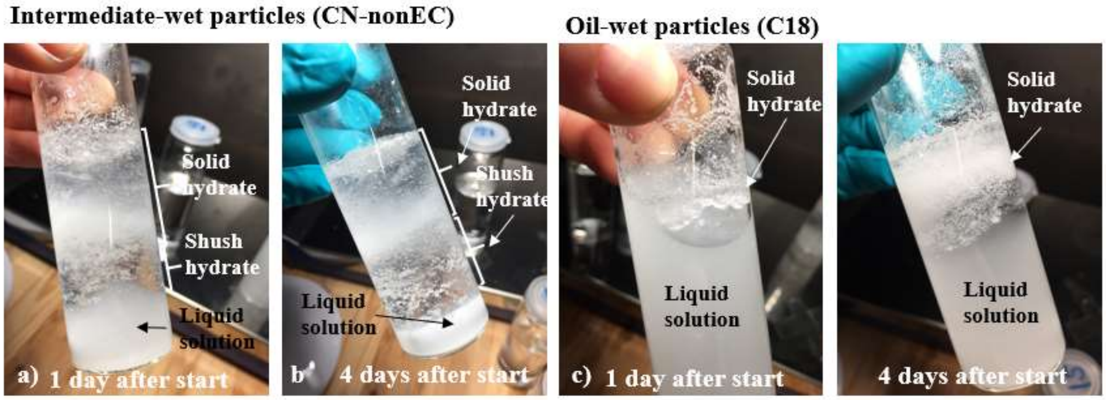

Figure 29. The THF hydrate formation for ID 19 and 20 with 17 H_2O: 1 THF with intermediate-and oil-wet particles where a) and b) shows ID 19 with intermediate water-wet CN-nonEC particles after 1 and 4 days and c) and d) shows ID 20 with oil-wet C18 particles after 1 and 4 days of growth. Experimental temperature of 2°C.

Figure 30 presents experiments with a solution of 17 H_2O: 0,66 THF performed at 2ºC, where figure 30a and b displays the addition of intermediate water-wet SiO_2 particles and figure 30c and d) displays the addition of oil-wet C18 particles. It can be seen that both solid particles yielded a similar hydrate structure after 4 days (b and d), with a solution consisting of solid particles at the surface and liquid solutions at the bottom with an area in the middle of slush hydrate suspension.

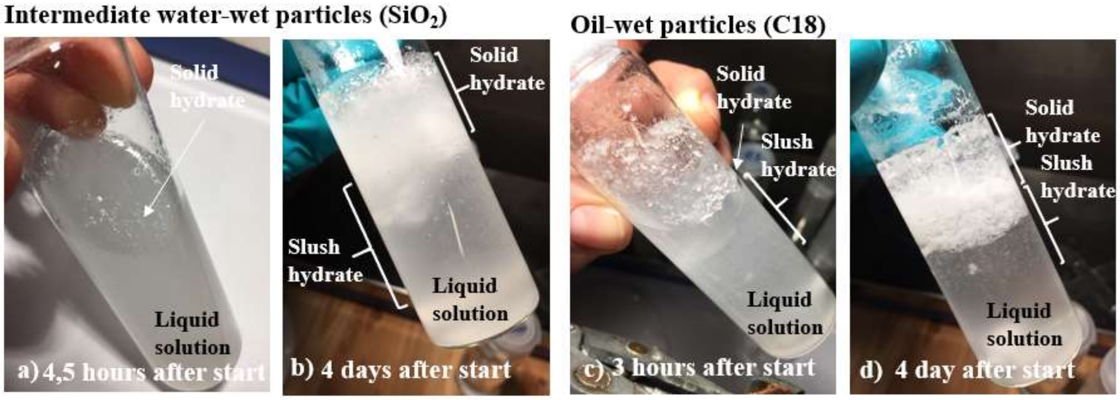

Figure 30. The THF hydrate formation for ID 17 and 22 with 17 H_2O: 0,66 THF with intermediate-and oil-wet particles where a) and b) shows ID 17 after 4,5 hours and 4 days and c) and d) shows ID 22 after 3 hours and 4 days of growth. Experimental temperature of 2ºC.

Figure 31 shows 7 parallel experiments with 17 H_2O: 1 THF with CN-EC particles (intermediate water-wet) after 24 hours at 2ºC. The crystal growth for each sample varies and none of the experiment has the same crystal growth pattern. It can also be seen that some of the crystals are growing out from the top of the surface (ID 37-40) and when viewing the samples from left to right the total crystal growth decreases in average from ID 36-42.

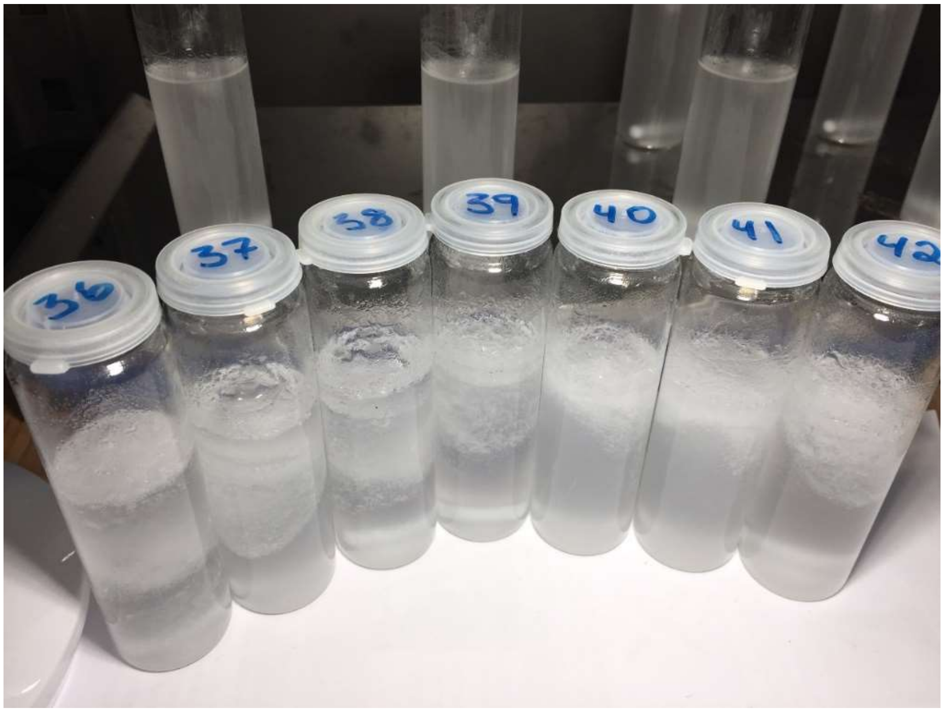

Figure 31. Seven parallel experiments performed with 17 H_2O: 1 THF with CN-EC particles (ID 36-42) after 24 hours. The figure shows that the crystal growth varies for each sample and none of the experiments gave equal crystal growth. Experimental temperature of 2ºC.

An interesting observation was that the most solid THF hydrates formed were for the solution containing the ideal hydration number, but without the addition of particles. It was observed that the solutions with the ideal hydration number with particles formed hydrates faster but not as solid as the same solution without the addition of particles.

Further investigation of the macroscopic crystal structure of THF hydrate in both bulk solution and with the addition of particles by use of an MRI instrument are presented in section 4.4.

4.3 Discussion – the screening of THF hydrate in different chemical environments

Equation 2 presented in section 2.1.4 shows the correlation between homogenous and heterogenous nucleation, differentiated by ϕ which is influenced by the particles/solid surfaces contact angles toward the liquid. The addition of particles will therefore increase the probability of hydrate nucleation due to the total increase in the total Gibbs free energy. The experiments performed in this section are meant to give an indication to which parameters affect hydrate nucleation the most. The following subsection discusses the effect of adding solid particles with varying wetting properties, change in temperature, mole ratio, electrolyte concentration and the growth pattern observed.

4.3.1 The effect of addition of particles with various wetting properties

The various particles used for these experiments had the following wetting properties:

- Intermediate water-wet: CN-EC/nonEC
- Untreated water-wet: Bentheimer, SiO_2
- Oil-wet: C18

The general observation for the experiments performed with the ideal hydration number were an substantially increase in the hydrate success rate when particles were added, for both solutions consisting of no electrolytes and 3,5wt% NaCl solutions, table 12 and 13. Figure 32 below shows the change in average hydrate formation time and success rate when particles were added to a solution of 17 H_2O: 1 THF without any electrolytes at 2ºC (Combination nr. 1, 3, 4, 11, 12 and 20 from table 13). From this figure the success rate increases from 66,7% in bulk solution to 100% for all experiments with particles added, independent of the various wetting properties. The average hydrate formation time can be seen to be the highest for C18 and SiO_2^* and lowest for experiments with Bentheimer. Since THF and water are polar compounds they have an affinity for hydrophilic surfaces, corresponding to solid surfaces that are water-wet. These results correspond well where the water-wet solid surfaces (e.g. Bentheimer, CN-EN/nonEC and SiO_2) had the lowest formation time and the oil-wet C18 the highest. However, the water-wet SiO_2^* did also show a high hydrate formation time, deviating from the other results. But, since the nucleation of hydrates are considered a stochastic process (i.e. random) the results presented here are expected to vary and more precise methods should be used for further investigation of the wettability of solid particles on hydrate formation

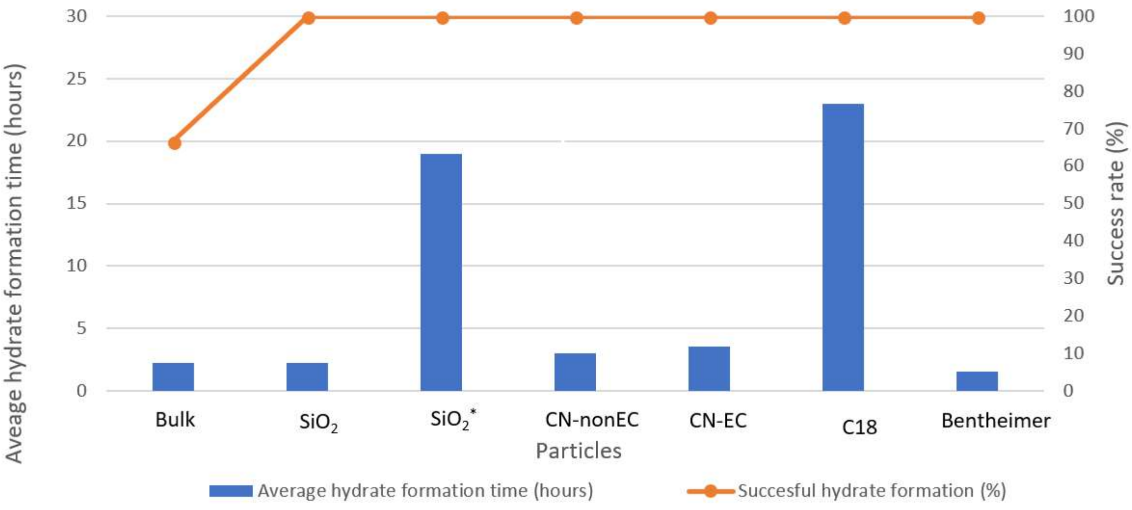

Figure 32. The average hydrate formation time and success rate for the experiments with 17 H_2O: 1 THF and 0,0 wt.% NaCl at 2ºC with the addition of various particles. Figure shows that success rate increases by the addition of particles from 66,7 % in bulk solution (comb. nr. 1) to 100% with addition of particles. Bentheimer lowers the formation time while the other particles increase the formation time compared to bulk solution. SiO_2, SiO_2^*, CN-nonEC, CN-EC, C18 and Bentheimer represent combination nr. 3, 11, 11, 12 and 20, respectively.

A more significant effect can be seen when comparting the results from figure 32 with the results from figure 33. Figure 33 displays the results with 17 H_2O: 1 THF with 3,5 wt.% NaCl at 2ºC with the addition of particles. This figure shows that by addition of particles the success rate increases from 20% in bulk solution to 75% for SiO_2 and to 100% for SiO_2^*, CN-nonEC and C18. Addition of CN-nonEC resulted in no hydrate formation, which is an anomaly since CN-EC and CN-nonEC should in principle yield hydrate formation equally. The hydrate formation time is observed to decrease with the addition of SiO_2, CN-nonEC and C18 particles, same as the experiments presented in figure 32.

The addition of water-wet CN-EC particles that did not yield any hydrate formation is an anomaly since both endcapped and non-endcapped CN particles should behave in the same manner. There were numerous remediation methods tried to investigate why this change occurred. The most likely reason was thought to either be a difference in the solid particles or temperature related, but without being able to find a most likely reason, further described in appendix A. An article found on molecular dynamic simulation of CO_2 hydrate formation reports that hydrate nucleation form more easily on hydrophobic surfaces and quote:

"It is surprising to find that the induction time for the crystal nucleation is reduces when less -OH groups exist on the silica surface. In other words, CO_2 hydrates can form more easily from less hydrophilic solid surfaces" (Bai et al., 2015)

This article reports the opposite of the results obtained here, since the results presented her formed hydrates with the solid particles containing the OH groups present, but it might suggest a reason for why there is a difference in hydrate formation between CN-EC and CN-nonEC. The general perception by the author is that presence of OH groups for CN-nonEC makes the molecule more water-wet and susceptible for hydrate formation, since THF is water soluble, which should yield hydrate formation more easily on hydrophilic surfaces such as CN-nonEC, Bentheimer and SiO_2. Furthermore, the solid chromatography CN phases used in this thesis are normally not used for forming hydrates and the results from this thesis might suggest that using such solid materials are not ideal for forming hydrate since the surface properties might not be identical depending on supplier.

Addition of twice the amount of solid particles was seen to increase the formation time by comparison of SiO_2 with SiO_2* in figure 32. The results show that addition of twice the amount of particles does not promote hydrate nucleation more than a smaller amount, suggesting that the presence of a small number of particles are enough for promoting hydrate nucleation and further addition of particles does not promote hydrate growth additionally.

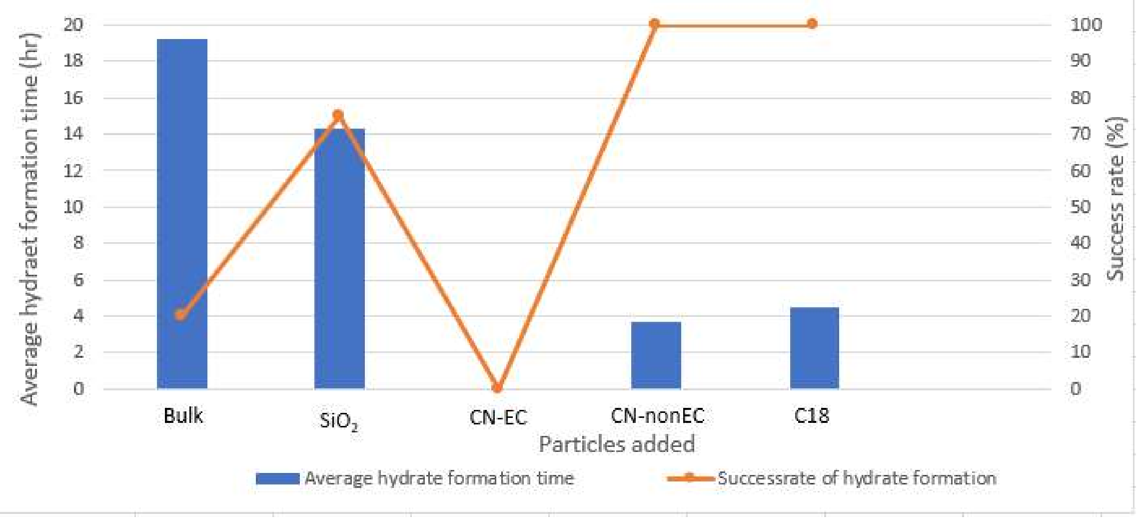

Figure 33. The average hydrate formation time and success rate for the experiments with 17 H_2O: 1 THF and 3,5 wt.% NaCl at 2°C. Figure shows that by addition of particles the success rate increased from 20% in bulk (comb.nr 2) to 75% for SiO_2 (comb.nr 5) to 100% for CN-nonEC (comb. nr. 18) and C18 (comb.nr. 19). The hydrate formation time can be seen to decrease by the addition of solid particles for those experiments with successful hydrate formation.

For the experiments with Utsira formation water, the addition of Bentheimer solid particles did not display a significant decrease in formation time compared to bulk solution, combination nr. 22 and 23 from table 12. Both combinations also had a success rate of 100%. Observation of the formation water displayed a solution with particles that most likely promoted hydrate nucleation. These results further verify the idea of that only small number of particles are necessary for promoting hydrate growth and that further addition of particles does not further decrease the formation time.

4.3.2 The effect of change in temperature

As the subcooling increases (i.e. temperature decrease) the hydrate formation time decreases and the success rate increases, for both experiments without electrolytes (figure 25) and with 3,5wt.% NaCl (figure 26). The most significant effect of subcooling is seen for the experiments performed with 3,5 wt.% NaCl solution, for these experiments the success rate decreased from 100% at 0ºC to 20% at 2ºC and the hydrate formation time increased from 7,92 to 19,25 hours. These results correspond well with literature where subcooling is one of the critical parameters for hydrate nucleation together with pressure control. Studies performed by Corak et al. (2011) have shown that for electrolyte solutions the increase in subcooling promote cyclopentane hydrate growth considerably. The increase in salinity leads to higher driving forces necessary for hydrate nucleation compared with no electrolyte present. The experiments performed without electrolytes are therefore further inside the hydrate stability zone than the experiments with electrolytes, and hence, addition of electrolytes will require higher driving forces than the experiments without. The experiments shown in figure 25 and 26 suggest that the system is more sensitive to change in temperature when electrolytes are present (figure 26).

The bulk experiments performed without any electrolytes was well within the hydrate formation zone at 2ºC, ref. figure 34 (melting point of THF hydrate), and any further reduction in temperature will only place the system further inside the HSZ and increase the subcooling effect. From figure 25 it can be seen that when lowering the temperature to 0 ºC the success rate increases to 100%.

4.3.3 The effect of change in electrolyte concentration

The results from section 4.2.3 and table 14 shows that an increase in electrolyte concentration leads to a decrease in the success rate of hydrate formation and an increase in average hydrate formation time. The comparison of combination 1 and 2 shows that the average hydrate formation times increases from 2,25 hours without electrolytes present to 19,25 hours with 3,5wt.% NaCl solutions at 2ºC. At 0ºC the formation time increases from 0,75 hours without electrolytes to 7,92 hours with 3,5wt.% NaCl solutions. These results display that the addition of electrolyte prolongs the formation time considerably but does not necessarily prevents it.

Figure 34 below shows the effect of changing the electrolyte concentration at 0ºC and 2ºC, where the blue bars are experiments performed at 2ºC and red bars are at 0ºC. The figure show that without any electrolytes present the average hydrate formation time at both temperatures are approximately the same whereas with 3,5 wt.% NaCl solution there is a more substantial difference in hydrate formation time at the two temperature. These results show that by increasing the electrolyte concentration the formation time increases substantially and is strongly dependent on experimental temperature, where a more sensitive system is seen when electrolytes are present. This is as expected since addition of electrolytes move the equilibrium line further away from the HSZ.

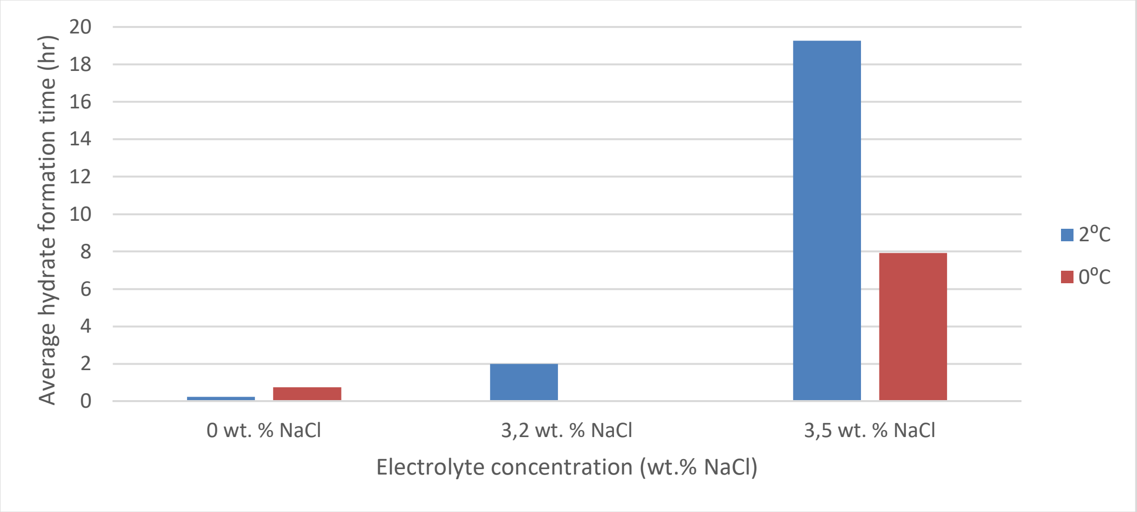

Figure 34. Change in average hydrate formation time in bulk solutions with varying electrolyte concentrations at 0°C and 2°C. Solutions with 3,2 wt.% NaCl was only performed at 2°C. The figure shows that when electrolyte concentration decreases, the average hydrate formation time decreases. Furthermore, the most significant effect of the decrease in formation time can be seen for the experiments performed at 2°C, where the formation time decreases from 19 hours with 3,5 wt.% NaCl solution to 0,23 hours with no electrolyte present.

From figure 34 and table 14 the experiments performed with 3,2 wt.% NaCl deviated from other results when comparing the success rate of hydrate formation. The experiments with 3,2 wt.% NaCl resulted in 20% success rate at 0°C whereas 3,5 wt.% NaCl yielded 100% success rate. The average hydrate formation time was however seen to correspond well with the other results, as seen in figure 34, where the formation time at 3,2 wt.% NaCl lies between 3,5 wt.% NaCl and experiments without electrolytes. The most probable reason for the low success rate of hydrate formation were thought to be temperature dependent due to the month these experiments were performed at. These experiments were conducted in May month 2018 where the temperature in the city was considerably higher than the temperatures in the previous months. The refrigerator used for these experiments seems to be affected by the increased air temperature.

4.3.4 The effect of change in mole ratio

Figure 35 below is modified from figure 5 in section 2.1.2 which shows the melting point temperatures of THF hydrate by the change in wt.% of THF. A 20 wt.% THF solution corresponds to approximately 17 moles of H_2O and 1 mole THF. A 13,3 mass. % THF corresponds to 17 moles H_2O and 0,66 moles of THF and a 6,7 wt.% THF corresponds to 17 moles of H_2O and 0,33 moles of THF. This thesis used these mole ratios performed at 2°C. According to figure 35 the 6,7 wt.% THF should not give any hydrate formation since the melting point is slightly below 1ºC whereas the 13,3 wt.% THF should give THF hydrate formation since the melting point is approximately 4ºC.

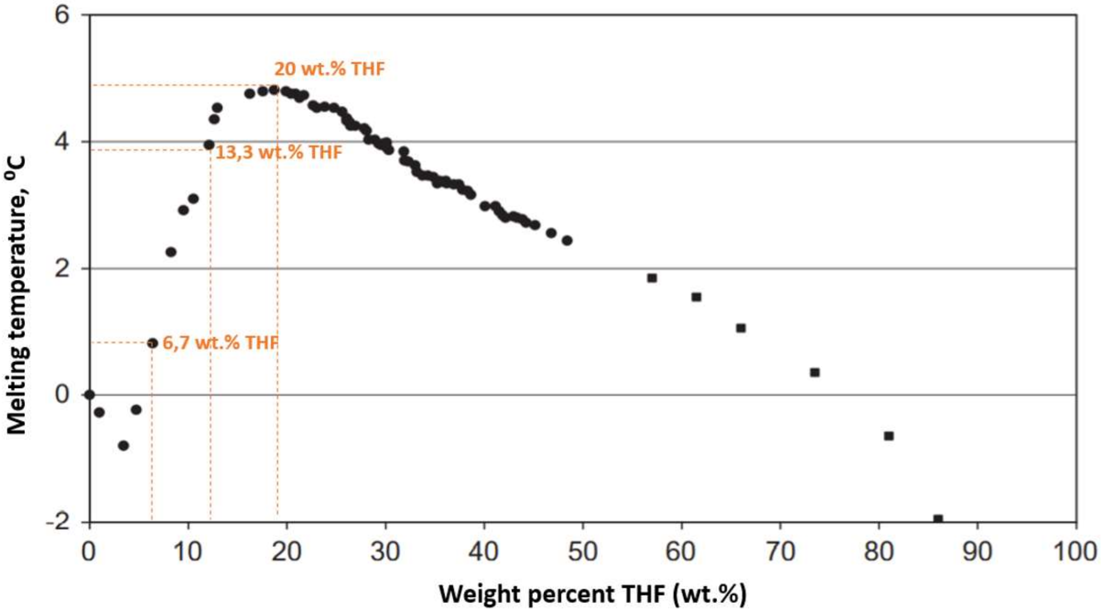

Figure 35. The change in melting point curve of THF hydrate with ultrapure water by the change in wt.% THF. Figure shows in orange the various mole ratios used in this thesis.

The results from table 15 in section 4.2.4 shows that THF hydrates did not form with 17 H_2O: 0,33 THF in bulk or with the addition of SiO_2 particles at 2ºC. By increasing the mole ratio to 17 H_2O: 0,66 THF there were successful hydrate formation for the solution containing SiO_2 and C18 solid particles. Bulk solutions with 17 H_2O: 0,66 THF and with the addition of CN did not yield any hydrate formation. Further increase in mole ratio to 17 H_2O: 1THF gave successful hydrate formation in both bulk and with the addition of particles. These results show that by increasing the weight percentage of THF toward the ideal hydration number, the hydrate formation success rate increases accordingly. These results correspond well with literature where the ideal hydration number (17 H_2O: 1 THF) should yield the most successful THF hydrate formation. When the hydration number is reduced there will be an excess of water, which means that complete solid hydrates throughout the solution will not form since there are not enough THF molecules to be encapsulated by the water molecules.

4.3.5 THF hydrate growth pattern

The solution containing the ideal hydration number without electrolytes added (figure 28a) were seen to form what appeared as more solid hydrates than solutions consisting of electrolytes, figure 28b/c. Since electrolytes are not part of the hydrate structure the formation of THF hydrate in a solution consisting of electrolytes will lead to local increased concentration of salt which in turn will prevent further hydrate growth. This is best illustrated in figure 28 where 28a shows without electrolytes and 28b and c with electrolytes, here it can be seen that solution with electrolytes formed hydrates only in part of the solution whereas the solution without electrolytes formed what appeared as solid hydrate.

Experiments performed with solid particles added did not display any significant change in hydrate growth depended on the various particles added. However, by comparison of hydrate growth in bulk solution with the ideal hydration number (figure 28a) with solutions with CN and C18 particles (figure 29 and 31) it can be seen that the bulk solution formed what appeared as the most solid hydrate.

The method of visually observing the THF hydrate growth was not sufficient to detect any significant differences of the various particles added and corresponding hydrate growth pattern. Some trends such as more hydrate growth on bulk solution compared to solutions of electrolytes and/or solid particles have been made, but a better method should be used for further investigation. Investigation of the macroscopic crystal growth of THF hydrate in bulk solution and with the addition of particles have been performed by use of MRI instrument, results presented in the next section (section 4.4).

4.4 Results- MRI technique for visualization of the macroscopic crystal structures of THF hydrate

The results from the investigation of the macroscopic crystal structure and morphology of THF hydrate in the MRI instrument is presented in this section, where solid particles with varying wetting properties have been added. The solid particles added were situated at the bottom of the solution. For better reproducibility, three parallels solutions were prepared for most of the series.

Each of the series were scanned by the RAREst protocol three times, leading to a total of 1,5 hours in the MRI instrument. The three RAREst protocols performed for each series represent a gradual melting of the formed THF hydrate. The image series presented in the following subsection shows the axial slice distribution with approximately 17 slices representing one sample, details shown in figure 21. Each of the samples presented in this section appeared by the visual inspection as solid hydrate, no visible liquid solution could be seen before starting the MRI analysis.

In total there was six series performed:

- 17 H_2O: 1 THF + Illite
- 17 H_2O: 1 THF + Bentheimer
- 17 H_2O: 1 THF + Water-wet SiO_2
- 17 H_2O: 1 THF + Oil-wet SiO_2
- Deionized water in bulk and deionized water + Bentheimer
- 17 H_2O: 1 THF

The following sub-section presents the results from each of these six series.

4.4.1 17 H_2O: 1 THF + Illite particles

The RAREst scans of three parallel solutions of 17 H_2O: 1 THF with addition of Illite solid particles is presented in this section. The temperature at hydrate formation was -2ºC before the samples were placed in the MRI instrument. The three solutions were scanned simultaneously three times with the RAREst protocol, approximately 30 min for each protocol. Each slice shown in the figures represents an axial position within the sample, ref. figure 21 for slice distribution. Solid hydrate is shown by the black areas due to solid phases not yielding any signal intensity and liquid solution is shown by the bright areas.

Figure 36 shows the RAREst protocols performed for parallel 1, where liquid solution can be seen between the formed hydrate structures and some accumulation of liquid solution approximately in the middle of the sample. This same trend can be seen for parallel two, figure 37, and parallel 3, figure 38.

The morphology of the THF hydrate structure from the figures for each parallel is consistently solid, with only small fractures/areas containing some liquid solution (bright areas) visible in the middle of each sample and between the macroscopic crystal structure. The melting of the hydrate structure is seen to occur on the outer edges of the three parallel samples and moving inwards. These figures show that the macroscopic crystal structures of THF hydrates can form channels that upon melting can contain more liquid.

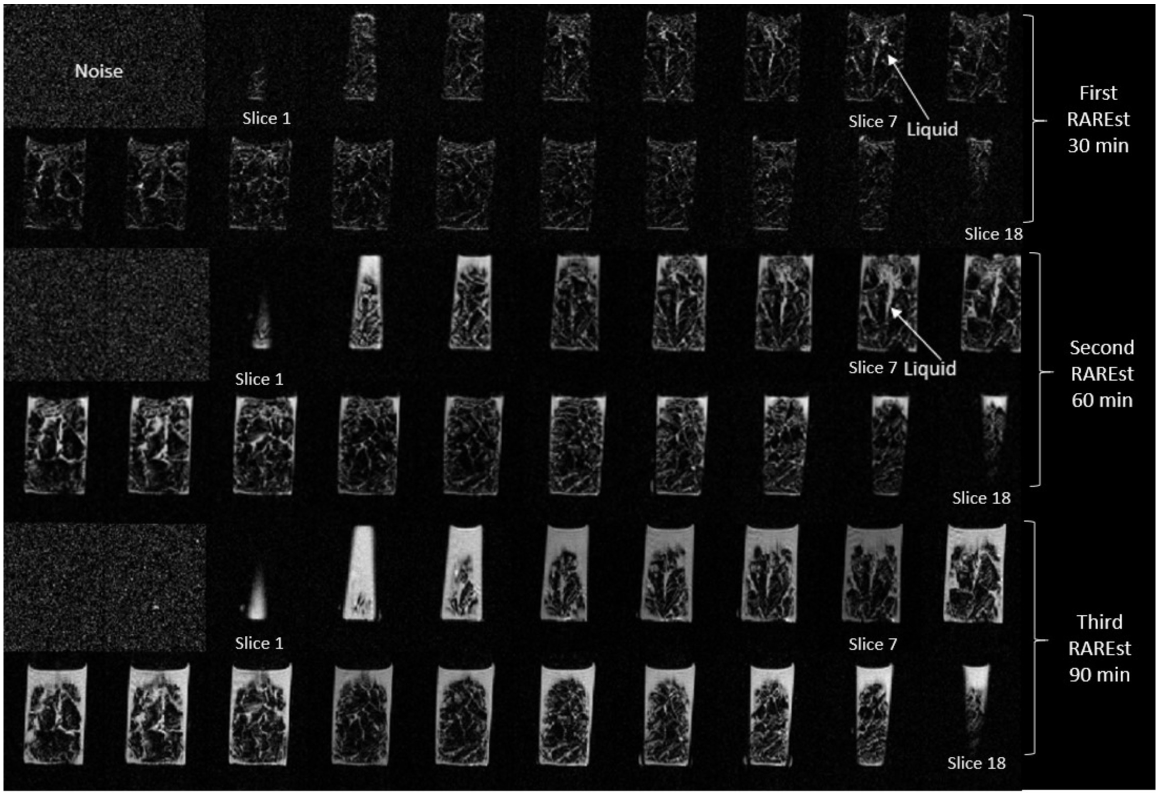

Figure 36. The three RAREst protocols performed for parallel one, with a solution consisting of 17 H_2O: 1 THF with the addition of Illite solid particles. Figure shows the macroscopic crystal structure of THF hydrate after 30, 60 and 90 minutes. The liquids phase can be seen between solid hydrate formed in solution and some liquid accumulation approximately in the middle of the sample. A gradual melting can be seen from the outer edges and inwards from 30 to 90 min. Each pixel picture obtained represents an axial slice in the sample.

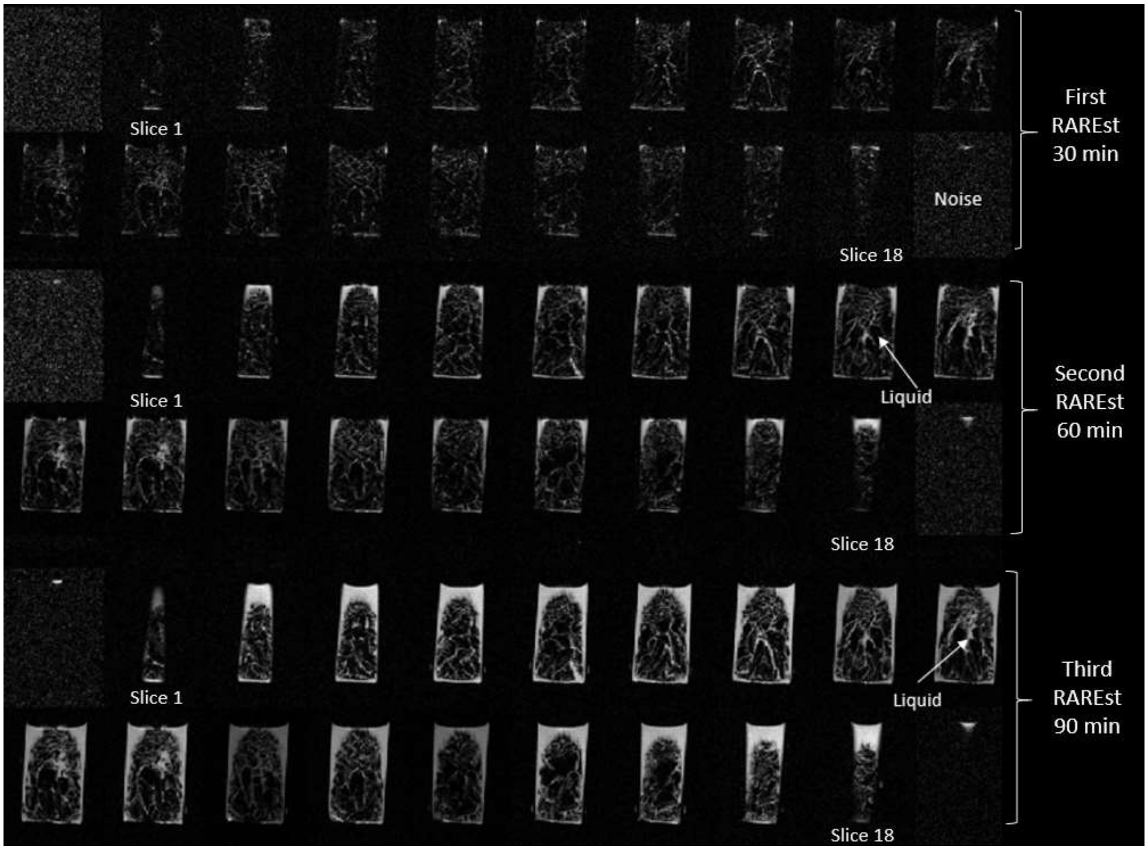

Figure 37. The three RAREst protocols performed for parallel two, with a solution consisting of 17 H_2O: 1 THF with the addition of Illite solid particles. Figure shows the macroscopic crystal structure of THF hydrate after 30, 60 and 90 minutes. The liquid phase can be seen between solid hydrate formed in solution and some liquid accumulation approximately in the middle of the sample. A gradual melting can be seen from the outer edges and inwards from 30 to 90 min. Each pixel picture obtained represents an axial slice in the sample.

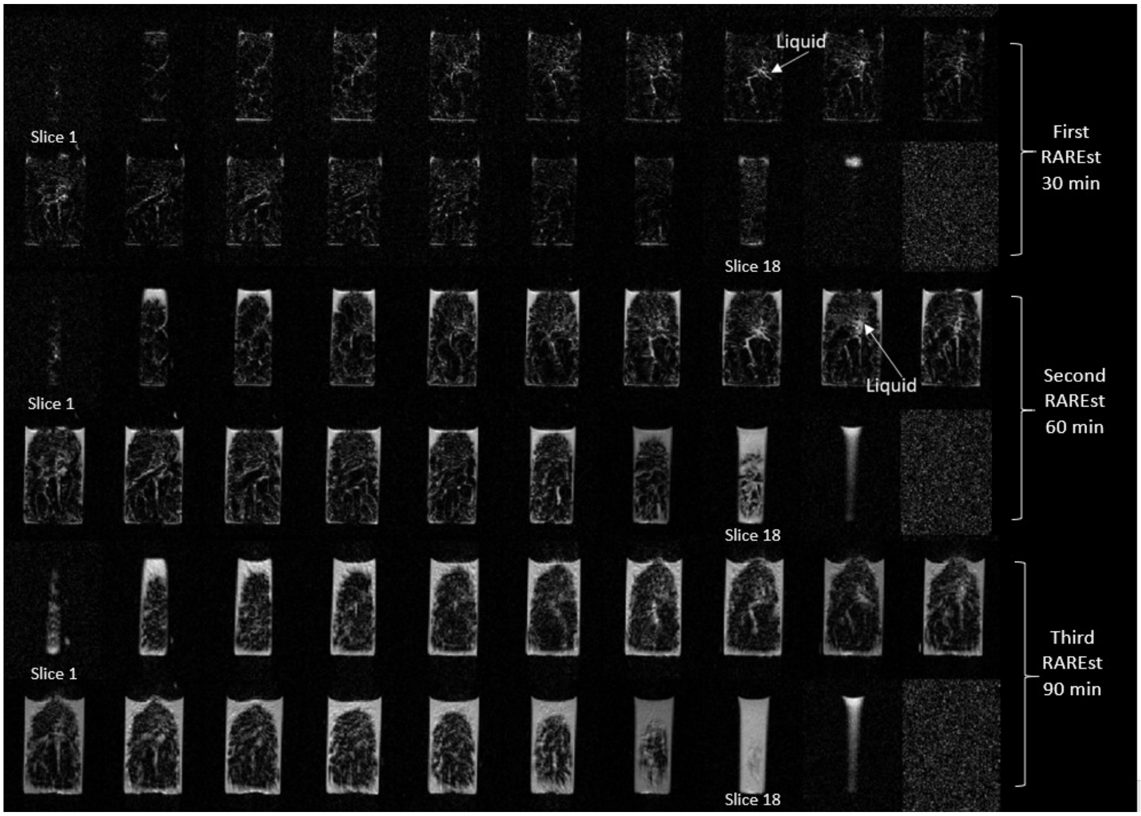

Figure 38. The three RAREst protocols performed for parallel three, with a solution consisting of 17 H_2O: 1 THF with the addition of Illite solid particles. Figure shows the macroscopic crystal structure of THF hydrate after 30, 60 and 90 minutes. The liquid phase can be seen between solid hydrate formed in solution and some liquid accumulation approximately in the middle of the sample. A gradual melting can be seen from the outer edges and inwards from 30 to 90 min. Each pixel picture obtained represents an axial slice in the sample.

4.4.2 17 H_2O: 1 THF + Bentheimer particles

The RAREst scans of three parallel solutions of 17 H_2O: 1 THF with addition of Bentheimer solid particles is presented in this section. The temperature at hydrate formation was -10ºC before the samples were placed in the MRI instrument. The three solutions were scanned simultaneously three times with the RAREst protocol, approximately 30 min for each protocol. Each slice shown in the figures represents an axial position within the sample, ref. figure 21 for slice distribution. Solid hydrate is shown by the black areas due to solid phases not yielding any signal intensity and liquid phase is shown by the bright areas.

Figure 39 shows the RAREst protocols performed for parallel one, where small amount of liquid can be seen between the formed hydrate structures and some liquid accumulation in slice 9 after 60 minutes (second RAREst). The morphology of the second parallel shown in figure 40 displays a more homogenous solid hydrate than the first parallel, where no significant accumulation of liquids could be seen. The third parallel on the other hand, shown in figure 41, have a more similar hydrate structure as parallel one than two. This third parallel have significant accumulation of liquid phase inside the structure, slice 9 and 10 after 60 and 90 minutes (second and third RAREst).

The morphology from the figures show that the formed hydrate for each parallel is consistently solid, with only small fractures/areas containing some liquids (bright areas) visible in the middle of some of the samples and between the macroscopic crystal structure. The melting of the THF hydrate is seen to occur on the outer edges of the three parallel samples and moving inwards. The third parallel (figure 41) also show that additional melting from 60 to 90 minutes results in further accumulation inside the structure, slice 9 and 10, suggesting that formed channels inside the hydrate structure can accumulate more liquid phase upon melting.

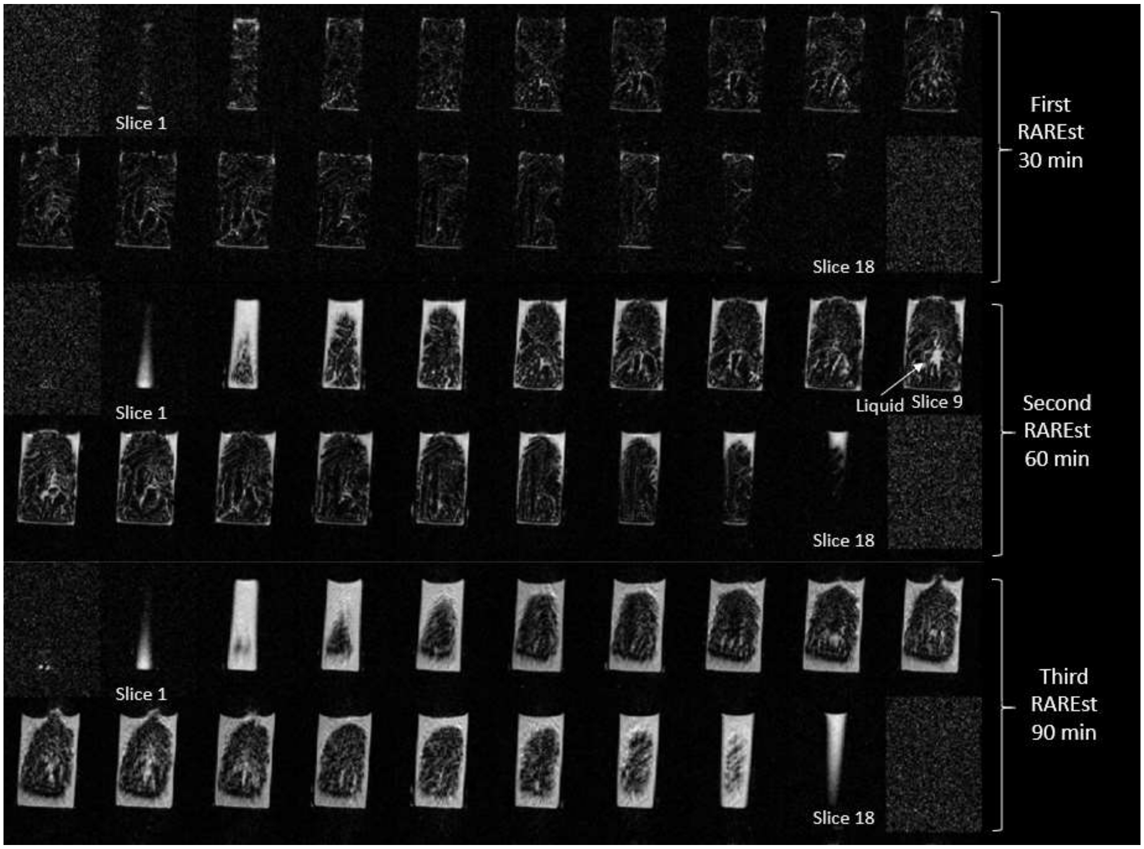

Figure 39. The three RAREst protocols performed for parallel one, with a solution consisting of 17 H_2O: 1 THF with the addition of Bentheimer solid particles. Figure shows the macroscopic crystal structure of THF hydrate after 30, 60 and 90 minutes. The liquid phase can be seen between solid hydrate formed in solution and some liquid accumulation in the middle of the sample (slice 9, second RAREst at 60min). A gradual melting can be seen from the outer edges and inwards from 30 to 90 min. Each pixel picture obtained represents an axial slice in the sample.

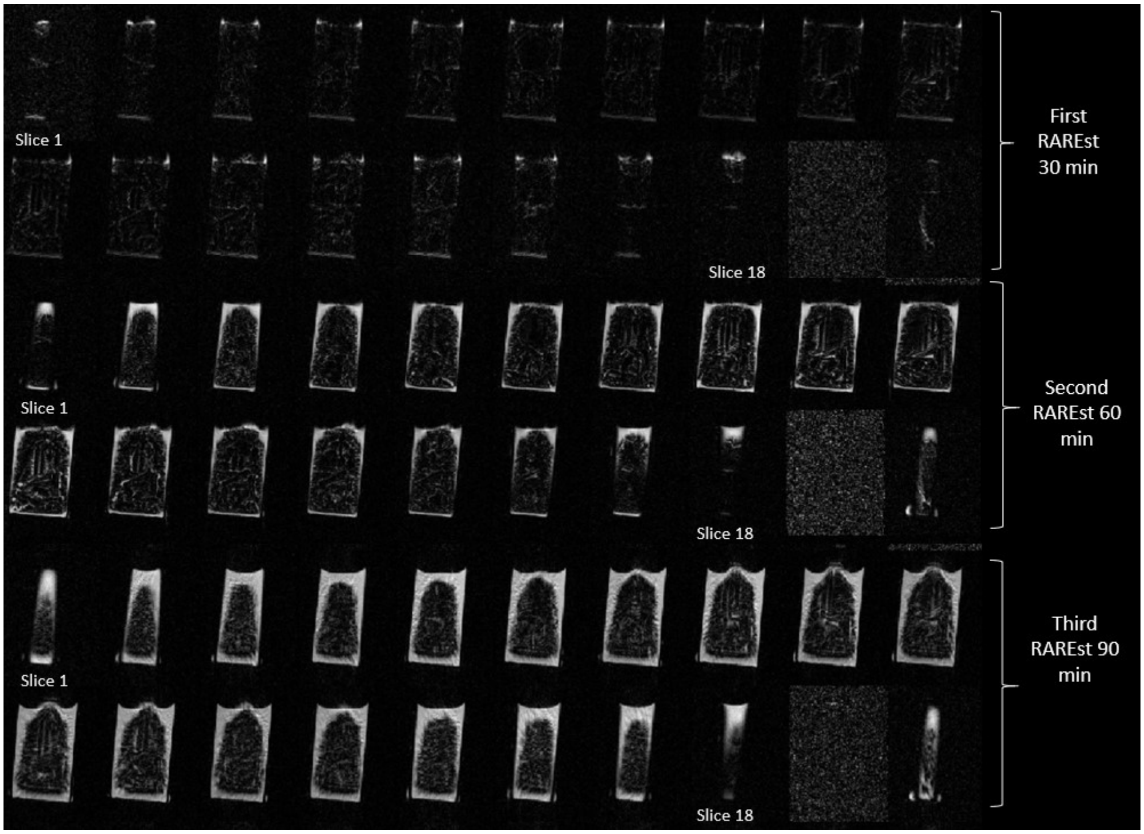

Figure 40. The three RAREst protocols performed for parallel two, with a solution consisting of 17 H_2O: 1 THF with the addition of Bentheimer solid particles. Figure shows the macroscopic crystal structure of THF hydrate after 30, 60 and 90 minutes. No significant liquid phase was seen inside the structure, only small accumulation between the hydrate structures formed. A gradual melting can be seen from the outer edges and inwards from 30 to 90 min. Each pixel picture obtained represents an axial slice in the sample.

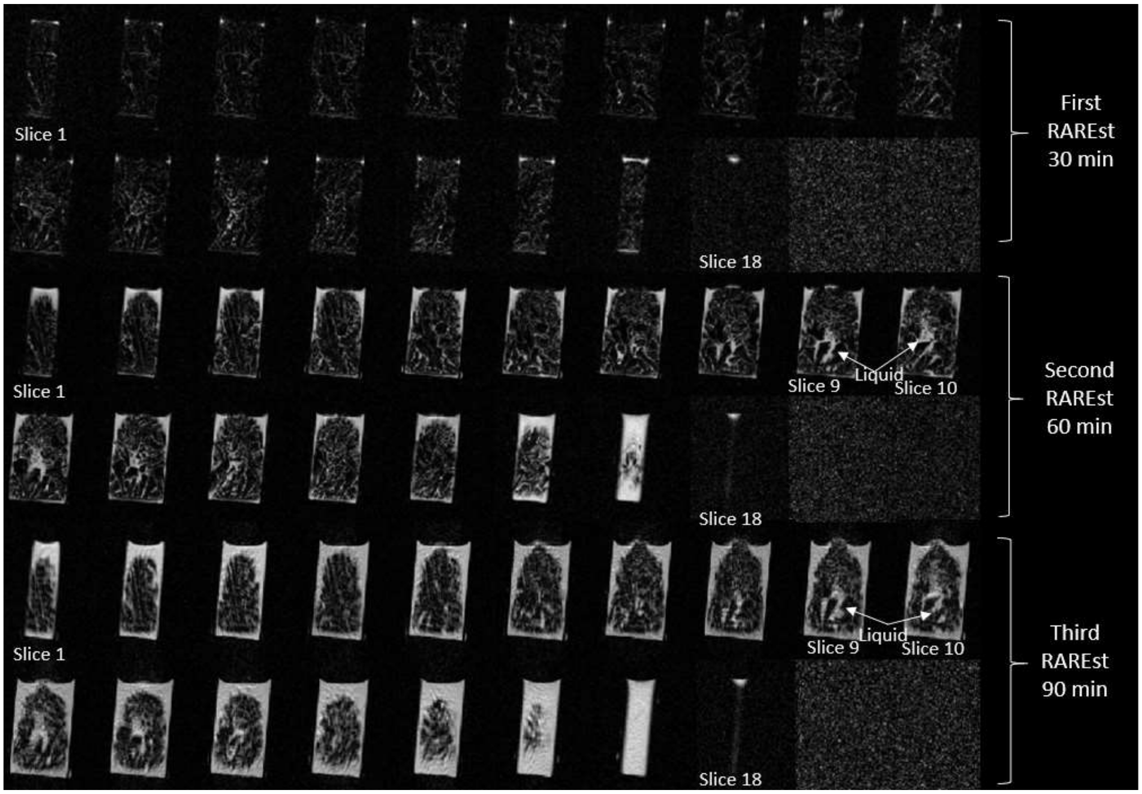

Figure 41. The three RAREst protocols performed for parallel three, with a solution consisting of 17 H_2O: 1 THF with the addition of Bentheimer solid particles. Figure shows the macroscopic crystal structure of THF hydrate after 30, 60 and 90 minutes. The liquid phase can be seen between solid hydrate formed in solution and some liquid accumulation in the middle of the sample (slice 9 and 10, second and third RAREst). A gradual melting can be seen from the outer edges and inwards from 30 to 90 min. Each pixel picture obtained represents an axial slice in the sample.

4.4.3 17 H_2O: 1 THF + Water-wet SiO_2 particles

The RAREst scans of two parallel solutions of 17 H_2O: 1 THF with addition of water-wet SiO_2 solid particles is presented in this section. The temperature at hydrate formation was -10ºC before the samples were placed in the MRI instrument. The two solutions were scanned simultaneously three times with the RAREst protocol, approximately 30 min for each protocol. Each slice shown in the figures represents an axial position within the sample, ref. figure 21 for slice distribution. Solid hydrate is shown by the black areas due to solid phases not yielding any signal intensity and liquid phase is shown by the bright areas.

Figure 42 shows the three RAREst protocols performed for parallel one. Solid hydrate is seen throughout the sample after 30 minutes, with only fractional accumulation of liquids between formed hydrate structures. For the second RAREst some liquid accumulation within the hydrate structure can be seen in slice 9.

The morphology of the second parallel shown in figure 43 show solid hydrate throughout the sample with only fractional accumulation of liquids between the formed hydrate structure. The two parallels show that the formed hydrate structure for each parallel is consistently solid. The melting of the hydrate is seen to occur on the outer edges of the three parallel samples and moving inwards.

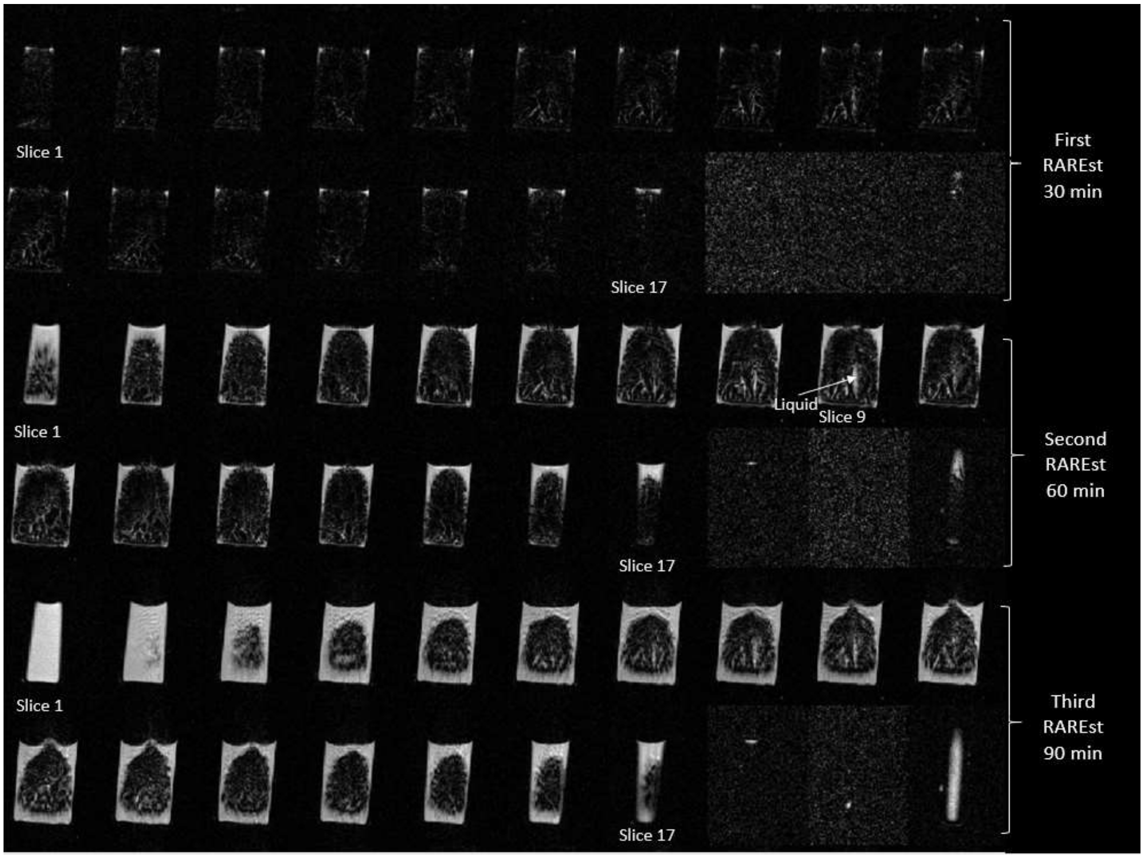

Figure 42. The three RAREst protocols performed for parallel one, with a solution consisting of 17 H_2O: 1 THF with the addition of water-wet SiO_2 solid particles. Figure shows the macroscopic crystal structure of THF hydrate after 30, 60 and 90 minutes. The second RAREst after 60 min show liquid phase within the solid hydrate, slice 9. A gradual melting can be seen from the outer edges and inwards from 30 to 90 min. Each pixel picture obtained represents an axial slice in the sample.

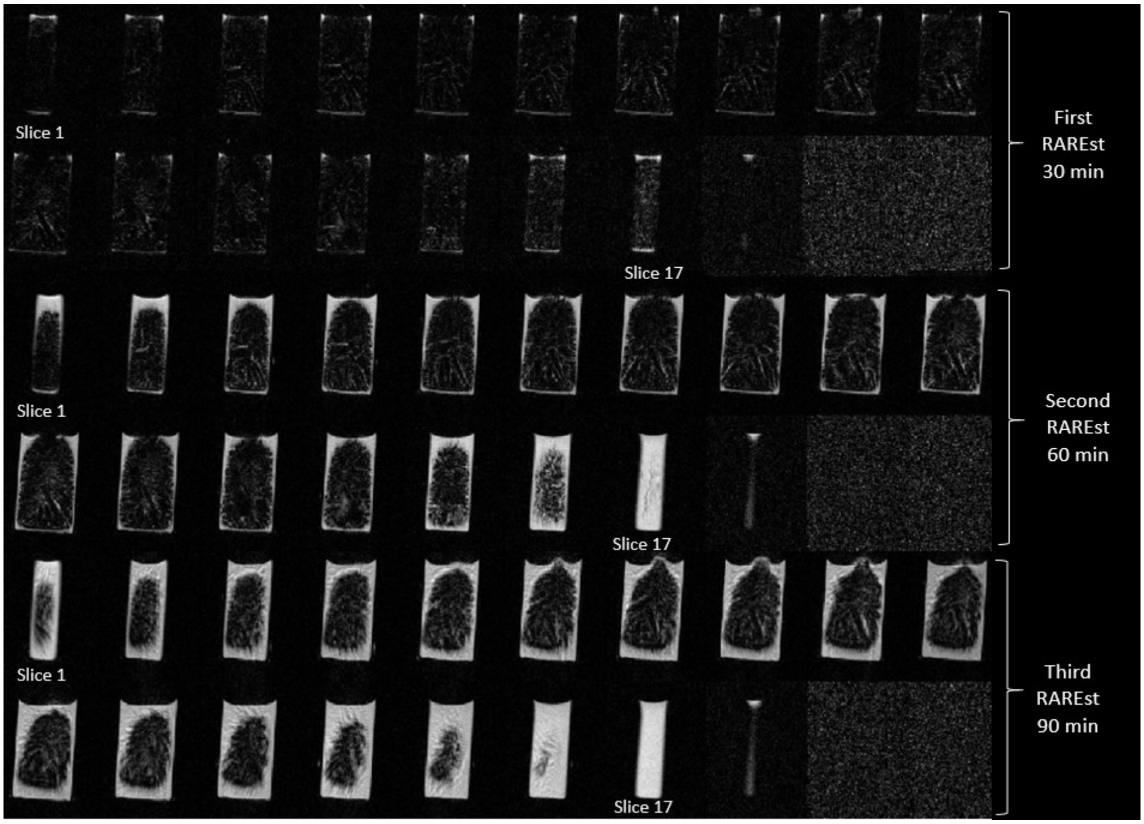

Figure 43. The three RAREst protocols performed for parallel two, with a solution consisting of 17 H_2O: 1 THF with the addition of water-wet SiO_2 solid particles. Figure shows the macroscopic crystal structure of THF hydrate after 30, 60 and 90 minutes. Solid hydrate is seen throughout the sample with only fractional accumulation of liquid phase between formed hydrate structures. A gradual melting can be seen from the outer edges and inwards from 30 to 90 min. Each pixel picture obtained represents an axial slice in the sample.

4.4.4 17 H_2O: 1 THF + Oil-wet SiO_2 particles

The RAREst scans of three parallel solutions of 17 H_2O: 1 THF with addition of oil-wet SiO_2 solid particles is presented in this section. The temperature at hydrate formation was -10ºC before the samples were placed in the MRI instrument. The three solutions were scanned simultaneously three times with the RAREst protocol, approximately 30 min for each protocol. Each slice shown in the figures represents an axial position within the sample, ref. figure 21 for slice distribution. Solid hydrate is shown by the black areas due to solid phases not yielding any signal intensity and liquid phase is shown by the bright areas.

Figure 44, 45 and 46 shows the RAREst images obtained for parallel one, two and three, respectively. The morphology of these figures shows solid hydrate formation throughout the sample with no significant cracks/accumulation of liquid within the sample. Only fractional accumulation of liquid phase between formed hydrate structures can be seen. The melting of the THF hydrate is seen to occur on the outer edges of the three parallel samples and moving inwards.

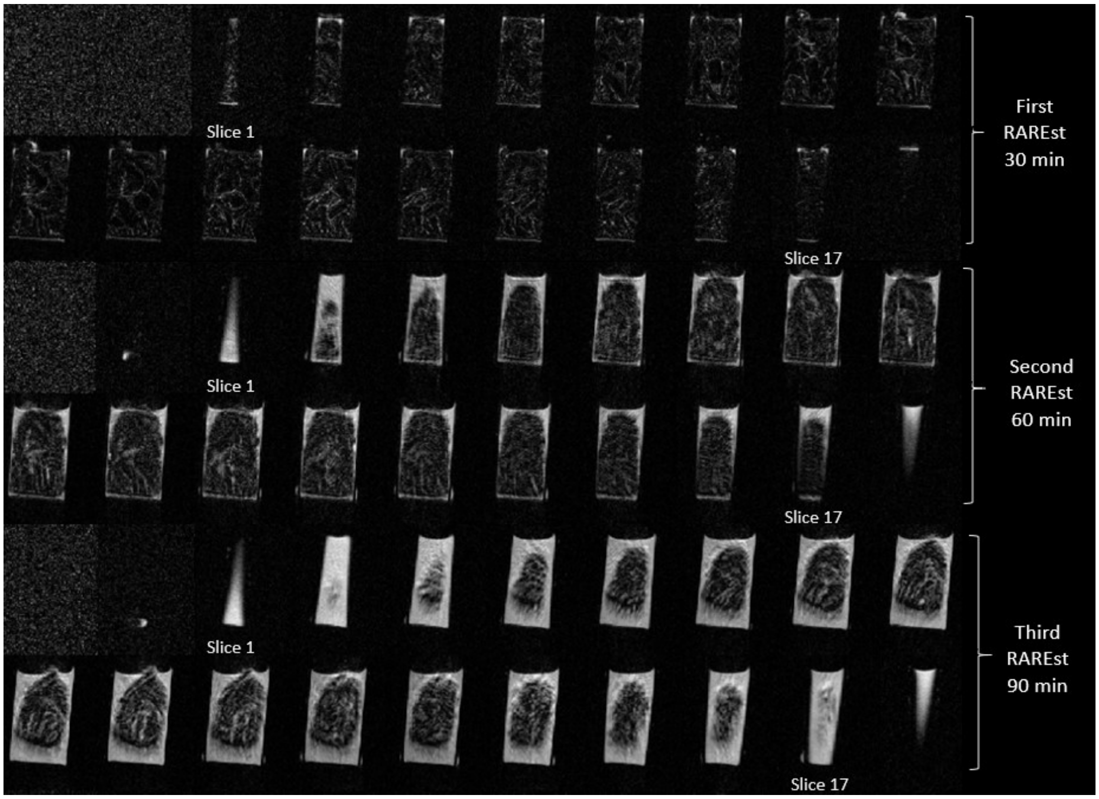

Figure 44. The three RAREst protocols performed for parallel one, with a solution consisting of 17 H_2O: 1 THF with the addition of oil-wet SiO_2 solid particles. Figure shows the macroscopic crystal structure of THF hydrate after 30, 60 and 90 minutes. Solid hydrate is seen throughout the sample with only fractional accumulation of liquid phase between formed hydrate structures. A gradual melting can be seen from the outer edges and inwards from 30 to 90 min. Each pixel picture obtained represents an axial slice in the sample.

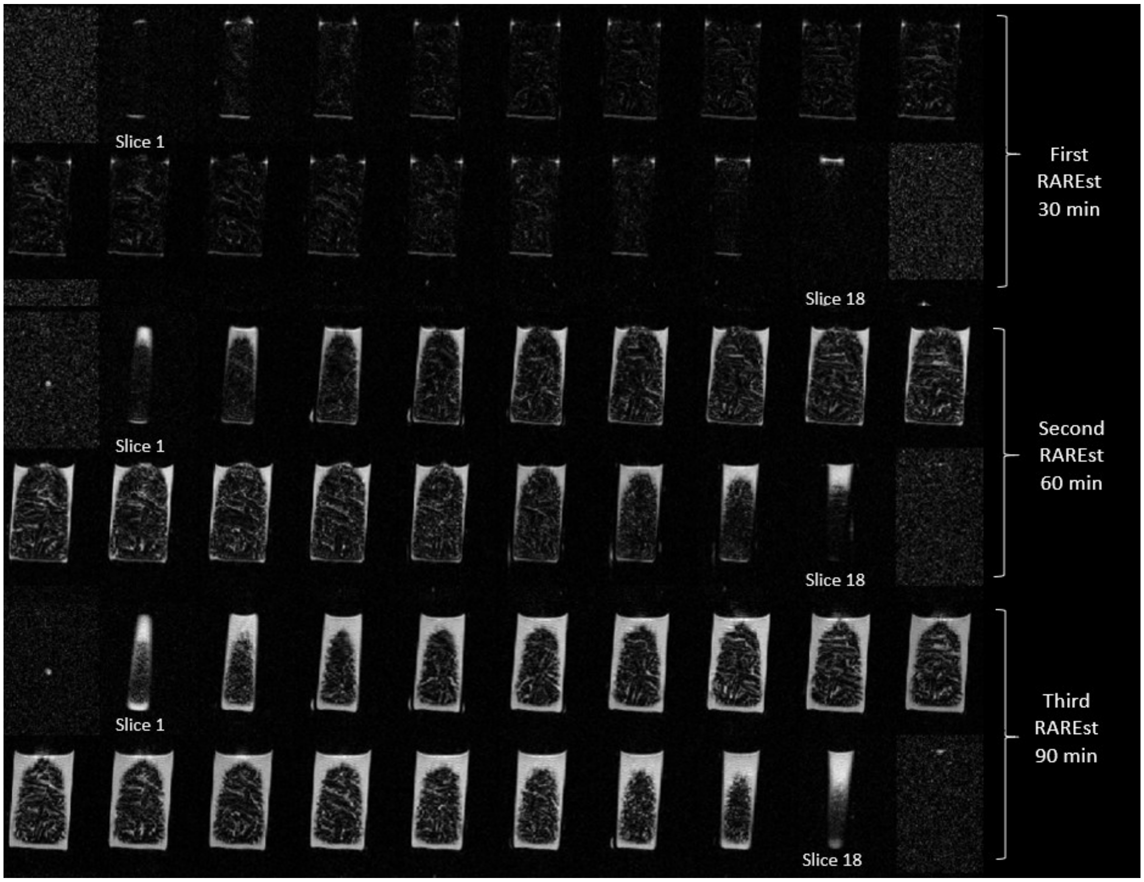

Figure 45. The three RAREst protocols performed for parallel two, with a solution consisting of 17 H_2O: 1 THF with the addition of oil-wet SiO_2 solid particles. Figure shows the macroscopic crystal structure of THF hydrate after 30, 60 and 90 minutes. Solid hydrate is seen throughout the sample with only fractional accumulation of liquid phase between formed hydrate structures. A gradual melting can be seen from the outer edges and inwards from 30 to 90 min. Each pixel picture obtained represents an axial slice in the sample.

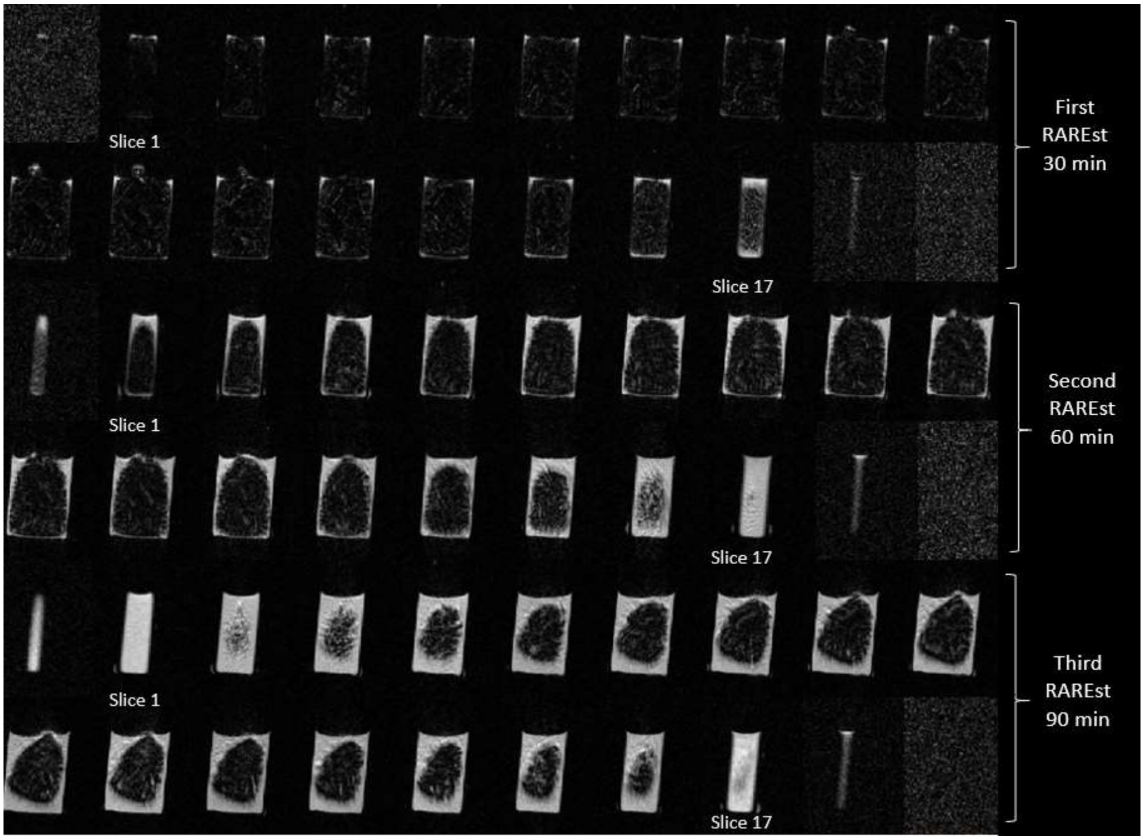

Figure 46. The three RAREst protocols performed for parallel three, with a solution consisting of 17 H_2O: 1 THF with the addition of oil-wet SiO_2 solid particles. Figure shows the macroscopic crystal structure of THF hydrate after 30, 60 and 90 minutes. Solid hydrate is seen throughout the sample with only fractional accumulation of liquid phase between formed hydrate structures. A gradual melting can be seen from the outer edges and inwards from 30 to 90 min. Each pixel picture obtained represents an axial slice in the sample.

4.4.5 Bulk solution of 17 H_2O: 1 THF

Only one experiment with a solution consisting of 17 H_2O: 1 THF in bulk was analyzed with the RAREst protocol. The temperature at hydrate formation was -10ºC before the samples were placed in the MRI instrument. The three RAREst protocols are shown in figure 47, 48 and 49 below. Each slice shown in the figures represents an axial position within the sample, ref. figure 21 for slice distribution. Solid hydrate is shown by the black areas due to solid phases not yielding any signal intensity and liquid phase is shown by the bright areas.

The images in figure 47, 48 and 49 show the macroscopic crystal structure of THF hydrate, where solid hydrate is seen throughout the solution, with only fractional accumulation of liquid between the formed hydrate structure. A small area approximately in the middle of the sample can be seen to contain some liquids, slice 8 and 15 in figure 48 and 49, respectively.

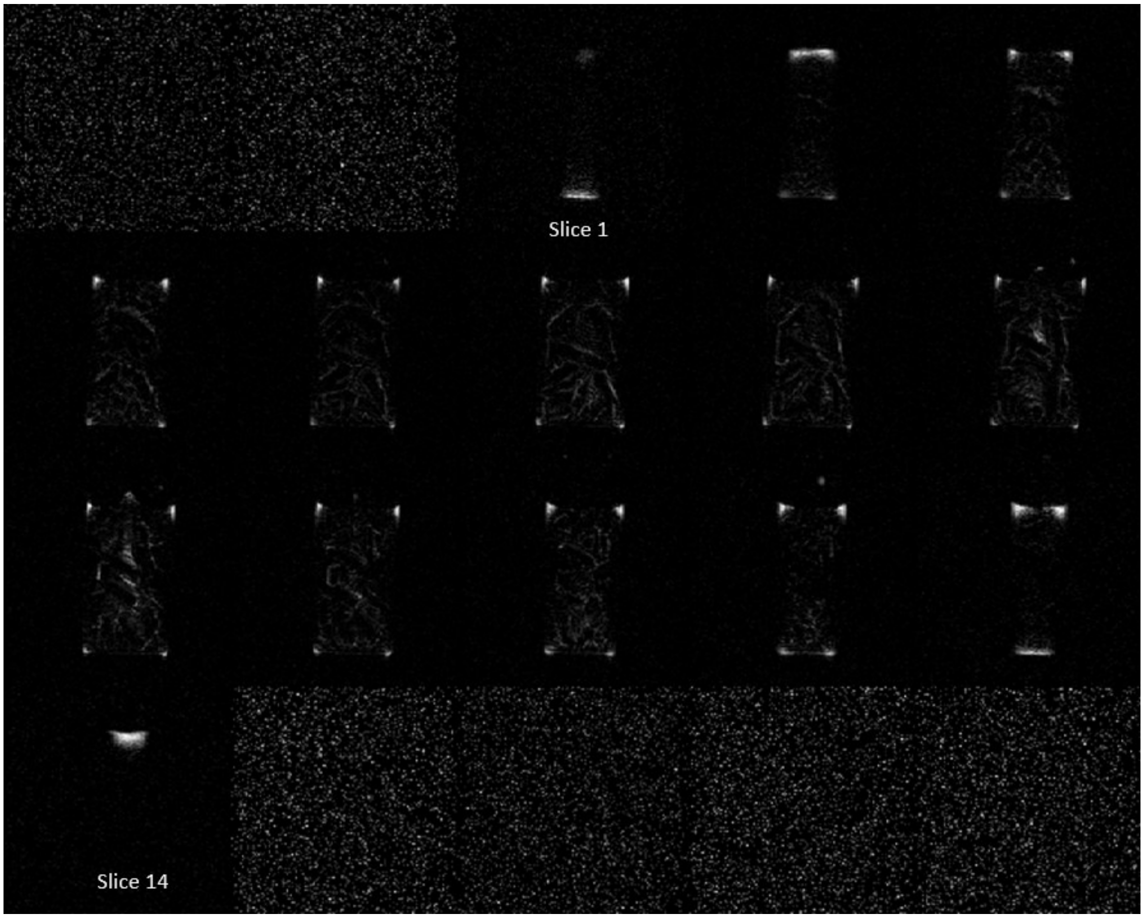

Figure 47. The first RAREst image of the THF hydrate, with a solution consisting of 17 H_2O: 1 THF without any particles added. This RAREst consisted of 20 slices after 30 minutes and show slight melting on the outer edges of the sample.

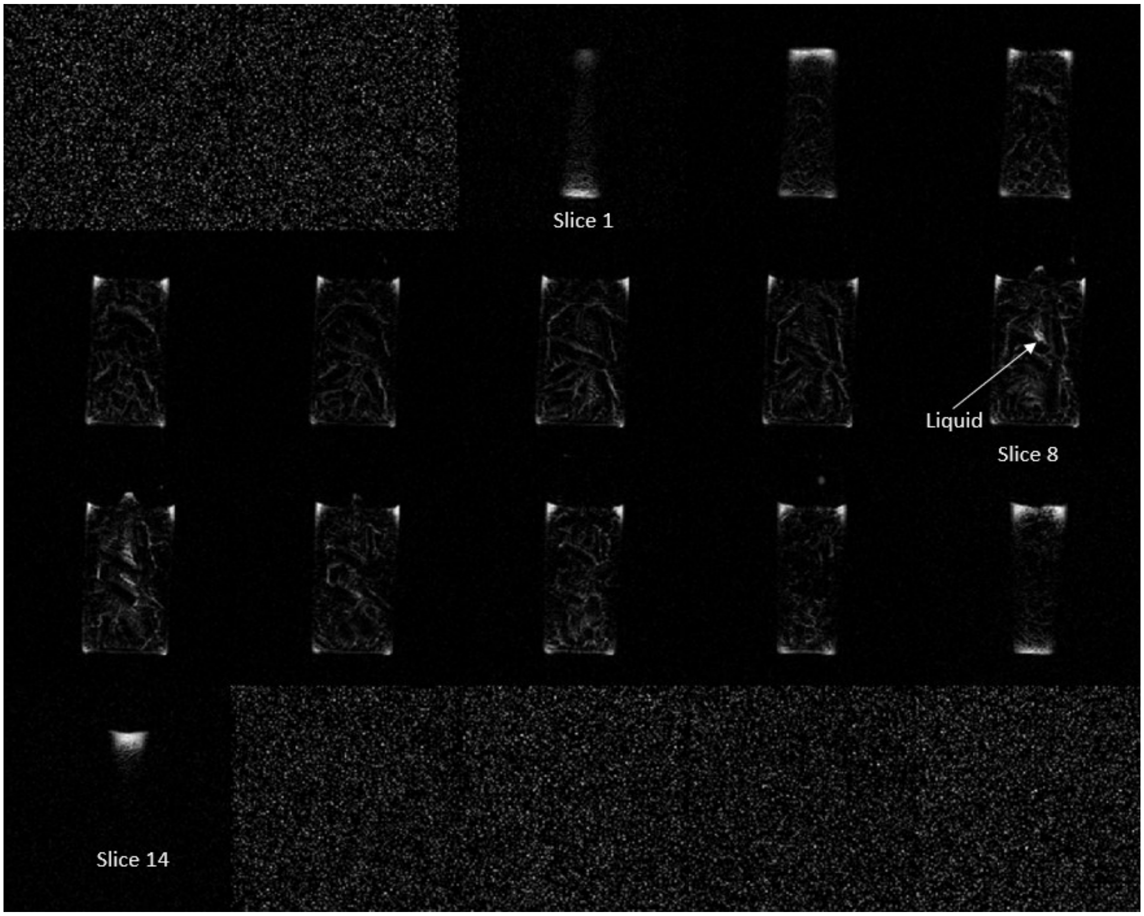

Figure 48. The second RAREst image of the THF hydrate, with a solution consisting of 17 H_2O: 1 THF without any particles added. This RAREst consisted of 20 slices after 60 minutes and show slight melting on the outer edges of the sample. Small accumulation of liquid phase can be seen in slice 8.

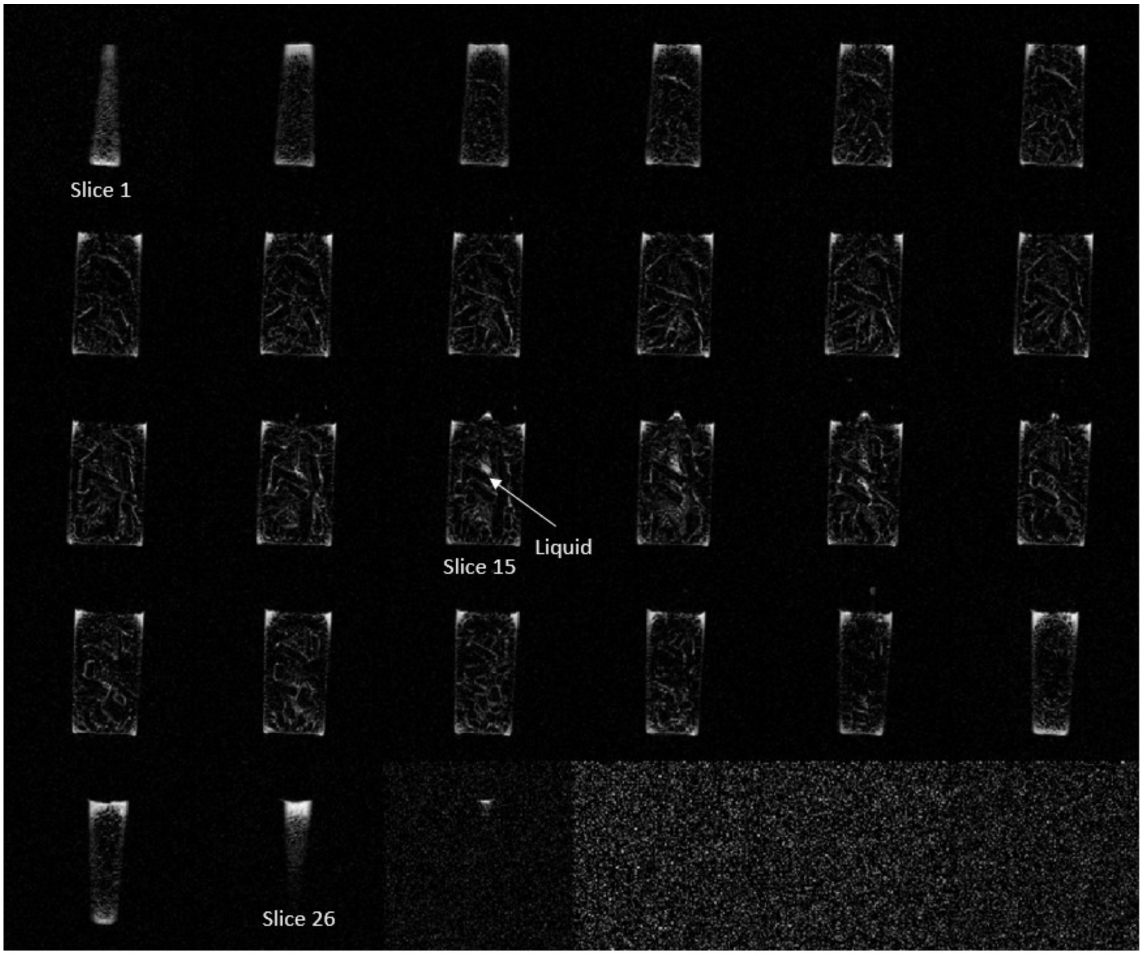

Figure 49. The third RAREst image of THF hydrate, with a solution consisting of 17 H_2O: 1 THF without any particles added. This RAREst consisted of 30 slices after 90 minutes and show slight melting on the outer edges of the sample. Small accumulation of liquid phase can be seen in slice 15.

4.4.6 Bulk water & water + Bentheimer particles

Pure ice in bulk solution and with addition of Bentheimer solid particles were analyzed for comparison of the macroscopic crystal structure with THF hydrate. The temperature at ice formation was -2ºC for the bulk solution and -10ºC for the solution with Bentheimer solid particles. Figure 50 shows three parallel solutions with pure ice formation in bulk solution and figure 51 shows three parallel solutions with pure ice with Bentheimer solid particles. The morphology from both are seen to form solid ice formation without any liquid phase visible, only on the outer edges of the sample.

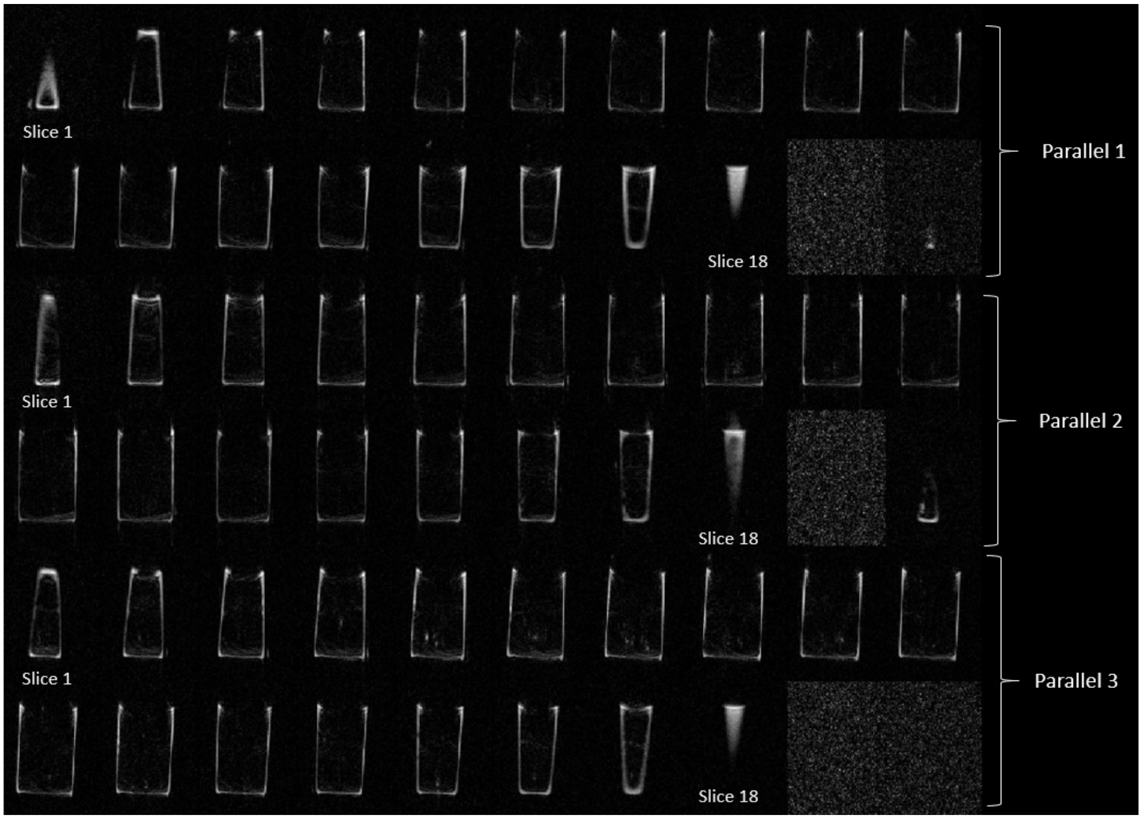

Figure 50. The RAREst image of three parallel samples after 30 minutes showing the macroscopic crystal structure of pure ice in bulk solution. Solid ice formation is seen throughout the samples.

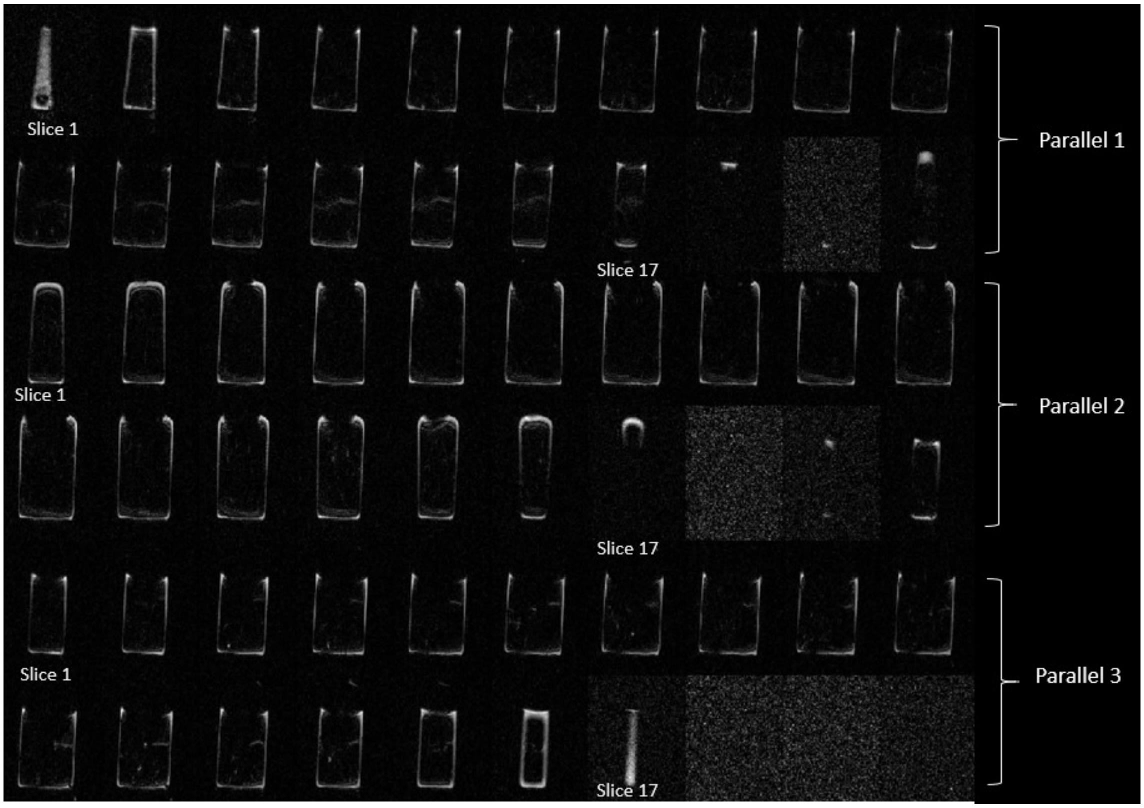

Figure 51.The RAREst image of three parallel samples after 30 minutes showing the macroscopic crystal structure of pure ice with the addition of Bentheimer solid particles. Solid ice formation is seen throughout the samples.

4.5 Discussion- MRI technique for visualization of the macroscopic crystal structures of THF hydrate

Magnetic Resonance Imaging (MRI) analysis of the macroscopic crystal structure and morphology of pure ice in bulk solution and with the addition of Bentheimer solid particles gave solid structure throughout the sample for all experiments. Comparison of the morphology of ice with THF hydrate showed a more staggered structure for THF hydrate with accumulation of fractional amount of liquid phase between formed THF hydrate structures, whereas ice formed solid throughout the solution, figure 52. The morphology seen in figure 52 shows a significantly different formation for ice versus THF hydrate. These results can either suggest a hydration number of THF that is not ideal or the formation of THF hydrate in the solution could lead to a local composition change in the liquid phase due to hydrates forming randomly around and trapping liquids.

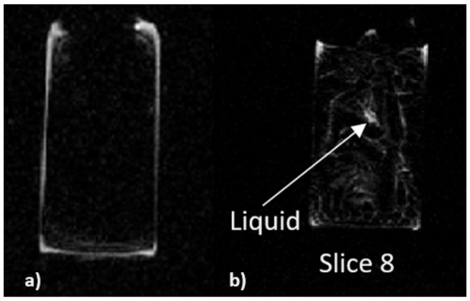

Figure 52. Figure shows a) ice formation and b) 17 H_2O: 1 THF hydrate in bulk. The figure is extracted slices from the second RAREst from figure 48 and 50. The figure show that ice formation and THF hydrate formation varies significantly.

The phase diagram (figure 6) shows that THF hydrates can form up to 4,5ºC with a 20 wt.% THF solution (17 H_2O: 1 THF). Liquid phase trapped between formed hydrates structures could lead to a local composition change in the solution, which could move the remaining liquid between the formed hydrates from inside the hydrate stability zone to outside since the composition of the solution have changed. This is proposed to be one of the possible reasons for why there is liquid inside a visible solid hydrate. Another option is the possibility of the ideal hydration number of 17 moles of H_2O to 1 mole THF to not be the ideal hydration number. Additional experiments with mole ratios above and below the hydration number chosen for this thesis would provide additional data on this hypothesis.

The morphology of the experiments performed with solid particles was observed to form staggered hydrate structures with liquid phase between the formed hydrate structure in addition to accumulation of liquid in the center of the sample for some of the experiments, figure 53. The most significant accumulation of liquids within the hydrate was seen for the experiments performed with Illite and Bentheimer, where Illite formed channels where liquid phase accumulated, figure 53a and b. Addition of Bentheimer particles also displayed this same trend with channels of liquids between the hydrate structure. It was also observed that when the Bentheimer hydrate melted the liquid phase inside the hydrate structure increased, figure 53c and d. However, since the difference in signal intensity for each of the RAREst performed has not been corrected for, direct comparison between different RAREst could be misleading, and correction of the signal intensity to be the same for all images should be performed for verification of analysis of the results. The results are however thought to give an indication to trends occurring.

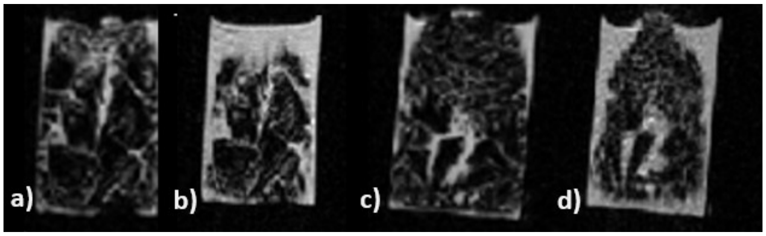

Figure 53. Figure shows the same axial position within a given sample consisting of 17 H_2O: 1 THF where a) is Illite after 60 minutes for parallel one (figure 36), b) Illite after 90 minutes for parallel one (figure 36), c) Bentheimer after 60 minutes for parallel three (figure 51) and d) Bentheimer after 90 minutes for parallel three (figure 51). These figures show that when Illite and Bentheimer melts the liquid phase and morphology for the formed hydrate structure changes considerably.

The morphology for the experiments with oil-wet and water-wet SiO_2 solid particles shows liquid phase between formed hydrate structure, figure 54. The macroscopic crystal structure formed is seen to not form the staggered hydrates as for the experiments with Illite and Bentheimer (figure 53). The addition of oil-and water-wet SiO_2 presented liquids between formed hydrate structure but without significant channel formation such as for Illite and Bentheimer. Since Illite is a mineral present in Bentheimer sandstone, table 9 for detail composition of Bentheimer sandstone, the similarity in shapes and liquid accumulation between these two is good.

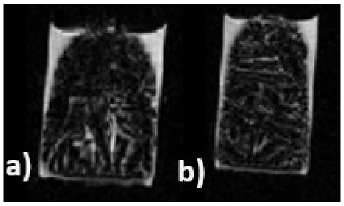

Figure 54. Figure shows 17 H_2O: 1 THF hydrate formation with the addition of a) water-wet SiO2 for parallel one (figure 42) and b) oil-wet SiO2 for parallel 2 (figure 45). Both samples show results from after the second RAREst.

Furthermore, the parallel samples prepared for each series was reasonably similar and results suggest that structures seen for the various particles added is reproducible. It can also be seen for the different RAREst images a gradual melt from the outer edges of the sample and inwards while the sample is being heated by the surrounding air. This melting is seen for all experiments performed.

4.6 Results- The CO_2 hydrate formation in Bentheimer cores

The following section provides the results obtained from the CO_2 hydrate formation in a Bentheimer sandstone core, summary of all experiments is listed in table 16. In total nine experiments were performed with nine different cores in collaboration with Jarand Gauteplass and Stian Almenningen. The experiments will be presented in the order of increasing injection rate where Baseline experiments will be presented first. The pressure gradient across the core is used to show pressure buildup in combination with resistivity and temperature changes throughout the experiment. Increase in pressure indicates blockage in the core (i.e. hydrates forming) in **combination** with temperature increase and resistivity increase. The CO_2 pump was stopped when pressure gradient exceeded approximately 85 bar. Hydrate formation was also verified when pressure decreased after the CO_2 pump was shut off, this was due to gas being consumed as hydrates and consequently lowering the pressure until the CO_2 pump was started again.

Three of the experiments performed were baseline experiments performed at 70 bar, room temperature (22ºC) and with 3,5 wt.% NaCl brine solutions with the three different injection rates chosen; 0,5, 5 and 10 ml CO_2/min. After the baseline experiments were finished the CO_2 pump was set to constant pressure (no flow rate), temperature set to 4ºC and the core was left-over night to record resistivity when hydrates formed. These results are presented in Table 16 as 1_a, 2_b and 3_c, ref. appendix D for additional data of the Baseline experiments during CO_2 hydrate formation.

Each of the experiments will be presented in individual sections except the baseline experiment which are presented together.

Table 16.Summary of results from CO_2 hydrate formation in Bentheimer sandstone core. Table list the flow rates used for each experiment, hydrate formation time, PV (pore volume) before hydrate formation and inhibitors used for dissociation. All experiments performed at 70 bar

Exp. nr	Salinity (wt.% NaCl)	Temperature (°C)	Flow Rate (ml/min)	Hydrate formation time (hour)	PV injected (frac)	Inhibitor used	Comment
1	3,50	21	5,0	No hydrate	-	-	Baseline
2	3,50	21	0,5	No hydrate	-	-	Baseline
3	3,50	21	10	No hydrate	-	-	Baseline
1_a	3,50	4	0,0	12,7	3,42	-	Baseline cont.
2_b	3,50	4	0,0	14,0	1,34	-	Baseline cont.
3_c	3,50	4	0,0	2,9	1,26	-	Baseline cont.
4	3,50	4	0,5	3,0	1,4	MeOH & thermal	
6	5,00	4	0,5	10,0	4,6	-	
8	7,00	4	0,5	No hydrate	NA	-	
9	3,50	7	0,5	No hydrate	NA	-	
7	5,00	4	5,0	2,0	9,4	-	
5	3,50	4	10	0,4	2,2	MeOH	

Table 17 below shows the core properties for all Bentheimer sandstone cores used in the different experiments. Before each experiment the porosity of the core and absolute permeability was calculated. Absolute permeability was calculated by flooding the core when mounted in the Hassle holder with desired brine solution at different flow rates and then calculating the mean permeability. Average porosity and permeability for all cores were calculated to 22% and 1,3 Darcy, respectively.

Table 17. Core properties for all experiments with calculated porosity, irreducible water saturation and permeability.

Exp. nr	Salinity (wt.% NaCl)	Length (cm) ±3E-02	Diameter (cm) ± 2E-02	Bulk volume (cm^3)	Pore volume, (cm^3)	Porosity (%) 1)	Saturation S_w	Saturation at bt 2), S_{iw_bt}	Absolute Permeability, k (Darcy) 1)
5	3,50	14,76	5,17	309,92	68,78	22,19	0,95	0,43	1,13
4	3,50	14,81	5,17	310,97	67,96	21,85	0,95	0,58	1,19
1	3,50	14,54	5,18	306,49	67,46	22,01	0,91	0,37	1,20
2	3,50	14,51	5,16	302,97	67,56	22,30	0,95	0,52	1,21
3	3,50	14,46	5,09	293,92	64,54	21,96	0,93	0,37	1,03
6	5,00	14,59	5,17	306,61	67,29	21,95	0,93	0,59	1,24
7	5,00	14,66	5,17	307,75	67,69	21,99	0,94	0,36	1,24
8	7,00	14,40	5,17	302,23	66,21	21,91	0,94	0,57	1,14
9	3,50	14,91	5,18	314,21	69,89	22,24	0,94	0,53	1,46

1) Porosity, permeability and saturation calculations shown in Appendix B.

2) Water saturation at CO_2 gas **B**reak**T**hrough.

Irreducible water saturation at gas breakthrough (S_{iw_bt}) was calculated by registering the amount of water being displaced by the liquid CO_2 injected until CO_2 breakthrough. Figure 55 below shows the S_{iw_bt} versus injection rate for the different core used in this thesis. The figure shows a satisfactory correlation between injection rate and S_{iw_bt} for each core since the experiments with the same injection rate have a similar saturation at breakthrough.

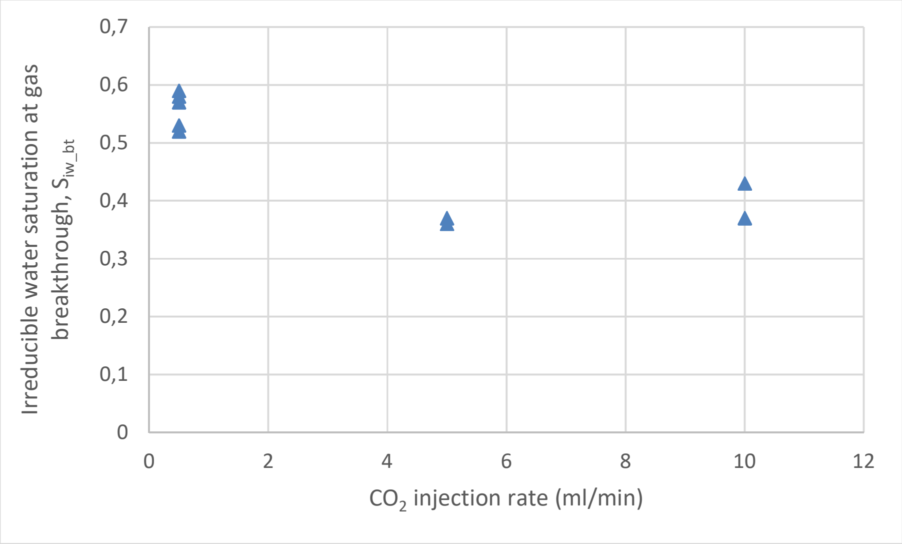

Figure 55. Water saturation at gas breakthrough versus injection rate for the experiments performed. The points represent each of the different cores used. The graph shows that the S_{iw_bt} decreases by increase in injection rate from 0,5 to 5 ml CO_2/min and from 5 to 10 ml CO_2/min the saturation is quite consistent.

4.6.1 Experiment 1-3: Baseline experiments

Baseline experiment were performed at 70 bar and room temperature (approximately 22ºC) with a saturated core of 3,5 wt.% NaCl and with the three varying injection rates chosen. Baseline experiments were performed for registration of resistivity and permeability at the various injection rates when the system is outside the HSZ. Figure 56, 57 and 58 below shows the pressure and resistivity changes over time for 0,5, 5 and 10 ml CO_2/min, respectively.

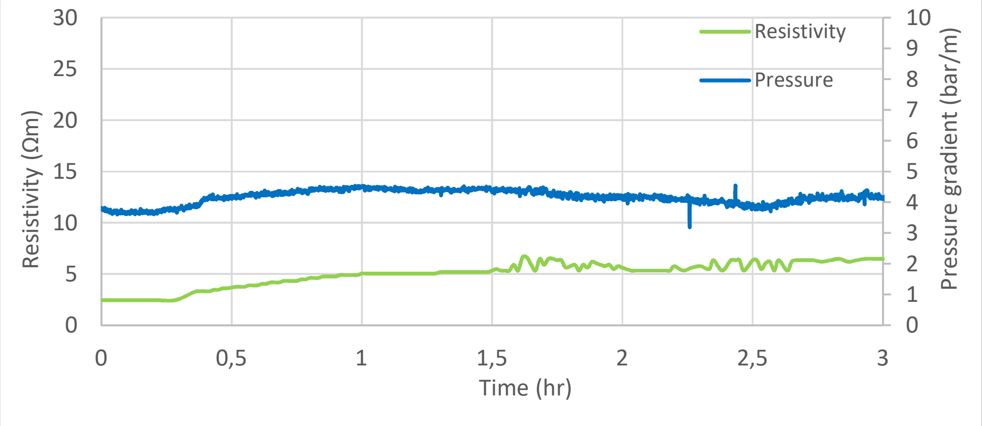

Figure 56. Pressure gradient and resistivity over time for experiment 2 with 0,5 ml CO_2/min.

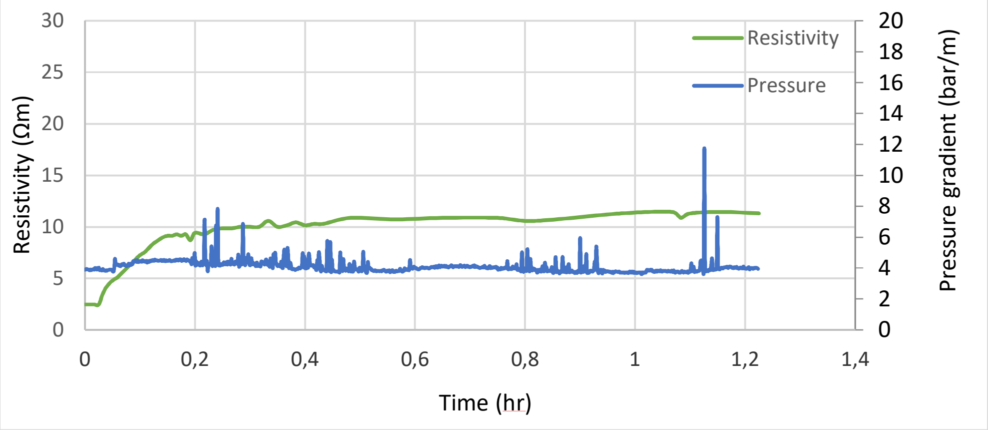

Figure 57. Pressure gradient and resistivity over time for experiment 1 with 5 ml CO_2/min.

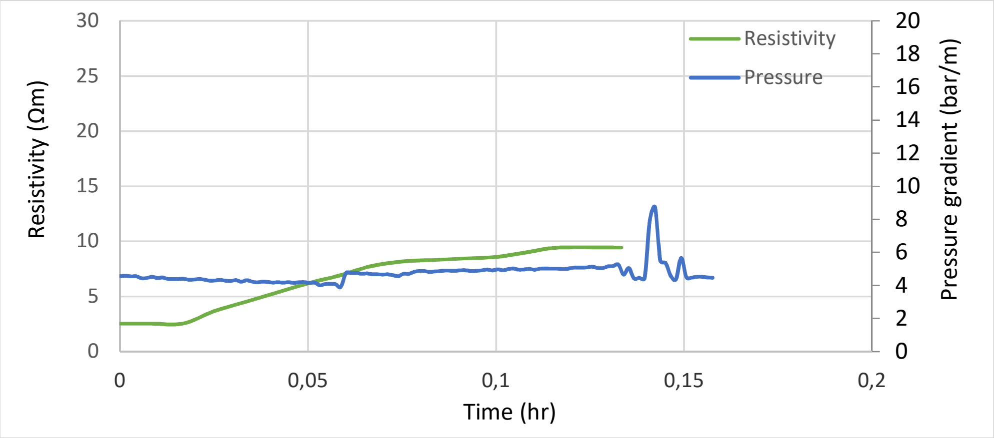

Figure 58. Pressure gradient and resistivity over time for experiment 3 with 10 ml CO_2/min.

After the three baseline experiments finished the core was set to 4ºC and bypass valve between inlet and outlet side was opened (i.e. closed system) and pressure set to be constant at 70 bar (i.e. zero injection of CO_2). All the tree different cores were left over-night and resistivity registered by use of web camera. Successful hydrate formation occurred for all baseline experiments and can be seen in figure 59.

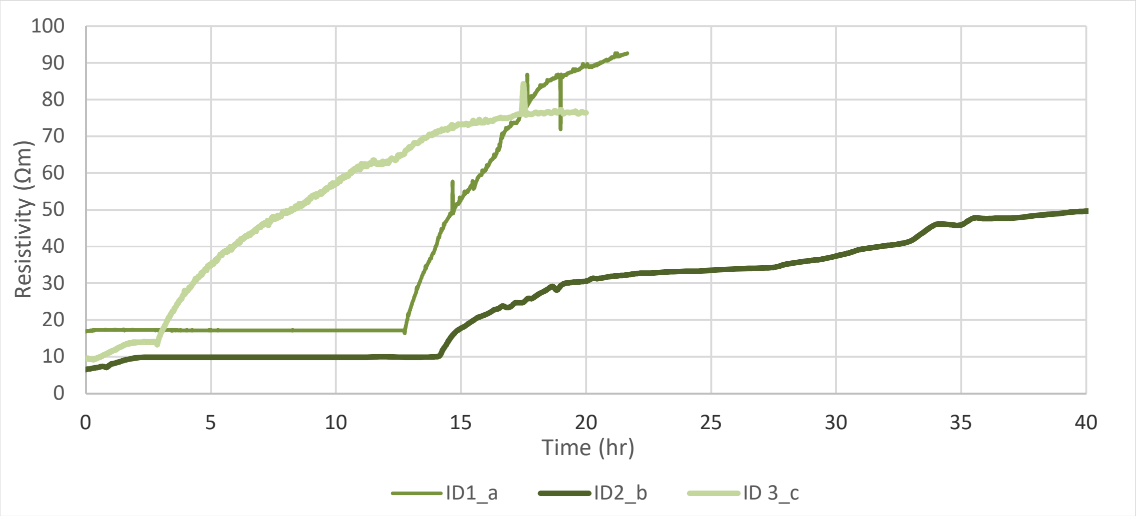

Figure 59. Resistivity measurements over time for experiment 1_a, 2_b and 3_c.

4.6.2 Experiment 4: 0,5 ml CO_2/min [3,5 wt.% NaCl at 4ºC]

Experiment 4 was performed with 0,5 ml CO_2/min with a brine salinity of 3,5 wt.% NaCl and a core temperature of 4ºC. Successful CO_2 hydrate formed was dissociated by chemical- (30 wt.% MeOH) and thermal stimulation.

Figure 60 below shows how temperature, resistivity and pressure gradient changes over time with 0,5 ml CO_2 injected per minute. Resistivity was logged manually. The temperature graph shows a slight increase, a peak, at 1,5 hours and this can be the first sign of the exothermic hydrate nucleation process of CO_2. In total 94 ml CO_2 was injected before the pressure gradient reached a maximum at 132 bar/m, and thus confirming successful hydrate plug. When the pressure gradient exceeded 85 bar/m the CO_2 pump was shut off and decrease after this point (3,2– 3,6 hours) is due to CO_2 being encapsulated by the water molecules forming hydrates and consequently pressure gradient decrease until pump was put on again, or hydrate formation. Both the pressure gradient increase- and decrease is an indication of successful hydrate formation inside the core. When the pressure gradient decreased to 20 bar/m the CO_2 pump was disconnected and the methanol pump connected for chemical dissociation of the plug. Resistivity measurements were not possible during methanol injection.

The increase in the pressure gradient from 20-130 bar/m was seen when methanol was injected (methanol pump set to 0,5 ml MeOH/min) and verified the formed hydrate plug. Methanol injection lasted for approximately 1 hour without no dissociation of formed plug, seen by no pressure or temperature changes. In total 3,6 ml MeOH was injected. Thermal stimulation was then chosen as next dissociation method. Temperature was set to 10 ºC and the CO_2 pump reconnected.

Successful dissociation of formed plug was seen at 5,6 hours with rapid pressure gradient drop in combination with temperature exceeding the hydrate stability zone for CO_2 at 8,3 ºC (figure 7, pressure-temperature diagram for CO_2 hydrate at different salinities). The experiment ended after 5,6 hours.

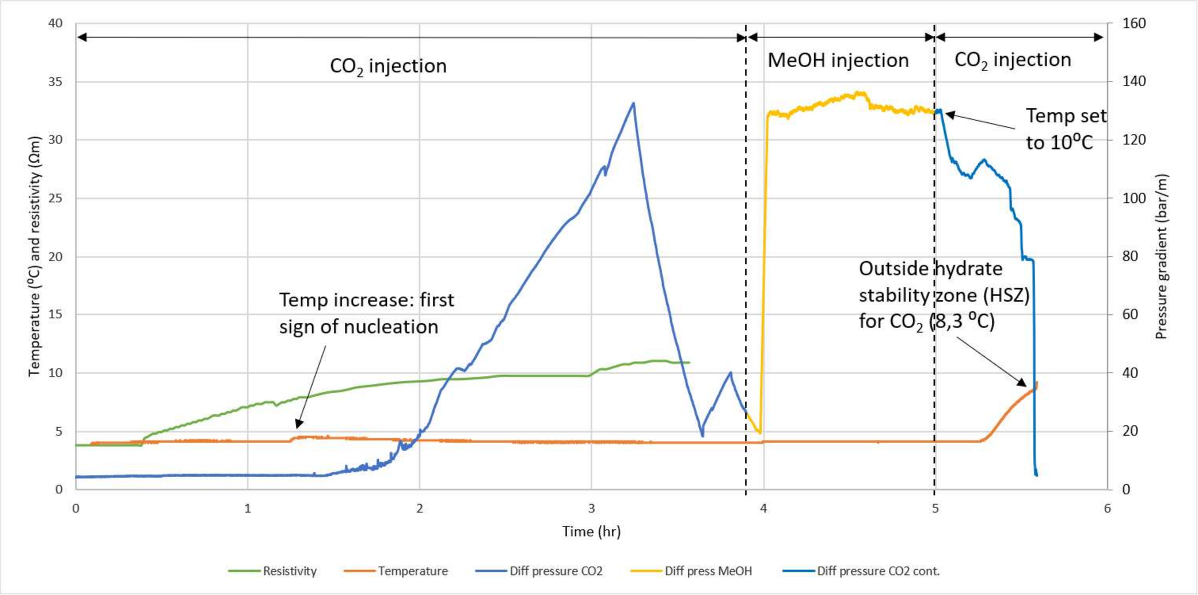

Figure 60. Experiment no 4. 0,5 ml CO_2/min with 3,5 wt.% NaCl solution at 4ºC and MeOH injection. Graphs shows how temperature, pressure gradient and resistivity changes over time with CO_2 hydrate formation.

4.6.3 Experiment 6: 0,5 ml CO_2/min [5,0 wt.% NaCl at 4ºC]

Experiment 6 was performed with 0,5 ml CO_2/min with a brine salinity of 5,0 wt.% NaCl and a core temperature of 4ºC. Successful CO_2 hydrate formed was dissociated by thermal stimulation after experiment ended.

Figure 61 shows how temperature, pressure gradient and resistivity changes over time for experiment 13. Resistivity was logged manually. The temperature graph shows a slight increase, a peak, just before the pressure gradient increases rapidly at 9,4 hours. This peak can be the first sign of the exothermic hydrate nucleation process. In total 306 ml CO_2 was injected before the pressure gradient reached a maximum at 140 bar/m. When the pressure gradient exceeded 85 bar the CO_2 pump was shut off and pressure gradient decrease after this point is (10,5– 18 hours) is due to CO_2 being encapsulated by the water molecules forming hydrates. Steady resistivity increase is seen throughout the experiment. The experiment was completed after 20 hours.

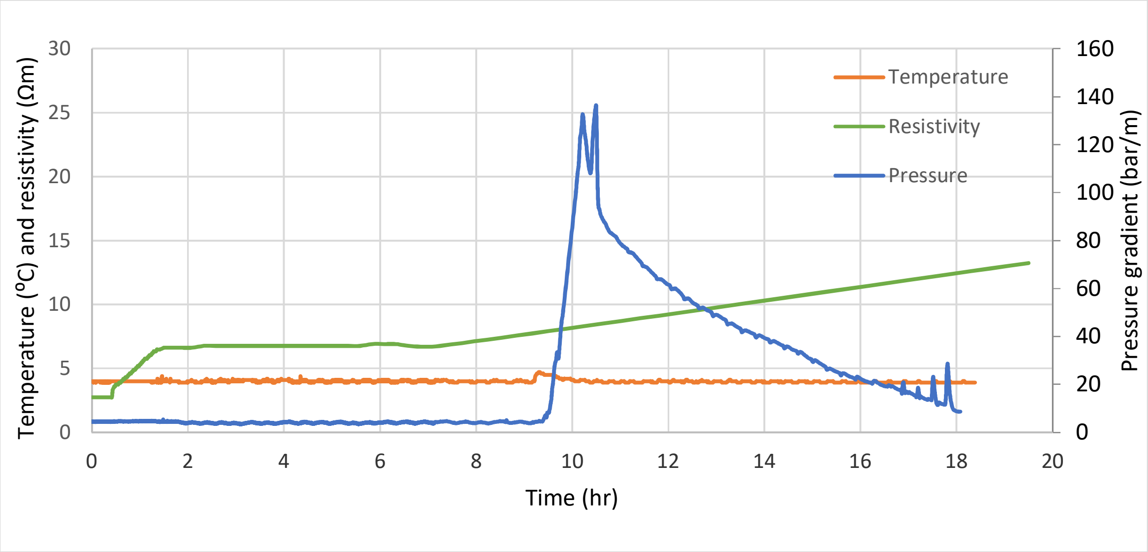

Figure 61. Experiment no 6. 0,5 ml CO_2/min with 5,0 wt.% NaCl solution at 4ºC. Graphs shows how temperature, pressure gradient and resistivity changes over time with CO_2 hydrate formation.

4.6.4 Experiment 8: 0,5 ml CO_2/min [7,0 wt.% NaCl at 4ºC]

Experiment 8 was performed with 0,5 ml CO_2/min with a brine salinity of 7,0 wt.% NaCl and a core temperature of 4ºC. Figure 62 below shows how temperature, pressure gradient and resistivity changes over time for experiment 8. The graph shows no hydrate formation, only instrumental fluctuations are seen on the graph. The resistivity was logged manually and stopped logging after normal working hours.

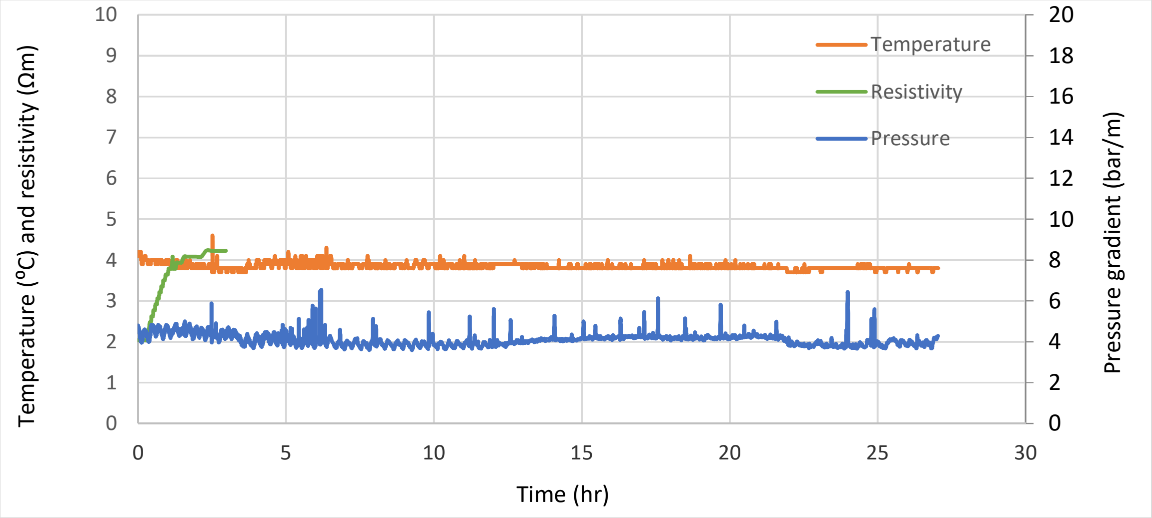

Figure 62. Experiment no 8. 0,5 ml CO_2/min with 7,0 wt.% NaCl solution at 4ºC. Graphs shows how temperature, pressure gardient and resistivity changes over time.

4.6.5 Experiment 9: 0,5 ml CO_2/min [3,5 wt.% NaCl at 7ºC]

Experiment 9 was performed with 0,5 ml CO_2/min with a brine salinity of 3,5 wt.% NaCl and a core temperature of 7ºC. Figure 63 below shows how temperature, pressure gradient and resistivity changes over time for experiment 16. The graph shows no hydrate formation at 7ºC. The resistivity was logged manually, and a web camera set up to register the resistivity outside normal working hours.

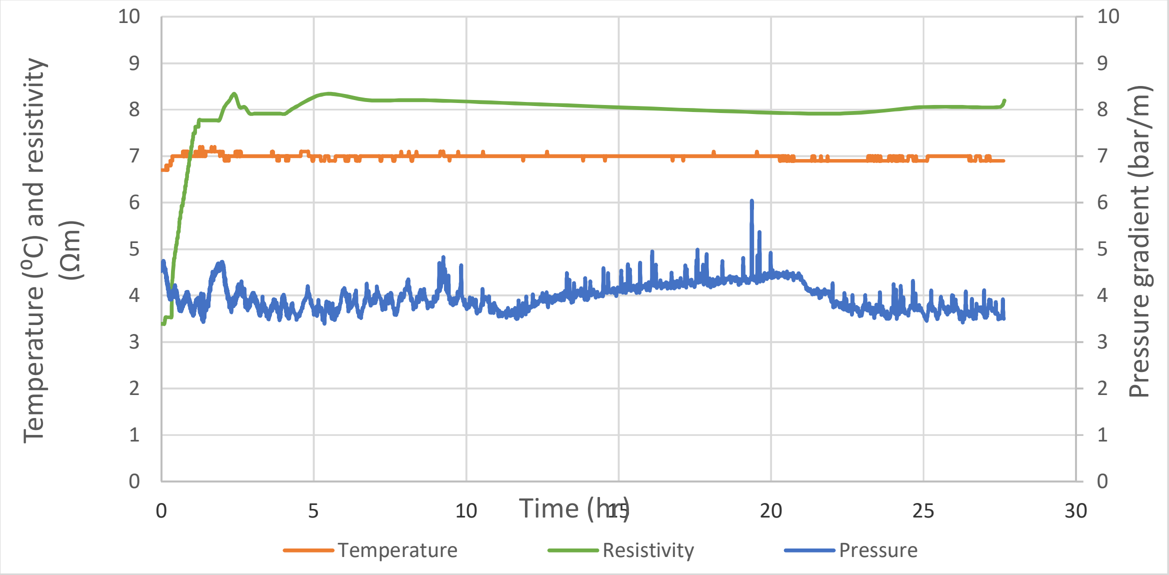

Figure 63. Experiment no 9. 0,5 ml CO_2/min with 3,5 wt.% NaCl solution at 7ºC. Graphs shows how temperature, pressure gradient and resistivity changes over time.

4.6.6 Experiment 7: 5 ml CO_2/min [5,0 wt.% NaCl at 4ºC]

Experiment 7 was performed with 5 ml CO_2/min with a brine salinity of 5,0 wt.% NaCl and a core temperature of 4ºC. The plug which formed was dissociated by thermal stimulation after experiment ended.

Figure 64 shows how temperature, pressure gradient and resistivity changes over time for experiment 14. Resistivity was logged manually. Temperature fluctuations seen in figure 64 is due to the temperature sensor being mounted in the inlet side of the core (at 4ºC) and when liquid CO_2 at room temperature is being injected at 5 ml/min the difference between the core temperature and injected liquid caused these fluctuations. In total 635 ml CO_2 was injected before the pressure gradient reached a maximum at 105 bar/m. When the pressure gradient exceeded 85 bar/m the CO_2 pump was shut off and reduction in the pressure gradient after this point is (2,2– 2,3 hours) is due to CO_2 being encapsulated by the water molecules forming hydrates. Steady resistivity increase is seen throughout the experiment. Temperature stabilization after hydrate formation (2 hours) is due to CO_2 pump being shut off and no liquid CO_2 injected. The CO_2 pump was then set to constant pressure until the end of the experiment, no more hydrate formation was seen. Experiment was completed after 4,5 hours.

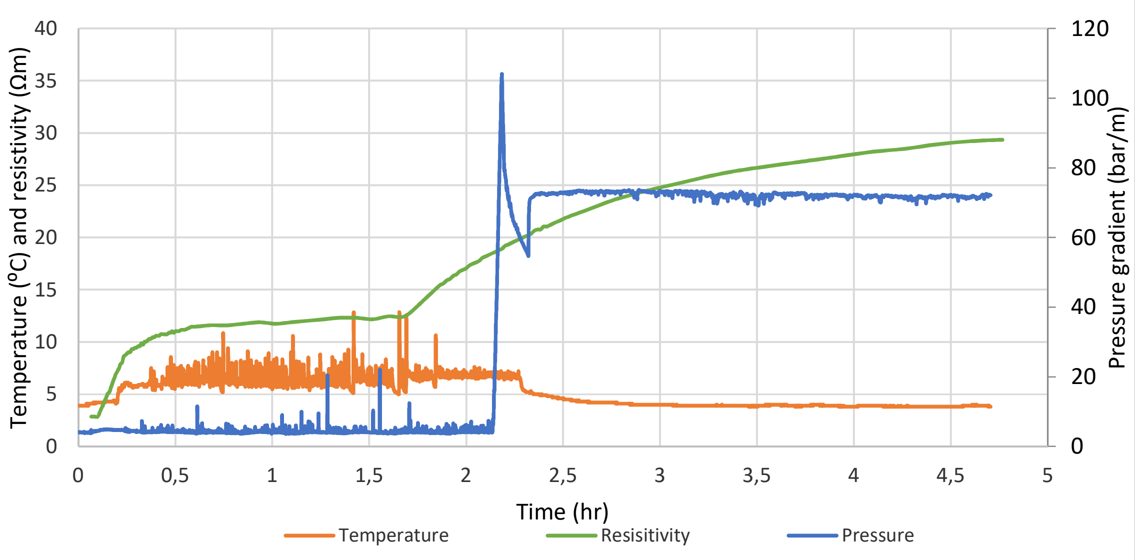

Figure 64. Experiment no 7. 5 ml CO_2/min with 5,0 wt.% NaCl solution at 4ºC. Graphs shows how temperature, pressure gradient and resistivity changes over time with successful hydrate formation.

4.6.7 Experiment 5: 10ml CO_2/min [3,5 wt.% NaCl at 4ºC]

Experiment 5 was performed with 10 ml CO_2/min with a brine salinity of 3,5 wt.% NaCl and a core temperature of 4ºC. Successful CO_2 hydrate formed was dissociated with methanol (30 wt.% MeOH).

Figure 65 below shows how the pressure gradient, temperature, resistivity and volume CO_2 injected from experiment start until 2 hours. Resistivity was logged manually. In total 160 ml CO_2 was injected before the first plug at 150 bar/m, point 1 in figure. The CO_2 pump was stopped in total 4 times due to the pressure gradient exceeding 85 bar/m, indicated by the 4 numbers in figure 65. Both the increase and decrease in the pressure gradient is due to hydrate formation of CO_2. When the pressure gradient exceeded 85 bar/m the CO_2 pump was shut off and reduction in the pressure gradient after this point is due to CO_2 being encapsulated by the water molecules forming hydrates. Steady resistivity increase is seen throughout the experiment. At point 3 and 4 there is a slight temperature increase, a peak, just before the pressure gradient increases, this temperature increase can be the first sign of hydrate formation due to hydrate formation being an exothermic process releasing energy.

MeOH was chosen for chemical dissociation of the formed plug. A solution of 30 wt.% MeOH was injected for approximately 2.5 hours before the pressure was seen to decrease rapidly, in total 24 ml MeOH injected. Resistivity measurements was not possible during MeOH injection. Successful dissociation of formed plug occurred at 4,3 hours. Experiment ended after approximately 4,2 hours.

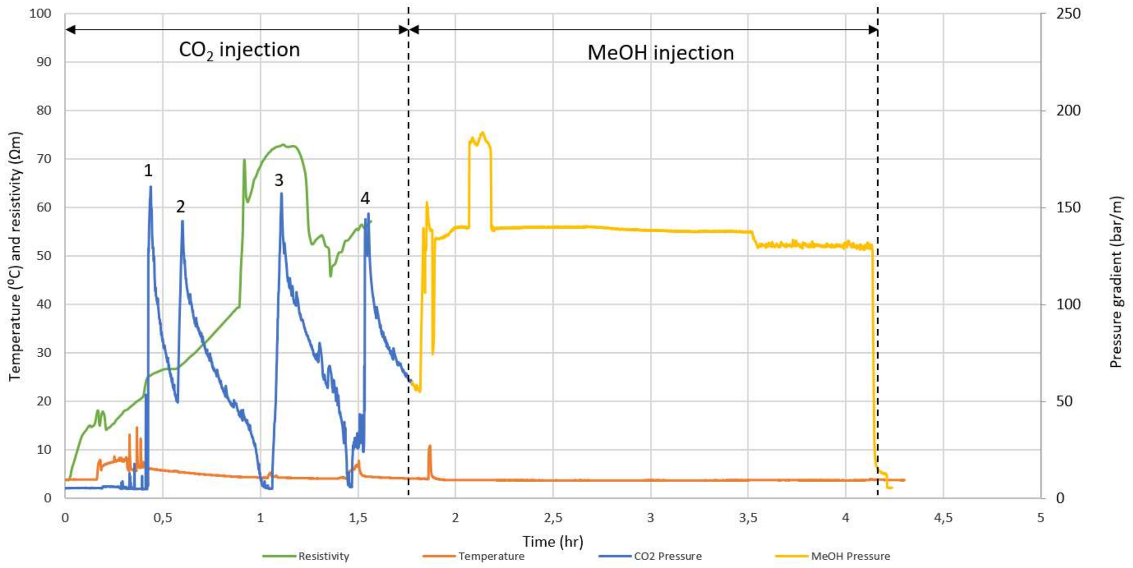

Figure 65. Experiment no 5. 10 ml CO_2/min with 3,5 wt.% NaCl solution at 4ºC and 30 wt.% MeOH injection. Graphs shows how temperature, pressure gradient, resistivity and volume injected over time. Point 1-4 indicates pressure peaks where CO_2 pump was shut of due to safety hazards.

4.7 Discussion- The CO_2 hydrate formation in Bentheimer cores

Nine experiments were performed with CO_2 as hydrate former in Bentheimer sandstone cores, where three of the experiments were baseline at the various injection rates. For the CO_2 hydrate formation experiments there were four experiments which resulted in successful hydrate formation.

The hydrate formation time recorded for all experiments was the time from injection started until maximum pressure gradient increase. The time until hydrate formation varied from 0,4 hours for experiment 5 (highest injection rate:10 ml CO_2/min) to no hydrate formation for experiment 9 (performed at 7°C) and experiment 8 (performed with a brine salinity of 7 wt.% NaCl).

Two experiments were performed under the same conditions (pressure, injection rate and salinity) with varying temperature, table 18 below. Temperature is a well-established physical inhibitor and mostly used in laboratory or other processes where the temperature can be regulated. Since an increase in temperature is known to be a good indicator of hydrate nucleation, the local peaks that can be seen right before a rapid pressure gradient increase for experiment nr 4, 6 and 7 could be the first indication of CO_2 hydrate nucleation. From the phase diagram of CO_2 (Figure 7), changing the system parameters from 4°C to 7°C changes the system from point 1 to 2. Table 18 shows that by increasing the temperature from 4°C to 7°C the hydrate formation time increases from 3 hours to no hydrate formation.

Table 18. Extraction of data from table 11. Summary of CO_2 core experiments with varying temperature.

Exp. no	Salinity (wt.% NaCl)	Temperature (°C)	Pressure (bar)	Inj. Rate CO_2 (ml/min)	Hydrate formation (hr)
4	3,50	4	70	0,5	3
9	3,50	7	70	0,5	No Hydrate

Electrolytes on the other hand are a known chemical inhibitor and are documented to change the thermodynamic stability of hydrate formation. This is due to the reduction in the chemical potential in the aqueous solution of water when electrolytes are present, thus leading to water being more stable in liquid form rather than as solid hydrate (Husebø et al., 2009). Since electrolytes are not part of the hydrate structure, the presence of electrolytes will lead to a higher concentration of electrolytes in the vacant pore space and consequently leading to a higher initial salt concentration and thus further inhibit hydrate growth. Aqueous solutions containing electrolytes will therefore inhibit hydrate formation by moving the equilibrium line seen in figure 7 further inside the HSZ.

Table 19 and figure 66 below show the effect of changing the electrolyte concentration on hydrate formation. To best compare the effect of salinity on hydrate formation the experiments with the same pressure, temperature and injection rates were compared. These were experiment no. 4, 6 and 8 where the salinities were 3,5, 5,0 and 7,0 wt.% NaCl, respectively. The results from these experiments show that with increasing in electrolyte concentration the hydrate formation time increases, corresponding well with literature (Sloan and Koh, 2008) . The hydrate formation time varies from 3 hours for the lowest salinity (experiment 4) to no hydrate formation for the highest salinity (experiment 8). It can also be seen that when increasing the electrolyte concentration from 3,5 wt.% NaCl (experiment 4) to 5,0 wt.% NaCl (experiment 6), the hydrate formation time increases by 7 hours.

Table 19. Extraction of data from table 11. Experimental summary of CO_2 core experiments with varying salt concentrations.

Exp. no	Salinity (wt.% NaCl)	Temperature (^{o}C)	Pressure (bar)	Inj. Rate CO_2 (ml/min)	Hydrate formation (hr)
5	3,50	4	70	10,0	0,4
4	3,50	4	70	0,5	3
6	5,00	4	70	0,5	10
7	5,00	4	70	5,0	2
8	7,00	4	70	0,5	No hydrate
9	3,50	7	70	0,5	No Hydrate

In the oil industry where CO_2 is being injected into water reservoirs for carbon capture and storage (CCS), the prevention of hydrate formation is crucial to maintain injection rate activity. Since the change in electrolyte concentration is a function of depth and pressure gradients (Pickard, 1975), injecting CO_2 into water reservoirs means injecting into aqueous reservoirs containing different electrolyte concentration. Results show that higher salinity will in lead to prolonged hydrate formation time, corresponding well with literature (Lamorena and Lee, 2008).

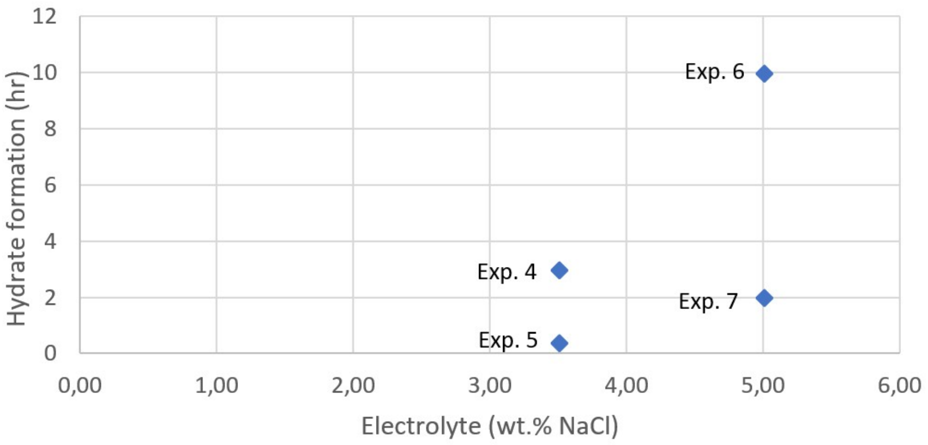

Figure 66. Electrolyte influence on CO_2 hydrate formation time for Bentheimer sandstone core experiments. Figure shows the difference in hydrate formation time for experiment no 4, 5, 6 and 7 at various salt concentrations. The graph shows that the hydrate formation time is quite consistent for 3,5 wt.% NaCl experiments and a larger deviation in formation time can be seen at 5,0 wt.% NaCl. At 7,0 wt.% NaCl there were no successful hydrate formation.

Methanol was used to chemically dissociate the formed hydrate plug in two of the successful hydrate formation experiment. Figure 65 shows experiment 5 with successful dissociation of formed plug by injecting in total 24 ml solution of a 30 wt.% MeOH solution for 2,5 hours. Dissociation of formed plug can be seen when MeOH pressure decreases rapidly at approximately 4,2 hours. Figure also show that when injection of MeOH started there was a rapid increase in the pressure gradient and a slight increase in temperature, verifying the successful hydrate plug formed during CO_2 injection.

Figure 60 shows experiment 4 with successful hydrate formation. Methanol was injected for 1 hour without successful dissociation of formed plug. In total 3,6 ml of a 30 wt.% MeOH solution was injected. The methanol pump was then disconnected, and CO_2 pump connected while temperature was set to 10ºC to thermally dissociate the formed plug. The formed plug dissociated at approx. 5,5 hours with a temperature of 8,3ºC, corresponding with the CO_2 hydrate equilibrium line in figure 7 that shows that at 70 bar the formed CO_2 plug with a 3,5 wt.% NaCl solution is outside the HSZ when the temperature exceeds 8ºC. The formed plug in this experiment would most likely been dissociate by use of methanol if the injection was kept on for a few hours more, such as in experiment 5 where the injection lasted for 2,5 hours with no temperature increase.

4.7.1 Experiments with successful CO_2 hydrate formation

Figure 67 shows the pore volume injected of CO_2 before successful hydrate formation for the four successful hydrate formation experiments. Two of the experiments performed gave successful hydrate formation with 3,5 wt.% NaCl and two with 5,0 wt.% NaCl brine solution, where the blue lines represent experiments with 3,5wt.% NaCl and green lines represent 5,0 wt.% NaCl. The first initial observations from the figure is the difference in pore volume injected between the blue and the green lines, where less PV is injected before pressure buildup for experiments with lower salinity (blue lines). These results correspond well with literature since electrolytes (i.e. NaCl) are documented as good inhibitors for preventing hydrate nucleation.

For both 3,5-and 5,0 wt.% NaCl solution the experiments with the lowest injection rate (0,5 ml CO_2/min) gave CO_2 hydrate formation at a lower pore volume of CO_2 than the higher injection rates. These results show that high injection rate leads to high pore volume of CO_2 injected before hydrate formation.

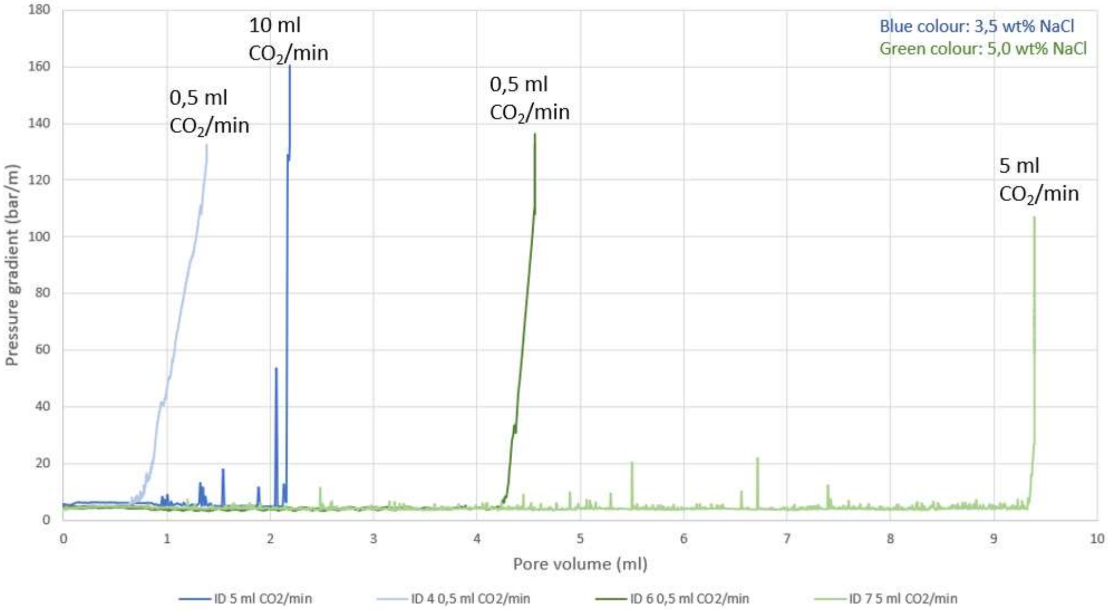

Figure 67. Successful hydrate formation experiment as a function of pressure gradient and pore volume CO_2 injected. Green lines indicated 5,0 wt.% NaCl solution and blue line indicate 3,5 wt.% NaCl solution. Experimental temperature of 4^0C.

Figure 68 on the other hand shows the same experiments as from figure 67 but with time on the x-axis instead of pore volume CO_2 injected. Results from figure 68 display rapid hydrate growth for the experiments with high injection rate (10 ml CO_2/min with 3,5wt.% NaCl and 5 ml CO_2/min with 5,0wt.% NaCl). The driving forces are seen to increase when the injection rate increases. By comparison of the experiments performed with 0,5 ml CO_2/min in figure 68 the increase in the salinity from 3,5-5,0 wt.% NaCl, the hydrate formation time increases from 2,2 to 9,4 hours, illustrating the effect of electrolytes as inhibitor on hydrate growth.

When comparing figure 67 and 68 the highest injection rates for both salinities will lead to the highest pore volume of CO_2 injected in the shortest amount of time. The comparison of experiment number 4 and 5 (blue lines) shows that an increase in injection rate from 0,5 ml CO_2/min to 10 ml CO_2/min will lead to a faster nucleation but not a substantial more amount of CO_2 injected. The 3 hours faster formation time for experiment number 5 than 4 is most likely due to the driving forces increases as injection rate increases in addition to more volume of CO_2 injected. This correlation between driving forces and injection rate can also be shown for the experiments with 5,0 wt.% NaCl solutions, where experiment number 7 with 5 ml CO_2/min gives successful hydrate formation after approximately 2 hours and experiment 6 with 0,5 ml CO_2/min does not form hydrates until 9,4 hours.

The successful CO_2 hydrate formation experiments displayed complete blockage of further injection of CO_2 when hydrates formed. This can be seen in the rapid pressure gradient increase for the experiments with successful hydrate formation in combination with resistivity increase (figure 60, 61, 64 and 65). These results show the possibility of using CO_2 hydrates as a sealing barrier for upwards migration of liquid CO_2 stored in conventional water reservoirs. Furthermore, the solid hydrates formed also display the possibility of storing CO_2 as hydrates for permanent storage in formations within the hydrate stability zone (HSZ).

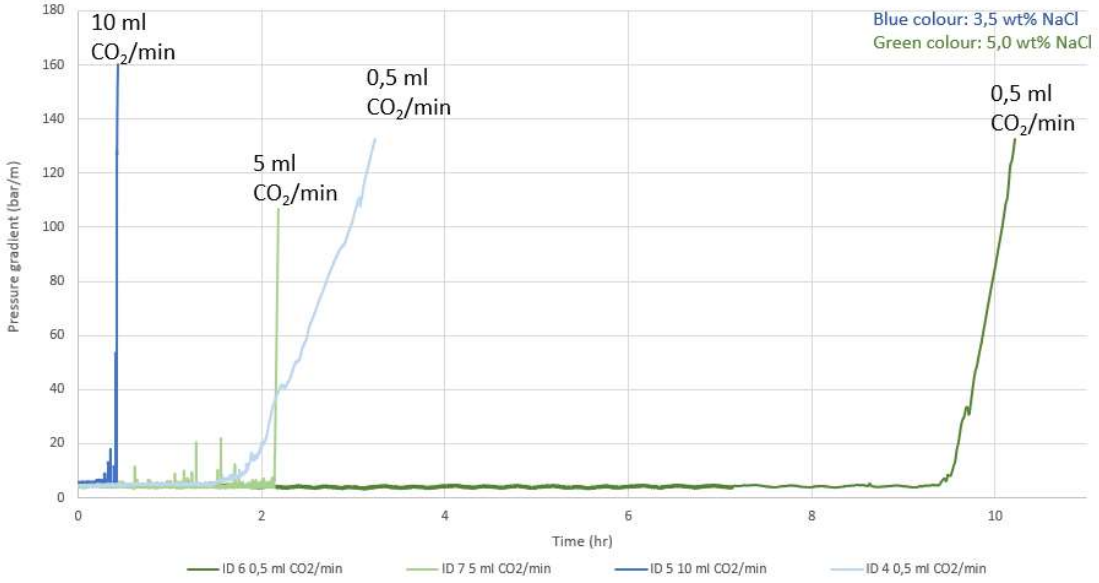

Figure 68. Successful hydrate formation experiment as a function of pressure gradient and time. Green lines indicated 5,0 wt.% NaCl solution and blue line indicate 3,5 wt.% NaCl solution. Experimental temperature of 4ºC.

4.7.2 Experiments without successful CO_2 hydrate formation

Figure 6 shows the pressure-temperature phase diagram for CO_2 hydrate formation at different electrolyte concentrations, where the experimental conditions used for these experiments is indicated by point 1 and 2. Experiment 8 was performed with 7 wt.% NaCl at 4ºC, point 1 in figure 6. The experiment did not form any CO_2 hydrates and according to figure 6 the system is within the hydrate stability zone (left of the grey curve) and should in principle yield hydrate formation. The further the system is inside the HSZ the higher the driving forces and consequently more rapid hydrate formation can occur. If the experiment was left for a longer period of time the CO_2 hydrates could have formed, but due to time constraints the experiment was ended after 27 hours.

Experiment nr 9 was performed at point 2 in figure 6 with 3,5 wt.% NaCl solution at 7ºC and did not form any CO_2 hydrates. From this figure it can be seen that the system is within the HSZ but not as far into the area as to the experiments with successful hydrate formation performed with 3,5 wt.% NaCl at 4ºC, point. 1. This experiment was ended after 27 hours.

The results from the experiment that did not give any hydrate formation can indicate that it is not sufficient to stay within the HSZ to form hydrates, the further the system is inside the HSZ, the larger are the driving forces and the more probable and faster hydrate nucleation can occur. This corresponds well with Equinor's Hydrate management procedure where the operators can operate within the HSZ without forming solid hydrate for a certain period of time (Kinnari et al., 2015). It is therefore also likely that if these experiments were left on for a longer period the CO_2 hydrate formation could have occurred.

5 Conclusions

Final remarks and conclusions based on the three different experimental methods performed in this thesis is presented here. This section is divided into sub-sections based on the different methods, the final section described the implication the results from this thesis has for sequestration of CO_2 into natural reservoirs.

5.1 THF hydrate formation in different chemical environments

Increase in temperature and electrolyte concentration was observed to prolong or even prevent THF hydrate formation, displaying the well documented inhibiting effect of these two parameters. Addition of solid particles to solutions containing THF as hydrate formed showed improved success rate compared to bulk solutions without particles, independent of mole ratio or electrolyte concentrations.

The experiments performed with CN-EC and CN-nonEC presented large variation in hydrate formation, where CN-nonEC yielded hydrates and CN-EC gave no hydrate formation (figure 33), for solutions with 3,5 wt.% NaCl. One suggestion to this deviation is the presence of OH groups for the non-endcapped solid, where the presence of OH group makes the solid surface more water-wet than without these. However, additional experiments are needed for verifications. The wetting properties of the other particles was on average seen to not display a significant and consistent difference to suggest any variation in hydrate formation time caused by the various wetting properties. The addition of solids resulted in significantly lower hydrate formation time compared to bulk solution. Moreover, bulk solution with the ideal hydration number was seen to form more solid hydrates than solution with particles added, suggestion a different growth mechanism with the addition of particles.

Hydrate formation time was also reported to increase with increasing electrolyte concentration, where no hydrates formed for electrolyte concentration of 5,0 wt.% NaCl. Utsira formation water with an electrolyte concentration of 3,2 wt.% NaCl showed consistent high success rate and low hydrate formation time, and no significant change in hydrate formation time was observed with the addition of solid particles. Comparison of NaCl solutions and Utsira formation water reports a greater success rate and lower formation time for Utsira formation water, independent of particles added. These results suggest higher probability of hydrate formation in natural conditions due to naturally occurring substances present.

5.2 MRI technique for investigation of the macroscopic crystal structure of THF hydrate

Magnetic Resonance Imaging (MRI) analysis of THF hydrate structures demonstrates significant difference in macroscopic crystal structure and morphology of ice compared to THF hydrate. The morphology of ice formation was seen to form uniform solid structure whereas the THF hydrate was observed to consist of staggered structures connected to form solid hydrate with liquid phase between the structures.

Addition of Illite and Bentheimer particles resulted in a morphology seen as staggered hydrate with liquid accumulation in the center of the solution, in addition to channels with liquids that upon melting stored more liquid. The morphology of the experiments performed with oil-and water-wet SiO_2 solid particles formed a more uniform hydrate structure, just a limited accumulation of liquids in the center. Only slight accumulation of liquid is seen between the crystals.

The presence of liquid phase between formed hydrate structures for both experiments with particles and in bulks solution could either be liquid phase trapped between formed hydrates leading to excess hydrate former or not enough water to form hydrates. This change in the local liquid composition would then move the system from inside the formation zone to outside. Another option was that the theoretical hydration number of 17 H_2O: 1 THF is based on filling all the available cavities with guest molecules. In real systems, empty cavities will occur, and thus lead to excess of hydrate former after complete hydrate formation.

The use of MRI as an imaging technique has shown to be an excellent tool for investigation of clathrate hydrate macroscopic crystal structures and morphology.

5.3 The CO_2 hydrate formation in Bentheimer cores

Hydrate formation in Bentheimer sandstone core with CO_2 as hydrate former have been successfully performed at 4 and 7ºC with a pore pressure of 70 bar. Temperature-and electrolyte increase was seen to substantially increase the CO_2 hydrate formation time. Increase in electrolyte concentration resulted in prolonging and even prevention of CO_2 hydrate growth, where 3,5 and 5,0 wt.% NaCl solutions resulted in successful hydrate formation and 7,0 wt. % NaCl solution did not form any hydrates. The effect of temperature increase from 4 to 7 ºC was unsuccessful hydrate formation at 7ºC.

Increase in CO_2 injection rate resulted in rapid hydrate growth in addition to higher pore volume of CO_2 injected before hydrate formation compared to experiments performed at lower injection rates. These results suggest that the driving forces increases with the injection rate. Increase in injection rate from

0,5 to 5 ml CO_2/min resulted in a decrease in formation time from 10 to 2 hours. High injection rates should be a preferred option for sequestration of CO_2 into formation, resulting in the highest pore volume injection in the shortest time. Formation of CO_2 hydrates is documented to form solid plugs blocking further injections completely, seen by rapid pressure-and resistivity increase.

5.4 Implication for CO_2 storage in natural reservoirs

Natural occurring substances such as Utsira formation water and Bentheimer sandstone particles were observed to promote hydrate growth. The positive effect of natural occurring substances and particles on hydrate growth display the possibility of permanently storing CO_2 in the formations within the HSZ. The results also show that it is necessary to perform experiment with the actual formation water and cores at the desired area for injection. Increase in electrolyte concentration from 3.5 to 5.0 wt.% NaCl resulted in much longer formation time in addition to larger pore volume injected. These results show that for storage of CO_2 in formations within the HSZ it is beneficial to inject CO_2 where there are high salinities to inhibit hydrate growth to increase the amount of CO_2 injected before formation occurs.

Formation of CO_2 hydrates in Bentheimer sandstone cores were seen to form solid plugs completely blocking further injection. These results show that CO_2 hydrates can work as a sealing barrier for further migration of liquid CO_2 stored in conventional water reservoirs. Above the reservoir where liquid CO_2 is stored, the sealing properties of CO_2 hydrate has the potential to trap escaped CO_2 and prevent leakage. MRI analysis to investigate the spatial distribution of the formed CO_2 plug would provide more detail on the distribution of the formed plug.

The injection rate of CO_2 into the core was with a brine solution of 3.5 wt.% NaCl was seen to have the greatest storage capacity (i.e. pore volume injected) for the experiments with the highest injection rate. However, additional experiments performed by Jarand Gauteplass and Stian Almenningen show that it is difficult to observe any significant difference in pore volume injected and injection rate for the experiment performed with a solution of 3,5wt.% NaCl. A more substantially difference was seen as the salinity increases (Gauteplass et al., 2018). The article further present and conclude that CO_2 hydrate formation leads to robust flow barriers which can work as a sealing barrier for upwards migration of liquid CO_2 stored in conventional water reservoirs.

The results presented in this thesis show that formation of CO_2 hydrates as a sealing barrier for upwards migration of liquid CO_2 stored in conventional reservoirs could work.

6 Recommendation for further work

Additional experiments with CO_2 as hydrates former in Bentheimer sandstone cores should be performed to verify results obtained for this thesis since no replica experiments were performed. In addition, experiments with change in injection rate of CO_2 should also be performed to investigate the effect of injection rate on hydrate formation. Modifying experimental setup to involve temperature logging inside the core would be beneficial for more precise measurements of initial nucleation of hydrate formation. Moreover, performing identical experiments inside an MRI instrument for analysis of the spatial distribution of CO_2 hydrates inside the core would also be beneficial for a broader understanding of formed hydrate plug. Furthermore, experiments with Utsira formation water instead of brine solution should be performed to see if there is a difference in change in the hydrate formation time. Performing identical experiments with THF as hydrate former instead of CO_2 and comparing the formation time should be done to verify if the use of THF as analogue to CO_2 is appropriate.

For the THF experiments performed in different chemical environments the variation in the stirring rate should be performed to see if the hydrate formation time changes. Use of temperature sensors in the samples would provide much more precise formation times than registered in this thesis. The use of the MRI instrument for investigation of the macroscopic crystal structure of formed THF hydrate was very suitable, and additional experiments should be performed for further investigation of the effect of various solid particles on THF hydrate. Moreover, use of NMR spectra for investigation of the liquid phase within the hydrate structure should be performed to identify liquid composition.

Change in the theoretical hydration number for THF should be performed during MRI analysis to investigate if the morphology of the formed hydrate would change compared to the results in this thesis. It is proposed to prepare solutions above and below 17 H_2O: 1 THF in bulk.

Extracting cores and formation water for an area where there is a potential for injecting CO_2, for either blockage for upwards migration of liquid CO_2 or permanent storage, should be performed to investigate the formation of CO_2 hydrates. Performing these experiments in an MRI instrument would bring additional necessary data. Furthermore, use of inhibitors to delay hydrate formation would be beneficial for safe transport of CO_2 into desired location. Performing experiments with inhibitors in sandstone cores should be performed to investigate this effect. Another option is the promotion of CO_2 hydrate growth by addition of the promotors such as sodium dodecyl sulfate (SDS). This could also be of interest to inject CO_2 into formation zones where hydrates not normally form, but the addition of promotors could start the hydrate growth.

Bibliography

ALMENNINGEN, S. 2015. *An Experimental Study of Methane Hydrates in Sandstone Cores.* Master Thesis, Bergen: The University of Bergen.

ANDERSON, R. 2017. *What are Gas Hydrates?* [Online]. Edinburgh: Heriot-Watt University. Available: https://www.egis.hw.ac.uk/hydrate/what-are-gas-hydrates/ [Accessed 15.07 2018].

BAI, D., CHEN, G., ZHANG, X., SUM, A. K., et al. 2015. How Properties of Solid Surfaces Modulate the Nucleation of Gas Hydrate. *Scientific reports,* 5(12747), pp.12747.

BAIRD, C. & CANN, M. C. 2012. *Environmental chemistry.* 5th ed. New York, W.H. Freeman and Co. pp.

BALDWIN, B. A., STEVENS, J., HOWARD, J. J., GRAUE, A., et al. 2009. Using magnetic resonance imaging to monitor CH4 hydrate formation and spontaneous conversion of CH4 hydrate to CO2 hydrate in porous media. *Magnetic Resonance Imaging,* 27(5)**,** Jun, pp.720-726.

BARNES, G. & GENTLE, I. 2005. *Interfacial science : an introduction.* Oxford, Oxford University Press. pp.

BERGE, C. 2017. *An Experimental Study of Foam Flow in Water Saturated Porous Media.* Master Thesis, Bergen: The University of Bergen.

BIROL, F. 2017. *World energy outlook 2017* [Online]. Cairo: SyndiGate Media Inc. Available: https://www.iea.org/weo2017/ [Accessed 12.03 2018].

BLINK, E. J. 2004. *MRI: Physics.* mri-physics.net. pp.

BORGUND, A. E., HOILAND, S., BARTH, T., FOTLAND, P., et al. 2009. Molecular analysis of petroleum derived compounds that adsorb onto gas hydrate surfaces. *Applied Geochemistry,* 24(5)**,** May, pp.777-786.

BOSWELL, R. & COLLETT, T. S. 2011. Current perspectives on gas hydrate resources. *Energy & Environmental Science,* 4(4), pp.1206-1215.

BRAND, U., BLAMEY, N., GARBELLI, C., GRIESSHABER, E., et al. 2016. Methane Hydrate: Killer cause of Earth's greatest mass extinction. *Palaeoworld,* 25(4), pp.496-507.

BROWN, M. A. & SEMELKA, R. C. 2010. *MRI: Basic principles and application.* 4th ed. Hoboken, New Jersey, Wiley-Blackwell. pp.

CHEMISTRY WEB BOOK, N. 2017. *Thermophysical Properties of Fluid systems* [Online]. NIST National Institute of Standards and Technology. Available: https://webbook.nist.gov/chemistry/fluid/ [Accessed 10.07.18].

CHENG, C., ZHAO, J., SONG, Y., ZHU, Z., et al. 2013. In-situ observation for formation and dissociation of carbon dioxide hydrate in porous media by magnetic resonance imaging. *Science China Earth Sciences,* 56(4)**,** Apr, pp.611-617.

CHOPRA, S., WILLOUGHBY, E. C. & RIEDEL, M. 2010. *Geophysical characterization of gas hydrates.* Series no. 14. Tulsa, Okla, Society of Exploration Geophysicists. pp.

CORAK, D., BARTH, T., HØILAND, S., SKODVIN, T., et al. 2011. Effect of subcooling and amount of hydrate former on formation of cyclopentane hydrates in brine. *Desalination,* 278(1)**,** Jan, pp.268-274.

DAVY, H. 1811. On a Combinations of Oxymuriatic Gas and Oxygen Gas. *Philosophical Transactions of the Royal Society of London,* 101, pp.155-162.

DEVARAKONDA, S., GROYSMAN, A. & MYERSON, A. S. 1999. THF–water hydrate crystallization: an experimental investigation. *Journal of Crystal Growth,* 204(4)**,** Aug, pp.525-538.

ENGLEZOS, P., BABU, P., LINGA, P. & KUMAR, R. 2015. A review of the hydrate based gas separation (HBGS) process for carbon dioxide pre-combustion capture. *Energy,* 85(Supplement C), Jun, pp.261-279.

ERIKSEN, C. 2017. *MRI method and development for hydrate studies.* Master Thesis, Bergen: The University of Bergen.

ERSLAND, G., HUSEBO, J., GRAUE, A., BALDWIN, B. A., et al. 2010. Measuring gas hydrate formation and exchange with CO2 in Bentheim sandstone using MRI tomography. *Chemical Engineering Journal,* 158(1), Mar, pp.25-31.

ERSLAND, G., HUSEBØ, J., GRAUE, A. & KVAMME, B. 2009. Transport and storage of CO2 in natural gas hydrate reservoirs. *Energy Procedia,* 1(1), Feb, pp.3477-3484.

ERSTAD, K., HOILAND, S., FOTLAND, P. & BARTH, T. 2009. Influence of Petroleum Acids on Gas Hydrate Wettability. *Energy & Fuels,* 23(3-4), Mar-Apr, pp.2213-2219.

FADNES, F. H. 1996. Natural hydrate inhibiting components in crude oils. *Fluid Phase Equilibria,* 117(1), pp.186-192.

FLEMING, N., RAMSTAD, K., ERIKSEN, S. H., MOLDRHEIM, E., et al. 2007. Development and Implementation of a Scale-Management Strategy for Oseberg Sør. *SPE Production & Operations,* 22(3), Aug, pp.307-317.

GAUTEPLASS, J., ALMENNINGEN, S., ERSLAND, G. & BARTH, T. 2018. Hydrate seal formation during laboratory CO2 injection in a cold aquifer. *Int Journal of Greenhouse Gas Control*, in press.

GRAUE, A., BUANES, T., KUMETSOUA, T., ERSLAND, G., et al. 2007. Storage of CO2 in natural gas hydrate reservoirs and the effect of hydrate as an extra sealing in cold aquifers. *Int. Journal of Greenhouse Gas Control,* 1(2), pp.236-246.

GRAUE, A., KVAMME, B., BALDWIN, B. A., STEVENS, J., et al. 2008. MRI visualization of spontaneous methane production from hydrates in sandstone core plugs when exposed to CO2. *Spe Journal,* 13(2), Jun, pp.146-152.

HESTER, K. C. & BREWER, P. G. 2009. Clathrate Hydrates in Nature. *Annu. Rev. Mar. Sci.,* 1(1), pp.303-327.

HUSEBØ, J., ERSLAND, G., GRAUE, A. & KVAMME, B. 2009. Effects of salinity on hydrate stability and implications for storage of CO2 in natural gas hydrate reservoirs. *Energy Procedia,* 1(1), Feb, pp.3731-3738.

KINNARI, K., HUNDSEID, J., LI, X. & ASKVIK, K. 2015. Hydrate Management in Practice. *J. Chem. Eng. Data,* 60(2), pp.437-446.

KOH, C. A., SUM, A. & SLOAN, E. D. 2010. *Natural Gas Hydrates in Flow Assurance.* Burlington, Elsevier Science. 200 pp.

KOIDE, H., TAKAHASHI, M., TSUKAMOTO, H. & SHINDO, Y. 1995. Self-trapping mechanisms of carbon dioxide in the aquifer disposal. *Energy Conversion and Management,* 36(6), Jun, pp.505-508.

KONTOGEORGIS, G. M. & KIIL, S. 2016. *Introduction to Applied Colloid and Surface Chemistry.* Chicester, John Wiley & amp; Sons, Incorporated. 674 pp.

KVAMME, B., GRAUE, A., BUANES, T., KUMETSOUA, T., et al. 2007. Storage of CO2 in natural gas hydrate reservoirs and the effect of hydrate as an extra sealing in cold aquifers. *Int. Journal of Greenhouse Gas Control,* 1(2), Apr, pp.236-246.

KVENVOLDEN, K. A. 1988. Methane hydrate — A major reservoir of carbon in the shallow geosphere? *Chemical Geology,* 71(1), Dec, pp.41-51.

KVENVOLDEN, K. A. 1993. GAS HYDRATES - GEOLOGICAL PERSPECTIVE AND GLOBAL CHANGE. *Reviews of Geophysics,* 31(2), May, pp.173-187.

KVENVOLDEN, K. A. 1995. A review of the geochemistry of methane in natural gas hydrate. *Organic Geochemistry,* 23(11), Nov, pp.997-1008.

LAL, R. 2008. Carbon sequestration. *Philosophical Transactions of the Royal Society B-Biological Sciences,* 363(1492), Feb, pp.815-830.

LAMORENA, R. B. & LEE, W. 2008. Formation of carbon dioxide hydrate in soil and soil mineral suspensions with electrolytes. *Environmental science & technology,* 42(8), pp.2753.

LARSON, M. A. & GARSIDE, J. 1986. Solute clustering and interfacial tension. *Journal of Crystal Growth,* 76(1), Jul, pp.88-92.

LEE, H., SEO, Y., SEO, Y. T., MOUDRAKOVSKI, I. L., et al. 2003. Recovering methane from solid methane hydrate with carbon dioxide. *Angewandte Chemie-International Edition,* 42(41), pp.5048-5051.

LINGA, P., HO, L. C., BABU, P. & KUMAR, R. 2013. HBGS (hydrate based gas separation) process for carbon dioxide capture employing an unstirred reactor with cyclopentane. *Energy,* 63(Supplement C), Dec, pp.252-259.

LIU, Y., SONG, Y., CHEN, Y., YAO, L., et al. 2010. The detection of tetrahydrofuran hydrate formation and saturation using magnetic resonance imaging technique. *Journal of Natural Gas Chemistry,* 19(3), May, pp.224-228.

MAKOGON, Y. F. 2010. Natural gas hydrates – A promising source of energy. *Journal of Natural Gas Science and Engineering,* 2(1), Apr, pp.49-59.

MAKOGON, Y. F., HOLDITCH, S. A. & MAKOGON, T. Y. 2007. Natural gas-hydrates — A potential energy source for the 21st Century. *Journal of Petroleum Science and Engineering,* 56(1), Mar, pp.14-31.

MASLIN, M., OWEN, M., BETTS, R., DAY, S., et al. 2010. Gas hydrates: past and future geohazard? *Philosophical Transactions of the Royal Society a-Mathematical Physical and Engineering Sciences,* 368(1919), May, pp.2369-2393.

MCCARTNEY, R., MOLDRHEIM, E. & FLEMING, N. 2010. Detection and quantification of Utsira formation water in production wells of the Oseberg Sør field and impact on scale management, Norway, March 15-17, 2010. Geilo: 21st International Oil Field Chemistry Symposium. pp.1-30.

MILKOV, A. V. 2004. Global estimates of hydrate-bound gas in marine sediments: how much is really out there? *Earth-Science Reviews,* 66(3), Aug, pp.183-197.

ORSZULIK, S. T. 2008. *Environmental Technology in the Oil Industry.* Dordrecht, Springer Netherlands. 485 pp.

PANDEY, G., KUMAR, A., VELUSWAMY, H. P., SANGWAI, J., et al. 2017. Morphological Studies of Mixed Methane Tetrahydrofuran Hydrates in Saline Water for Energy Storage Application. *Energy Procedia,* 143, Dec, pp.786-791.

PICKARD, G. L. 1975. *Descriptive physical oceanography : an introduction.* 2nd ed. Oxford, Pergamon Press. 214 pp.

PIÑERO, E., MARQUARDT, M., HENSEN, C., HAECKEL, M., et al. 2013. Estimation of the global inventory of methane hydrates in marine sediments using transfer functions. *Biogeosciences,* 10(2), Feb, pp.959.

RIISØEN, S. 2012. *Effect of Combined Low Salinity and Surfactant Injection on Oil Recovery in Aged Bentheimer Sandstones at Different Temperatures.* Master Thesis, Bergen: The University of Bergen.

ROCHELLE, C. A., CAMPS, A. P., LONG, D., MILODOWSKI, A., et al. 2009. Can CO2 hydrate assist in the underground storage of carbon dioxide? *Geological Society, London, Special Publications,* 319(1), pp.171-183.

RUPPEL, C. D. & KESSLER, J. D. 2017. The interaction of climate change and methane hydrates. *AGU Publications,* 55(1), Mar, pp.126-168.

SLOAN, E. D. 2003. Fundamental principles and applications of natural gas hydrates. *Nature,* 426(6964), pp.353.

SLOAN, E. D. & KOH, C. A. 2008. *Clathrate Hydrates of Natural Gases.* Boca Raton, FL, CRC Press. 721 pp.

TETLIE, E. S. 2017. *Application of MRI in studies of tetrahydrofuran hydrates in quartz sand at atmospheric pressure.* Master Thesis, Bergen: The University of Bergen.

UNITED NATIONS, U. 2015. *The Paris Agreement* [Online]. Paris: United Nations. Available: https://unfccc.int/process-and-meetings/the-paris-agreement/the-paris-agreement [Accessed 01.08 2018].

VELUSWAMY, H. P., KUMAR, A., SEO, Y., LEE, J. D., et al. 2018. A review of solidified natural gas (SNG) technology for gas storage via clathrate hydrates. *Applied Energy,* 216**,** Apr, pp.262-285.

WILSON, P. W., LESTER, D. & HAYMET, A. D. J. 2005. Heterogeneous nucleation of clathrates from supercooled tetrahydrofuran (THF)/water mixtures, and the effect of an added catalyst. *Chemical Engineering Science,* 60(11)**,** Jun, pp.2937-2941.

YANG, M., CHONG, Z. R., ZHENG, J., SONG, Y., et al. 2017. Advances in nuclear magnetic resonance (NMR) techniques for the investigation of clathrate hydrates. *Renewable and Sustainable Energy Reviews,* 74**,** Jul, pp.1346-1360.

ZHAO, J., LV, Q., LI, Y., YANG, M., et al. 2015. In-situ visual observation for the formation and dissociation of methane hydrates in porous media by magnetic resonance imaging. *Magnetic Resonance Imaging,* 33(4)**,** May, pp.485-490.

ZHAO, J., YAO, L., SONG, Y., XUE, K., et al. 2011. In situ observations by magnetic resonance imaging for formation and dissociation of tetrahydrofuran hydrate in porous media. *Magnetic Resonance Imaging,* 29(2)**,** Feb, pp.281-288.

Appendix A- Uncertainty estimations

Uncertainty estimations of carbon dioxide hydrate formation experiments in sandstone core:

Uncertainties in equipment used for the CO_2 hydrate formation experiments are listed in table 20 below.

Table 20. Uncertainty of equipment/instruments used for carbon dioxide hydrate formation in sandstone core experiments

Equipment/instrument	Parameter	Uncertainty
Pressure Transducers (ESI-USB)	Pressure	≤ ± 0,15%
Production cylinder, 50ml	Volume	± 0,5 ml
GF-3000 Digital Balance	Weight	± 0,01 g
ST sigma 1000	Pressure	0,1%
	Flow	0,1%
HH506RA Multilogger thermometer	Temperature	0,1°C
HP Model 4262 A LCR Resistance meter	Resistance	± 0,2-0,3%

Experimental uncertainties:

When weighing the Bentheimer sandstone core after saturation with brine, some of the water imbibed into the core drops onto the weighing scale and the total saturated weight will be slightly overestimated. In addition, some water clings to the surface of the core and hence, will not be part of the total porosity volume. From Stian Almenningnens Master thesis (Almenningen, 2015) the total estimate of these uncertainties were calculated to ± 0.02 (frac.).

Freezing and blocking of the back-pressure regulator (BPR) occurred when carbon dioxide bypassed the regulator. This problem was fixed by putting the BPR on a heating plate.

Uncertainty estimations for the screening process of THF hydrate:

Uncertainty estimations for the equipment used for the THF hydrate formation experiments are shows in table 21 below.

Table 21. Uncertainty estimations of equipment used for the THF screening process experiments.

Equipment/instrument	Parameter	Uncertainty
Thermometer, Digitron	Temperature	± 0,5 ºC
Weighing scale	Weight	± 0,01 g
Fridge compressor	Temperature, air	± 2,0 ºC

Experimental uncertainties:

The refrigerator used for the experiments was equipped with an acrylic glass front with holes making it easy to examine samples without affecting the temperature significantly. One temperature sensor was placed in a water solution next to the experiments to verify desired temperature regularly, mean temperature deviation in the solutions were registered to ± 1,0 ºC. The temperature was regulated by a compressor in the fridge in such a way that when setting the temperature to 2ºC the fridge regulated the air temperature between 0-4ºC. This variation is thought to influence the experiments in addition to an elevated temperature rise in the city from January (maximum temperature 7,9 ºC) when experiments started and until May (maximum temperature 28,2ºC).

The liquid THF solutions used for this thesis was with and without inhibitor (250ppm BHT). To investigate the potential effect of BHT there were identical experiments performed and no effect of solution with or without BHT was observed. BHT is used in THF solutions to prevent explosion hazards.

The experiments performed with 3,5 wt.% NaCl solution formed hydrates in 100% of the cases up until April/May month, where the solutions which normally formed hydrates suddenly did not form hydrates. The surrounding air temperature in the room where the experiments were performed was then investigated to see if this could be the reason for why the solutions did not form hydrates. The temperature in the city had increased from January to May approx. 15-20ºC, and this large temperature change was thought as the most likely reason for why it suddenly became difficult to form hydrates at 2ºC. The temperature for the experiments was then lowered to 0ºC and successful hydrate formation occurs, verifying that the temperature did influence hydrate formation. The conclusion of this work was that a temperature of 2ºC was most likely on the limit of hydrate formation for a THF solution containing 3,5 wt.% NaCl. The remaining experiment were performed at 0ºC.

The air compressor that regulated the temperature in the refrigerator turned off and on depending on the temperature, this on and off on the compressor had subsequent vibrations associated. These vibrations could possibly affect the hydrate formation if the sample was on the verge of hydrate formation and an additional vibration of the sample could lead to successful hydrate formation. It was seen several times that when the sample was within the hydrate stability zone and agitation was induced by either shaking the sample or tipping it upside down the sample spontaneous crystallized. These vibrations from the refrigerator could possibly affect hydrate formation.

The initial experiments did not have any video camera to record the exact time for THF to nucleate and thus leading to unprecise hydrate formation times. The author only monitored the experiments within normal working hours. A web camera was purchased and set up to register a more precise formation time. Several of the experiments performed for the initial experiments with unprecise formation time were verified by additional experiments to verify the hydrate formation time by use of the web camera.

Appendix B- Calculations

This section contains explanation of how different calculations were conducted for all experiments in this thesis.

Calculations for the CO_2 experiments in the Bentheimer sandstone core:

Porosity calculations:

Calculation of porosity was done by using the following expression:

$$\phi = \frac{V_b}{V_t} * 100\% \qquad \text{Equation 1}$$

, where:

ϕ: porosity,

Vb: bulk volume

Vt: total volume of core (V= Area x Length = πr^2x L)

Permeability calculations:

Darcy's equation for a single fluid in a porous media (Equation 2) was used to calculate the absolute permeability by rearranging the equation:

$$q = k * \frac{\Delta P * A}{\mu * L} \qquad \text{Equation 2}$$

$$k = \frac{q}{A} * \frac{L * \mu}{\Delta P}$$

, where:

q: flow rate through the porous media (cm^3/s),

k: absolute permeability (D),

A: cross section of core (cm^2),

L: length of core (cm),

ΔP: differential pressure across the core (atm)

μ: Viscosity of solution (cP= 1 kg/ms)

Darcy equation (Equation 2) is applicable for systems where the core is in a horizontal position, incompressible fluid, core 100% saturated with desired solution, stationary flow, laminar fluid flow and no chemical reactions. Each of these criteria were met for the experiments performed.

Calculation of absolute permeability involved flooding the saturated core with brine solution at different injection rates (10, 20, 40 and 50 ml/min) and then calculating the average differential pressure for each injection rate and then the mean permeability for the core could be found.

Calculation of irreducible water saturation, S_{iw}:

Calculation of irreducible water saturation for each core was performed by subtracting the produced liquid with the imbibed water originally in the core, and then using the following expression:

$$S_{iw} = \frac{\frac{S_w}{\rho_{brine}}}{V_p} \qquad \text{Equation 3}$$

, where S_w: imbibed water, ρ_{brine}: density brine solution and V_p: pore volume

Appendix C- Additional data for the THF experiments

The desired mole ratio and electrolyte concentration were pre-prepared in batch solutions of 0,5 L or 1,0 L before adding the solution into different vials with or without addition of solids. Approximately 40 g of liquid solution was used and 0,5 or 1g of solid. The total weights for the liquid solutions and solids added for each sample is listed in table 1 below. The samples were prepared at room temperature (22ºC) before placing them into the pre-cooled refrigerator at desired temperature.

Tabell 1. Weight of liquid solution and added solids of the THF screening process experiments. The table list the different mole ratio used, electrolyte and solids added for each experiment.

Sample ID	Composition liquid	Electrolyte (wt.% NaCl)	Solid surface	Weigh solid (g) ± 0,001 g	Weight liquid (g) ± 0,001 g
1	17 H_2O: 1 THF	0	-	-	40,017
2	17 H_2O: 1 THF	3,5	-	-	40,097
3	17 H_2O: 1 THF	0	SiO_2	0,503	40,01
4	17 H_2O: 1 THF	0	SiO_2	1,005	40,029
5	17 H_2O: 1 THF	3,5	SiO_2	0,509	40,046
6	17 H_2O: 1 THF	3,5	SiO_2	0,999	39,999
7	17 H_2O: 1 THF	0	-	-	39,989
8	17 H_2O: 1 THF	0	-	-	40,023
9	17 H_2O: 1 THF	0	SiO_2	0,5	39,987
10	17 H_2O: 1 THF	0	SiO_2	0,503	40,023
11	17 H_2O: 0,33 THF	0	-	-	40,081
12	17 H_2O: 0,33 THF	0	-	-	39,999
13	17 H_2O: 0,33 THF	0	SiO_2	0,501	40,123
14	17 H_2O: 0,33 THF	0	SiO_2	0,503	39,967
15	17 H_2O: 0,66 THF	0	-	-	40,049
16	17 H_2O: 0,66 THF	0	-	-	40,003
17	17 H_2O: 0,66 THF	0	SiO_2	0,5	40,13
18	17 H_2O: 0,66 THF	0	SiO_2	0,5	40,009
19	17 H_2O: 1 THF	0	CN-nonEC	0,455	40,069
20	17 H_2O: 1 THF	0	C18	0,526	40,004
21	17 H_2O: 0,66 THF	0	CN-nonEC	0,476	40,008
22	17 H_2O: 0,66 THF	0	C18	0,49	40,074
23	17 H_2O: 1 THF	5	-	-	40,05
24	17 H_2O: 1 THF	5	-	-	40,048
25	17 H_2O: 1 THF	5	SiO_2	0,506	40,017

26	17 H_2O: 1 THF	5	SiO_2	0,517	40,026
27	17 H_2O: 1 THF	5	SiO_2	1,001	40,02
28	17 H_2O: 1 THF	3,5	-	-	40,024
29	17 H_2O: 1 THF	3,5	CN-nonEC	0,436	40,03
30	17 H_2O: 1 THF	3,5	C18	0,509	40,034
31	17 H_2O: 1 THF	3,5	-	-	40,078
32	17 H_2O: 1 THF	3,5	CN-nonEC	0,458	40,011
33	17 H_2O: 1 THF	3,5	CN-nonEC	0,442	39,998
34	17 H_2O: 1 THF	3,5	SiO_2	0,511	40,036
35	17 H_2O: 1 THF	3,5	SiO_2	0,515	40,085
36	17 H_2O: 1 THF	0	CN-EC	0,412	40,024
37	17 H_2O: 1 THF	0	CN-EC	0,466	390999
38	17 H_2O: 1 THF	0	CN-EC	0,528	40,007
40	17 H_2O: 1 THF	0	CN-EC	0,484	40,028
41	17 H_2O: 1 THF	0	CN-EC	0,48	40,081
43	17 H_2O: 1 THF	3,5	CN-EC	0,441	40,108
44	17 H_2O: 1 THF	3,5	CN-EC	0,497	40
45	17 H_2O: 1 THF	3,5	CN-EC	0,504	40,003
46	17 H_2O: 1 THF	3,5	CN-EC	0,533	40,009
47	17 H_2O: 1 THF	3,5	CN-EC	0,487	40,065
48	17 H_2O: 1 THF	3,5	CN-EC	0,497	40,053
49	17 H_2O: 1 THF	3,5	CN-EC	0,481	40,014
50	17 H_2O: 1 THF	3,5	-	-	40,087
51	17 H_2O: 1 THF	3,5	-	-	40,09
52	17 H_2O: 1 THF	3,5	-	-	40,017
53	17 H_2O: 1 THF	3,5	-	-	40,334
55	17 H_2O: 1 THF	3,5	-	-	40,017
60	17 H_2O: 1 THF	3,5	-	-	40,048
61	17 H_2O: 1 THF	3,5	-	-	39,993
62	17 H_2O: 1 THF	3,5	-	-	39,966
70	17 H_2O: 1 THF	3,5	Si60	0,409	41,26
71	17 H_2O: 1 THF	3,5	Si60	0,429	40,035
72	17 H_2O: 1 THF	3,5	Si60	0,49	40,208
73	17 H_2O: 1 THF	3,5	Si60	0,694	40,335
74	17 H_2O: 1 THF	0	CN-EC	0,409	39,984
75	17 H_2O: 1 THF	0	CN-EC	0,45	40,112
76	17 H_2O: 1 THF	0	CN-EC	0,458	39,945
77	17 H_2O: 1 THF	0	CN-EC	0,468	39,956
78	17 H_2O: 1 THF	0	-	-	40,085
79	17 H_2O: 1 THF	0	-	-	39,945

80	17 H_2O: 1 THF	0	-	-	40,053
81	17 H_2O: 1 THF	0	Bentheimer	0,505	40,142
82	17 H_2O: 1 THF	0	Bentheimer	0,52	40,273
83	17 H_2O: 1 THF	3,5	Bentheimer	0,524	39,969
84	17 H_2O: 1 THF	3,5	Bentheimer	0,543	40,017
85	17 H_2O: 1 THF	3,5	Bentheimer	0,504	40,031
86	17 H_2O: 1 THF	3,5	Bentheimer	0,543	40,206
87	17 Utsira: 1 THF	3,2	-	-	40,09
88	17 Utsira: 1 THF	3,2	-	-	39,992
89	17 Utsira: 1 THF	3,2	-	-	39,91
90	17 Utsira: 1 THF	3,2	-	-	40,05
91	17 Utsira: 1 THF	3,2	Bentheimer	0,514	39,936
92	17 Utsira: 1 THF	3,2	Bentheimer	0,523	39,938
93	17 Utsira: 1 THF	3,2	Bentheimer	0,535	39,068
94	17 Utsira: 1 THF	3,2	Bentheimer	0,52	39,996
95	17 Utsira: 1 THF	3,2	Bentheimer	0,542	40,007
96	17 Utsira: 1 THF	3,2	Bentheimer	0,522	40,067
97	17 Utsira: 1 THF	3,2	Bentheimer	0,512	40,033
98	17 Utsira: 1 THF	3,2	Bentheimer	0,511	40,183
99	17 Utsira: 1 THF	3,2	-	-	39,985
100	17 Utsira: 1 THF	3,2	-	-	40,018
101	17 Utsira: 1 THF	3,2	-	-	39,992
102	17 Utsira: 1 THF	3,2	-	-	39,98
103	17 Utsira: 1 THF	3,2	Bentheimer	0,523	40,024
104	17 Utsira: 1 THF	3,2	Bentheimer	0,516	40,006
105	17 Utsira: 1 THF	3,2	Bentheimer	0,457	40,022
106	17 Utsira: 1 THF	3,2	-	-	39,924
107	17 Utsira: 1 THF	3,2	-	-	40,008
108	17 Utsira: 1 THF	3,2	-	-	40,046
109	17 Utsira: 1 THF	3,2	-	-	40,045
110	17 Utsira: 1 THF	3,2	-	-	40,052
111	17 Utsira: 1 THF	3,2	-	-	39,985
112	17 H_2O: 1 THF	3,5	-	-	39,957
113	17 H_2O: 1 THF	3,5	-	-	40,025
114	17 H_2O: 1 THF	3,5	-	-	40,023
115	17 H_2O: 1 THF	3,5	-	-	40,058
116	17 H_2O: 1 THF	0	-	-	40,009
117	17 H_2O: 1 THF	0	-	-	40,013
118	17 H_2O: 1 THF	0	-	-	40,007
119	17 H_2O: 1 THF	0	-	-	39,998
120	17 H_2O: 1 THF	0	-	-	40,029
121	17 H_2O: 1 THF	3,2	-	-	39,977
122	17 H_2O: 1 THF	3,2	-	-	40,019

123	17 H_2O: 1 THF	3,2	-	-	40,005
124	17 H_2O: 1 THF	3,2	-	-	39,95
125	17 H_2O: 1 THF	3,2	-	-	40,066
126	17 Utsira: 1 THF	3,2	-	-	40,041
127	17 Utsira: 1 THF	3,2	-	-	39,957
128	17 Utsira: 1 THF	3,2	-	-	40,026

Appendix D- Additional data for the baseline experiments

Each of the different baseline experiments performed at the three different injection rates (0,5, 5 and 10 ml CO_2/min) were cooled down to the hydrate formation conditions for CO_2 and all had successful hydrate formation, confirmed by resistivity measurements. The resistivity reached a maximum of 92 Ωm for experiment 1_a with a total volume of 230 ml CO_2 injected. Experiment 3_c reached a maximum of 76 with a total volume of 81 ml CO_2 injected. Experiment 2_b reached a maximum of 52 with a total volume of 90 ml CO_2 injected, data shows in table 22 below.

Table 22. Summary of experimental data obtained from the Baseline experiments during CO_2 hydrate formation.

ID	CO_2 injectivity rate (ml/min)	Successful hydrate formation (Yes/No)	Volume CO_2 injected total (ml)	Time until significant resistivity increase (hr)	Maximum resistivity (Ωm)
1_a	5	Yes	230	12	92
2_b	0,5	Yes	90	14	52
3_c	10	Yes	81	2,8	76